

**WWU**  
MÜNSTER



institut für  
theoretische physik

# THEORETICAL ASPECTS OF JET QUENCHING IN HEAVY-ION COLLISIONS

MASTER THESIS

Jan Honermann

Westfälische Wilhelms-Universität Münster

Institut für Theoretische Physik

AG Klasen

Supervisor & first examiner: Prof Dr. Michael Klasen

Second examiner: PD. Dr. Karol Kovarik

Münster, 09.05.2019

# Plagiarism declaration

I hereby declare that this M.Sc. thesis about theoretical aspects of jet quenching in heavy-ion collisions is my own work, that I have not used any sources or aids other than the ones listed, and that those parts of the thesis which are based on other works – including electronic media – in wording or content have definitely been marked as such and are accompanied by a bibliographical reference to the source.

I agree to a comparison of the work with other texts in order to find similarities and to the storage of the work in a database for this purpose.

Münster, 09.05.2019

---

Signature

# Contents

<b>1</b>	<b>Introduction</b>	<b>1</b>
<b>2</b>	<b>Quantum chromodynamics</b>	<b>3</b>
2.1	A very brief look at the development from QED to QCD . . . . .	3
2.2	QCD Lagrangian . . . . .	5
2.3	Group theory . . . . .	6
2.4	Perturbative quantum chromodynamics . . . . .	9
2.5	Running coupling . . . . .	11
<b>3</b>	<b>Deep inelastic scattering</b>	<b>15</b>
3.1	Parton model . . . . .	16
3.2	Parton distribution functions . . . . .	19
3.3	DGLAP equations . . . . .	22
3.4	Factorisation . . . . .	25
3.5	Parton shower . . . . .	26
3.6	Hadronisation/Fragmentation . . . . .	28
3.7	Glauber model . . . . .	31
<b>4</b>	<b>Jets</b>	<b>36</b>
<b>5</b>	<b>Quark-gluon plasma</b>	<b>40</b>
5.1	Bjorken Model . . . . .	42
5.2	Probing the QGP . . . . .	44
<b>6</b>	<b>JEWEL</b>	<b>48</b>
6.1	Process Generation . . . . .	48
6.2	Medium Modifications . . . . .	49
6.3	Background subtraction . . . . .	52

---

<b>7</b>	<b>Experimental data of jet production in lead-lead collisions from the LHC</b>	<b>55</b>
<b>8</b>	<b>Results</b>	<b>59</b>
8.1	ALICE . . . . .	63
8.2	CMS . . . . .	68
8.3	ATLAS . . . . .	73
<b>9</b>	<b>Conclusion</b>	<b>77</b>
<b>A</b>	<b>Calculation of invariant matrix elements in pQCD at tree level</b>	<b>80</b>
A.1	Quark, antiquark $\rightarrow$ quark, antiquark . . . . .	80
A.2	Quark, gluon $\rightarrow$ quark, photon . . . . .	82
A.3	Quark, antiquark $\rightarrow$ gluon, photon . . . . .	86
A.4	gluon, gluon $\rightarrow$ gluon, gluon . . . . .	87
A.4.1	Spinor-Helicity Formalism . . . . .	87
A.4.2	Diagrams . . . . .	90
	<b>List of Figures</b>	<b>96</b>
	<b>Bibliography</b>	<b>97</b>

# 1 Introduction

Conditions of the early universe can, albeit for fractions of a second, be produced in experiments. As it turns out, simply colliding protons at ever higher energies does not produce a detectable medium, but collisions of heavy nuclei, lead in the case of the LHC, at ultra-relativistic velocities do. Without a medium, high-energy jets consisting of quarks and gluons, the subatomic constituents of protons and neutrons, form after the collision and later hadronise into detectable particles. The unobservability of quarks and gluons is a property of the strong interaction, coined confinement. The short-lived state of free quarks and gluons in the collision is called the quark-gluon plasma. Jet quenching is referring to the loss of energy a jet suffers while passing through a dense and hot medium, namely the quark-gluon plasma, after heavy nucleus collisions, due to strong interactions with constituents of the medium. Properties of the medium can then be deduced by comparing the result of measurements with the expected values in the vacuum case, where no medium is present. A chief observable for this, and the main focus of this thesis, is the nuclear modification factor, defined as

$$R_{AA} = \frac{\frac{1}{N_{\text{Evt}}} \left. \frac{d^2 N_{\text{jets}}^{AA}}{dp_T d\eta} \right|_{\text{cent}}}{\langle T_{AA} \rangle \left. \frac{d^2 \sigma_{\text{jets}}}{dp_T d\eta} \right|_{\text{pp}}}, \quad (1.1)$$

where  $N_{\text{jets}}^{AA}$  is the jet yield, the number of jets, in heavy nucleus collisions divided by the differential cross section of jet production in pp-collisions. To account for the increased size and number of constituents of a lead nucleus as compared to a single proton,  $\langle T_{AA} \rangle$  is introduced. This quantity is obtained in the framework of the Glauber model, to be discussed in more detail later, and should normalise the ratio to 1, if nothing else happens. In experiments a value significantly below 1 is reported, hinting at the presence of a medium. In this thesis the nuclear modification factor will be calculated with JEWEL, a leading-order Monte Carlo event generator that includes

medium effects, and compared to experimental data. In order to run JEWEL with newer PDF sets like nCTEQ15 and give estimates about scale uncertainties some slight modifications will be made to JEWEL, to be discussed in more detail later.

The thesis is structured as follows: the basics of quantum chromodynamics will be discussed first in chapter 2. The Feynman rules will be given and the chapter ends with a brief discussion of the running strong coupling. A discussion of deep inelastic scattering follows in chapter 3, referring to scatterings where the beam particles are completely unravelled. After the parton model, which was used as a model for proton-proton collisions before the advent of QCD, the basic notion of PDF's will be introduced, accounting for the substructure of composite objects like protons, Together with the DGLAP equations and factorisation. Afterwards, the parton shower, an essential ingredient of simulations concerning particle collisions, is reviewed. The chapter closes with a discussion of the Glauber model, which nowadays is mostly used to give geometric corrections for the comparison of proton-proton (pp) collisions with lead-lead (Pb+Pb) collisions. Chapter 4 will expand the notion of jets, as a proxy for initial outgoing products of the hard scattering, which can be measured in experiments. An intuitive view of the formation of a quark-gluon plasma (QGP) is given in chapter 5. The Bjorken model is introduced, which gives a one-dimensional expansion of the QGP. Also basic mechanisms of interactions in the medium are reviewed, together with possible probes. Next, chapter 6, discusses some details of JEWEL. Results obtained by JEWEL are compared to three experimental analyses in chapter 8. Chapter 7 gives a list of available experimental analyses, which could be used for future works. In Appendix A the calculation of QCD matrix elements at leading order is exemplified.

## 2 Quantum chromodynamics

A natural starting point for the investigation of jet quenching phenomena in heavy-ion collisions is the theory of strong interactions, quantum chromodynamics (QCD). A brief overview of the main aspects of QCD and group theory will be given in this chapter. In the last part, the strong coupling constant  $\alpha_s$  will be discussed. For more detailed derivations and explanations one can look at textbooks by e.g. Schwartz [40] or Peskin and Schröder<sup>1</sup> [37].

### 2.1 A very brief look at the development from QED to QCD

The success of quantum electrodynamics (QED) - which governs the behaviour of charged particles, photons and interactions between those two based upon the Abelian local gauge group  $U(1)$  - in calculating e.g. the anomalous magnetic moment of the electron and cross sections showed that quantum field theories (QFTs) are a worthwhile subject of investigation. For this people had to learn how occurring divergent expressions at intermediate steps in calculations could be handled to yield finite results. From QED people also gained a very important insight: the coupling constant of the electromagnetic force  $\alpha_{el}$  is not a constant, but it possesses a scale dependence: The coupling constant gets smaller with increasing energy. This running coupling constant offered a possible solution to a puzzling problem people were facing back then. With the advent of particle accelerators and scattering experiments and the increase of collision energy in ever larger and sophisticated machines, it soon became apparent that the proton is not a fundamental particle, but composed of what would later

---

<sup>1</sup>Upon which this chapter is mainly based.

be identified as quarks and gluons. These particles themselves have never been observed outside of a proton. This fact, together with additional insights from collider experiments about the substructure of protons, lead to the formulation of two defining properties for the force of strong interactions, which governs the behaviour of quarks and gluons: confinement and asymptotic freedom. Confinement states that quarks and gluons have to be bound inside of particles in nature and cannot be observed in e.g. a detector<sup>2</sup>, while asymptotic freedom states that quarks and gluons can be considered as free particles at very small distances, for example inside of a proton. The coupling of a theory of strong interactions thus needs to be small at large energy scales and big at small scales, the opposite behaviour of  $\alpha_{\text{el.}}$ . As it turns out, it is possible to construct such a theory. These theories are generalisations of QED, using a non-Abelian group as gauge group and are therefore known as non-Abelian gauge theories or otherwise Yang-Mills theories. QCD is based upon the special unitary group  $SU(3)_c$  and it will be shown later that the coupling of QCD gets weaker with increasing energy.  $SU(3)_c$  stands for  $SU(3)$  colour, with the colour charges of QCD green, blue and red. The QCD Lagrangian possesses other symmetries besides the colour symmetry, but these will be explicitly marked when talked about, so that mentions of the  $SU(3)$  symmetry of QCD refers to the colour part. Though  $SU(3)$  is established as gauge group for QCD to describe measurements, one can give many relations and formulas for a general  $SU(N)$  gauge group, which will be done in the next sections, while continuing to talk about e.g. gluons as the gauge bosons. One can simply put in a 3 for every N that turns up and will obtain the result for QCD. As a last closing remark: natural units are used in all following chapters, which means that  $c = \hbar = 1$ . In natural units it follows that  $E = p = \frac{1}{l}$  with the energy  $E$ , the momentum  $p$  and a length  $l$ , while also making occurring formulas nicer to write down. Results obtained in natural units can afterwards be multiplied by appropriate powers of  $c$  and  $\hbar$  to obtain the right dimensions of units.

---

<sup>2</sup>Or only colour-neutral objects can exist in nature.



## 2.2 QCD Lagrangian

The Lagrangian of QCD, after quantisation, is given by:

$$\begin{aligned} \mathcal{L} = & \bar{\psi}_i (\delta_{ij} i \not{\partial} + g A^a T_{ij}^a - m \delta_{ij}) \psi_j - \frac{1}{4} (F_{\mu\nu}^a)^2 \\ & + (\partial_\mu \bar{c}^a) (\delta^{ac} \partial_\mu + g f^{abc} A_\mu^b) c^c - \frac{1}{2\xi} (\partial_\mu A_\mu^a)^2 . \end{aligned} \quad (2.1)$$

The quark fields  $\psi_i$  with their mass  $m$  are described by spin-1/2 spinors, the mid-alphabet Latin letters are used to signify colour indices. Sum convention is implied: a sum is running over every index that appears twice. There are 6 different known quarks<sup>3</sup>, each with its own anti-particle, grouped in three generations. Since they can not be measured as free particles, there are some subtleties involved in giving a mass to a quark. Their mass can only be given in a specific renormalization scheme, see table 2.1 for the masses in the most widely used scheme. Feynman slash notation  $\not{\partial} = \gamma_\mu \partial^\mu$  is used, with the gamma matrices  $\gamma_\mu$ . The  $g$  is the strong coupling constant and  $A_\mu^a$  are the gluon fields, massless spin-1 fields. Gluons carry a colour charge, as opposed to the uncharged photons in QED. This charged mediator of the strong force leads to a vastly different phenomenology for QCD, but it also means that calculations become more complicated. The early-alphabet Latin letters index the different generators  $T^a$  of  $SU(N)$ ; there is one gluon field for each generator. The next section will be a brief discussion of group theory, where more details are given. The field strength tensor is defined as

$$F_{\mu\nu}^a = \partial_\mu A_\nu^a - \partial_\nu A_\mu^a + g f^{abc} A_\mu^b A_\nu^c \quad (2.2)$$

with the structure constants  $f^{abc}$ .

$c^a$  and  $\bar{c}^a$  are the Faddeev-Popov ghosts, spin-0 particles with fermionic statistics. Since they violate the spin-statistics theorem, they cannot appear as physical fields, but they can appear in the path integral formulation. When expanding the path integral in perturbation theory, ghost appear in internal lines of Feynman diagrams. They suppress unphysical degrees of freedom of gluons in calculations. There is one ghost pair for every gluon, but it is not required from the derivation that ghost and anti-ghosts are related. The last term written down is the so-called gauge-fixing term.

The QCD Lagrangian possesses some accidental symmetries. There is a global  $U(1)$  symmetry, which constitutes the conservation of the baryon number. For the first

---

<sup>3</sup>Also called flavours.

Quark	down	up	strange	charm	bottom	top
mass (MeV)	4.7	2.15	93.5	1270	4180	163000
Charge	-1/3	+2/3	-1/3	+2/3	-1/3	+2/3

Table 2.1: Quark masses in the  $\overline{\text{MS}}$  scheme and their charges.

three quark flavours there exists an additional  $\text{SU}(3)_F$  symmetry, the flavour symmetry. Neglecting the masses, this is an exact symmetry; with the different quark masses included, it still represents an approximative symmetry, meaning that results calculated by assuming an exact symmetry still give mostly correct results. Another global symmetry of the Lagrangian is the BRST (Becchi, Rouet, Stara and Tyutin) invariance, which is important for the renormalisability of non-Abelian gauge theories. With the help of BRST invariance, one can show that only a finite amount of counterterms are necessary to cancel all infinities of the theory.

## 2.3 Group theory

This section is a short summary of basic aspects of group theory. In mathematics, a group is an algebraic structure  $(\mathbf{G}, \circ)$  which connects a set of elements via the operation  $\circ$ . A group needs to fulfil four axioms, also called the group axioms:

$$\begin{aligned}
 (\mathbf{G0}) : \text{Closure} & \quad \forall \mathbf{a}, \mathbf{b} \in \mathbf{G} : \mathbf{a} \circ \mathbf{b} \in \mathbf{G} \\
 (\mathbf{G1}) : \text{Associativity} & \quad \forall \mathbf{a}, \mathbf{b}, \mathbf{c} \in \mathbf{G} : (\mathbf{a} \circ \mathbf{b}) \circ \mathbf{c} = \mathbf{a} \circ (\mathbf{b} \circ \mathbf{c}) \\
 (\mathbf{G2}) : \text{Identity} & \quad \exists \mathbf{e} \in \mathbf{G} : \forall \mathbf{a} \in \mathbf{G} : \mathbf{e} \circ \mathbf{a} = \mathbf{a} = \mathbf{a} \circ \mathbf{e} \\
 (\mathbf{G3}) : \text{Inverse} & \quad \forall \mathbf{a} \in \mathbf{G} : \exists \mathbf{b} \in \mathbf{G} : \mathbf{a} \circ \mathbf{b} = \mathbf{e} = \mathbf{b} \circ \mathbf{a}.
 \end{aligned} \tag{2.3}$$

Groups can be very abstract constructs, but there are also quite simple and intuitive examples for groups. Integers  $\mathbb{Z}$  with addition form a group  $(\mathbb{Z}, +)$ . An important class of groups for physics are the so-called Lie groups. These are groups with an infinite number of elements but only a finite number of generators. Any group element connected to the identity can be written as

$$U = \exp(i\theta^a T^a) \cdot \mathbf{1}, \tag{2.4}$$

where  $T^a$  are the group generators and  $\theta^a$  are numbers. The generators of a Lie group form a Lie algebra which is defined as the Lie bracket:

$$[T^a, T^b] = if^{abc}T^c, \quad (2.5)$$

with the structure constants  $f^{abc}$ , corresponding to a mapping  $\mathcal{G} \times \mathcal{G} \rightarrow \mathcal{G}$ . The structure constants fulfil the Jacobi identity:

$$f^{abd}f^{dce} + f^{bcd}f^{dae} + f^{cad}f^{dbe} = 0. \quad (2.6)$$

The group elements can be placed in operators that act on a vector space; a particular embedding is called a representation. For finite-dimensional representations they will be embedded in matrices. Given a representation, the Lie bracket from equation (2.5) can be defined as a commutator:

$$[A, B] = AB - BA. \quad (2.7)$$

With this, the Jacobi identity (2.6) can also be formulated in terms of commutators:

$$[A, [B, C]] + [B, [C, A]] + [C, [A, B]] = 0. \quad (2.8)$$

For every application in physics, the group elements can be embedded into matrices; the more abstract definition (2.5) is included for completeness' sake.

Furthermore, for physical applications there is a very important kind of Lie algebras like  $\mathfrak{su}(N)$  or  $\mathfrak{so}(N)$ , the simple Lie algebras. They are defined as having no non-trivial ideals. Ideals are subalgebras defined by:

$$\exists \mathbf{I} \subset \mathbf{G} : \forall \mathbf{g} \in \mathbf{G} : \forall \mathbf{i} \in \mathbf{I} : [\mathbf{g}, \mathbf{i}] \in \mathbf{I}. \quad (2.9)$$

A semisimple Lie algebra is an algebra that is made out of the direct sum of simple Lie algebras, like the Lie algebra of the Standard Model  $\mathfrak{su}(3) \oplus \mathfrak{su}(2) \oplus \mathfrak{u}(1)$ . The important part now is the existence of a theorem that states that all finite-dimensional representations of semisimple algebras are Hermitian.

For the last part we focus on the group  $SU(N)$ , the special unitary group. It preserves a complex inner product, so  $U^\dagger U = \mathbf{1}$ . Also  $\det(U) = 1$  is required. The group acts on

an  $N$ -dimensional vector space and elements can be written as (2.4). The generators are Hermitian and can be found by expanding this expression around  $\mathbb{1}$ . In total there are  $N^2 - 1$  generators, so the dimension of the group is  $d(\text{SU}(N)) = N^2 - 1$ . Commonly used representations in physics are the (anti-) fundamental or defining and the adjoint representation, with the fundamental representation being the smallest non-trivial representation of the algebra. By default the generators  $T^a$  will be in the fundamental representation; other representations are denoted by a subscript. For the fundamental one, the generators are  $N \times N$ -dimensional Hermitian matrices with trace 0. Under infinitesimal group transformations, a set of  $N$  fields, in our case the quark fields  $\phi_i$ , transforms as

$$\phi_i \rightarrow \phi_i + i\alpha^a (T^a)_{ij} \phi_j \quad (2.10)$$

with  $\alpha^a$  being real numbers. The antiquarks are described by complex conjugated fields, which transform in the anti-fundamental representation, defined as  $T_{\text{anti-fund}}^a = -(T^a)^*$ . Now one can work out the generators in the fundamental representation. In the case of the  $\text{SU}(3)$  for QCD these are in most cases given as  $T^a = \frac{1}{2}\lambda^a$ , with the Gell-Mann matrices  $\lambda$ :

$$\begin{aligned} \lambda^1 &= \begin{pmatrix} 0 & 1 & 0 \\ 1 & 0 & 0 \\ 0 & 0 & 0 \end{pmatrix}, & \lambda^2 &= \begin{pmatrix} 0 & -i & 0 \\ i & 0 & 0 \\ 0 & 0 & 0 \end{pmatrix}, & \lambda^3 &= \begin{pmatrix} 1 & 0 & 0 \\ 0 & -1 & 0 \\ 0 & 0 & 0 \end{pmatrix}, \\ \lambda^4 &= \begin{pmatrix} 0 & 0 & 1 \\ 0 & 0 & 0 \\ 1 & 0 & 0 \end{pmatrix}, & \lambda^5 &= \begin{pmatrix} 0 & 0 & -i \\ 0 & 0 & 0 \\ i & 0 & 0 \end{pmatrix}, & \lambda^6 &= \begin{pmatrix} 0 & 0 & 0 \\ 0 & 0 & 1 \\ 0 & 1 & 0 \end{pmatrix}, & (2.11) \\ \lambda^7 &= \begin{pmatrix} 0 & 0 & 0 \\ 0 & 0 & -i \\ 0 & i & 0 \end{pmatrix}, & \lambda^8 &= \frac{1}{\sqrt{3}} \begin{pmatrix} 1 & 0 & 0 \\ 0 & 1 & 0 \\ 0 & 0 & -2 \end{pmatrix}. \end{aligned}$$

The normalisation of the structure constants is commonly chosen as

$$\sum_{c,d} f^{acd} f^{bcd} = N\delta^{ab} \quad (2.12)$$

in physics. This implies the following normalisation in the fundamental representation:

$$\text{tr}(T^a T^b) = \frac{1}{2}\delta^{ab}. \quad (2.13)$$

The adjoint representation is defined by

$$(T_{\text{adj}}^a)^{bc} = -if^{abc}. \quad (2.14)$$

These operators act on the vector space of the operators themselves; they are embedded in  $N^2 - 1$ -dimensional matrices, equal to the dimension of the group. The gauge fields transform in the adjoint representation.

A basis-independent characterisation of the representation is given by the quadratic Casimir operator  $C_2(R)$ :

$$T_R^a T_R^a = C_2(R) \mathbb{1}, \quad (2.15)$$

with an implicit sum over  $a$ . This operator commutes with all other operators. After some calculation the Casimirs can be given as

$$C_F \equiv C_2(\text{fund}) = \frac{N^2 - 1}{2N}, \quad C_A \equiv C_2(\text{adj}) = N \quad (2.16)$$

in the fundamental and adjoint representation.

At the end of this section, there will be a collection of relations that will often be used in calculations involving  $SU(N)$ :

$$\text{tr}(T^a T^b) = T_{ji}^a T_{ij}^b = T_F \delta^{ab}, \quad (2.17)$$

$$\sum_a (T^a T^a)_{ij} = C_F \delta_{ij}, \quad (2.18)$$

$$f^{acd} f^{bcd} = C_A \delta^{ab}, \quad (2.19)$$

with the index of the fundamental representation  $T_F = \frac{1}{2}$  and the Casimirs given by (2.16).

## 2.4 Perturbative quantum chromodynamics

To perform perturbative calculations one needs to work out the Feynman rules from the Lagrangian (2.1). A thorough derivation of how this is done can be found in textbooks, so just the final Feynman rules for QCD are given here. Calculations with Feynman rules in QCD are often referred to as perturbative QCD (pQCD).

In the Lagrangian there is a sum over  $N^2 - 1$  free gauge bosons; each single propagator is identical to the propagator of a photon and given by:

$$\nu; b \text{ \scriptsize \textcircled{wavy}} \xrightarrow{p} \mu; a = i \frac{-g^{\mu\nu} + (1 - \xi) \frac{p^\mu p^\nu}{p^2}}{p^2 + i\varepsilon} \delta^{ab}. \quad (2.20)$$

For intermediate states one must sum over all possible gluons.

The ghost propagator is given by:

$$b \text{ \scriptsize \textcircled{dotted}} \xrightarrow{p} a = \frac{i\delta^{ab}}{p^2 + i\varepsilon}. \quad (2.21)$$

For coloured fermions the propagator is given by:

$$j \text{ \scriptsize \textcircled{arrow}} \xrightarrow{p} i = \frac{i\delta^{ij}}{\not{p} - m + i\varepsilon}. \quad (2.22)$$

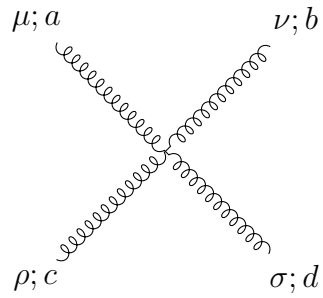
The factors  $\delta_{ij}$  describe the conservation of colour. Colour can be exchanged in interaction vertices between the partaking particles, but propagators describe the movement of (virtual<sup>4</sup>) intermediate states between two vertices, in the language of Feynman diagrams. Therefore the colour must remain unchanged by a propagator, since there is no colour source involved in this movement.

Coming now to the possible interactions in QCD. These are given by terms in the Lagrangian (2.1) that have several different fields in them, giving the possible interactions between the particles of the theory. Pictorially they are given as vertices, with the number of incoming particles dependent on the amount of fields in the interaction term. The first vertex considered here describes the interaction of three gluons, the triple-gluon vertex. All momenta are chosen as incoming, so that  $p + k + q = 0$ . It is given by:

$$\begin{array}{c} \mu; a \\ \swarrow k \\ \text{\scriptsize \textcircled{wavy}} \\ \nu; b \text{ \scriptsize \textcircled{wavy}} \xrightarrow{p} \text{\scriptsize \textcircled{wavy}} \searrow q \\ \rho; c \end{array} = g f^{abc} [g^{\mu\nu} (k - p)^\rho + g^{\nu\rho} (p - q)^\mu + g^{\rho\mu} (q - k)^\nu]. \quad (2.23)$$

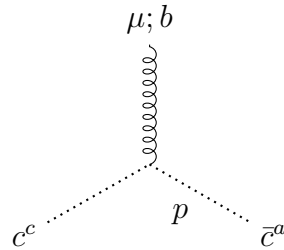
<sup>4</sup>Virtual particle means that the particle obeys  $Q^2 = E^2 - p^2$  where  $Q$  is the virtuality, instead of the normal (on-shell) energy-momentum-relation  $m^2 = E^2 - p^2$  from relativity.

There is also a four-gluon vertex; the momenta are also chosen as incoming:



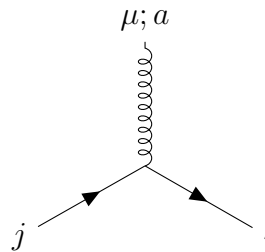
$$\begin{aligned}
 &= -ig^2 \times [f^{abe} f^{cde} (g^{\mu\rho} g^{\nu\sigma} - g^{\mu\sigma} g^{\nu\rho}) \\
 &\quad + f^{ace} f^{bde} (g^{\mu\nu} g^{\rho\sigma} - g^{\mu\sigma} g^{\nu\rho}) \\
 &\quad + f^{ade} f^{bce} (g^{\mu\nu} g^{\rho\sigma} - g^{\mu\rho} g^{\nu\sigma})].
 \end{aligned} \tag{2.24}$$

Ghosts only interact with gluons:



$$= -gf^{abc} p^\mu. \tag{2.25}$$

There is also one vertex for the interaction of gluons and fermions:



$$= ig\gamma^\mu T_{ij}^a. \tag{2.26}$$

Some examples for the calculations of tree-level matrix elements in non-Abelian gauge theories can be found in Appendix A.

## 2.5 Running coupling

With the basics of QCD and group theory covered, the end of this chapter will be a brief discussion of the strong coupling  $g$ . When calculating loop diagrams in QCD to obtain corrections for tree-level processes, one encounters divergent diagrams. Still, physically observable quantities should be finite. To get finite results one employs a technique called renormalisation. The basic idea behind this is that physics at long distances should decouple from the exact physics at short distances, so finite results

can be obtained despite the infinities at short distances in intermediate steps. This also implies that one is able to deform the short-distance behaviour, without changing the long-distance behaviour, by introducing a regulator. Usually one uses an analytic continuation to  $d = 4 - \varepsilon$  dimensions nowadays and takes  $\varepsilon \rightarrow 0$  after the calculation. This regulator introduces an unphysical scale  $\mu$  which in the end should drop out of physical predictions. Also the constants in the Lagrangian (2.1) are not physical quantities and can therefore not be measured as it turns out, they are referred to as eg. the bare charge  $g_0$ . Nevertheless they can be given in terms of measurable quantities, which are called renormalised, with some additional renormalisation factors. These renormalised quantities, identified by the subscript R, have to be measured at some scale  $\mu_R$ . Working in the  $\overline{\text{MS}}$ -scheme usually  $\mu$  will be set equal to  $\mu_R$ . For the strong bare charge one then finds for example:

$$g_0 = g_R \frac{Z_1}{Z_2 \sqrt{Z_3}} \mu^{\frac{4-d}{2}}. \quad (2.27)$$

For calculations one often employs renormalised perturbation theory, meaning that after introducing the renormalized constants one also adds so-called counterterms to the Lagrangian. For example, take the vacuum polarisation graphs:

$$+ \text{ghost loop} + \text{crossed-out gluon loop}, \quad (2.28)$$

with the last graph being the counterterm. Calculating the first four diagrams reveal that the result is composed of a finite and a divergent part. The counterterms are then infinite quantities, chosen in such a way, that they exactly cancel the divergencies appearing in the result of the calculation. QCD has four renormalisation factors and eight counterterms at 1-loop level as it turns out; more details can be found in textbooks.

Now returning to the charge. Since the scale  $\mu$  was artificially introduced, the bare charge can not depend on it, so:

$$\mu \frac{d}{d\mu} g_0 = 0. \quad (2.29)$$

Equations like this are called renormalisation group equations (RGE). But the renormalised charge possesses a scale dependence in its definition. Therefore the behaviour



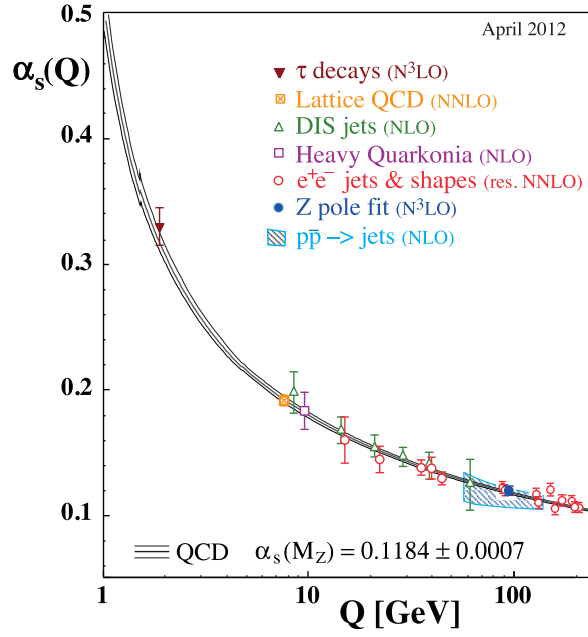


Figure 2.1: Running coupling  $\alpha_s$  in the  $\overline{\text{MS}}$  scheme from experimental data. The current value is  $\alpha_s(m_Z) = 0.1184 \pm 0.0007$ . Image taken from [13].

of the renormalised charge is scale-dependent and governed by the  $\beta$ -function via the equation

$$\mu \frac{d}{d\mu} g_R = \beta(g_R). \quad (2.30)$$

The  $\beta$ -function can be calculated perturbatively. For a 1-loop calculation one finds

$$\beta(g_R) = -\frac{\varepsilon}{2} g_r - \frac{g_R^3}{16\pi^2} \left[ \frac{11}{3} C_A - \frac{4}{3} n_f T_F \right]. \quad (2.31)$$

Now for QCD one defines the strong coupling constant  $\alpha_s = \frac{g^2}{4\pi}$ . Also taking the Casimir operator to be  $N = C_A = 3$ ,  $N_F = \frac{1}{2}$  and  $\varepsilon = 0$  one obtains the 1-loop RGE for QCD:

$$\mu \frac{d}{d\mu} \alpha_s = -\frac{\alpha_s^2}{2\pi} \beta_0, \quad (2.32)$$

with  $\beta_0 = 11 - \frac{2n_f}{3}$ . For the known number  $n_f$  of quark flavours  $\beta_0$  is a positive number. Equation (2.32) can be solved by separation of variables to obtain:

$$\alpha_s(\mu) = \frac{2\pi}{\beta_0} \frac{1}{\ln \frac{\mu}{\Lambda_{\text{QCD}}}}, \quad (2.33)$$

where  $\Lambda_{\text{QCD}}$  is the location of the Landau pole in QCD, i.e. the point at which perturbation theory breaks down. Since  $\alpha_s$  gets smaller for larger scales, this equation is

valid for  $\mu > \Lambda_{\text{QCD}}$ . The strong coupling has to be measured once to fix the Landau pole and afterwards the coupling constant can be calculated at any scale of interest.

Due to the dependence of the coupling on the scale one talks about the “running coupling constant”. Equation (2.33) shows that the coupling becomes large for low energies and small for high energies, so the strong coupling can account for the phenomena of confinement and asymptotic freedom. This behaviour can be verified by experiment, see Figure 2.1. For calculations at tree level one usually identifies the scale  $\mu$  with the momentum of the virtual particle. To get at least an estimator for errors due to the scale uncertainties, one calculates the process several times varying the scale in each run.

## 3 Deep inelastic scattering

The running of the strong coupling can qualitatively motivate the existence of protons and other colourless bound states like mesons or baryons. Though one problem remains: the perturbative methods from the previous chapter are not suited to describe these objects since for the relevant energy scales the strong coupling is large and so perturbation theory breaks down. Calculations on the lattice can show confinement and the formation of bound states, but since the calculations are still very expensive, from a computational standpoint, one is limited to calculating the behaviour of small systems. They are also ill-suited to calculate scattering amplitudes of e.g. two colliding protons. Since historically speaking much knowledge about the fundamental structure of matter was gained through scattering experiments, starting from Rutherford shooting  $\alpha$ -particles at gold foils to discover that atoms had a hard core of size  $\sim 10^{-15}$  m, and the success of QED to describe relativistic scattering experiments involving electrons and positrons, one would hope to be able to relate QCD calculations to scattering experiments. Remembering the running of the strong coupling, these scatterings should happen at high energy scales. A high energy scale is also needed to reveal the substructure of the proton, since the energy of a particle is by de Broglie related to a wavelength and to resolve a structure one needs wavelengths that are smaller than characteristic length scales of the structure. This chapter shows how perturbative QCD calculations can be related to scatterings in the high energy regime, where the strong coupling is small and quarks and gluons can be viewed as essentially free particles.

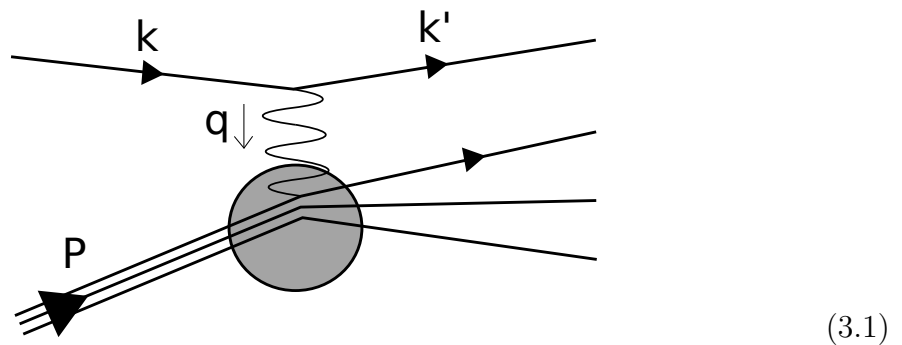
Deep inelastic scattering (DIS) refers to scattering processes at energy scales in which the incident particle, be it a proton or a heavier nucleus, is completely unravelled. Theoretical predictions in this regime are possible, since the problem reduces to the case of scattering point-like particles. For this purpose first the parton model will be given as a general framework. Afterwards corrections to this resulting from QCD are discussed. The last part of this chapter will be spent on the Glauber model, which gives

geometrical factors needed for comparing the results of proton-proton (pp) scattering with e.g. lead-lead (PbPb) scatterings. More detailed derivations can be found in textbooks [37] [40] and referenced papers.

### 3.1 Parton model

Before the advent of QCD, DIS was discussed in the context of the parton model, introduced by Feynman. The parton model states that the substructure of the proton consists of partons, which can be viewed as free particles inside their confinement. These partons would later be identified as quark, antiquarks, gluons and basically every other particle in the SM that can exist in the proton as quantum fluctuations<sup>1</sup>. Now to test the substructure of the proton a probe is needed. High-energetic electrons were first used as a probe, since the interaction of the electron was well understood and more importantly, it can still, for all intents and purposes, be viewed as a point-like particle. So for now DIS processes of the form  $e^-p^+ \rightarrow e^-X$  are considered, where an electron  $e^-$  collides with a proton  $p^+$  and the proton breaks apart. Here X stands for all possible final state that can result from this. A proton starts to break apart, when the involved momentum transfer or the center of mass energy is greater than the mass of the proton.

To get more concrete now consider the following diagram for the process  $e^-p^+ \rightarrow e^-X$ :



with the initial  $k^\mu$  and final  $k'^\mu$  momentum of the electron, the proton momentum  $P^\mu$  and the momentum transfer  $q^\mu = k^\mu - k'^\mu$  via the virtual photon. From this the proton momentum and electron momenta before and after the scattering are the best variables to observe experimentally, so it is useful to express predictions in terms of

<sup>1</sup>At least in principle, but one usually restrains this to quarks and gluons.

these quantities. With  $E$  denoting the energy of the electron and  $\theta$  the angle between the incoming and outgoing electron, the cross section can be written in the lab frame as:

$$\left( \frac{d\sigma}{d\Omega dE'} \right)_{\text{lab}} = \frac{\alpha_e^2}{4\pi m_p q^4} \frac{E'}{E} L^{\mu\nu} W_{\mu\nu}, \quad (3.2)$$

with the leptonic tensor  $L^{\mu\nu}$ , which contains information about polarisations, and the hadronic tensor  $W_{\mu\nu}$ . There are some additional useful variables, which can be used. One is the energy scale of the collision  $Q \equiv \sqrt{-q^2} > 0$  and the Bjorken  $x$ :

$$x \equiv \frac{Q^2}{2P \cdot q}. \quad (3.3)$$

One can contract the two tensors and express the result in terms of the scattering angle:

$$\left( \frac{d\sigma}{d\Omega dE'} \right)_{\text{lab}} = \frac{\alpha_e^2}{8\pi E^2 \sin^4\left(\frac{\theta}{2}\right)} \left[ \frac{m_p}{2} W_2(x, Q) \cos^2 \frac{\theta}{2} + \frac{1}{m_p} W_1(x, Q) \sin^2 \frac{\theta}{2} \right], \quad (3.4)$$

where  $W_1$  and  $W_2$  are newly introduced structure functions, determined by measurements of the angle and energy.

Up to this point only the proton momentum came up, but in the parton model the interaction is between a single parton and the photon. In principle this is nothing new, it still is the known case of scattering with point-like particles, but the momentum of the parton before the scattering is not exactly known. Due to momentum conservation  $p_i^\mu + q^\mu = p_f^\mu$  must hold, with  $p_{i,f}$  being the initial and final momentum of the parton. With the mass  $m_q$  of the parton it follows that

$$m_q^2 + 2p_i \cdot q + q^2 = m_q^2 \quad \implies \quad \frac{Q^2}{2p_i \cdot q} = 1. \quad (3.5)$$

Now while the exact momentum of the parton is unknown, it must have some fraction  $\xi$  of the proton's momentum,  $p_i = \xi P$ . With this  $\xi = \frac{\xi Q^2}{2p_i \cdot q} = x$ , so the Bjorken  $x$  is equal to the fraction of the proton momentum in the parton model. They are often used interchangeably in the literature.

Taking the unknown fractional momentum of a parton into account, the parton model

gives the cross section for  $e^-P^+ \rightarrow e^-X$  scattering as a cross section for  $e^-p_i \rightarrow e^-X$  integrated over all possible momentum fractions and summed over all partons species:

$$\sigma(e^-P^+ \rightarrow e^-X) = \sum_i \int_0^1 d\xi f_i(\xi) \hat{\sigma}(e^-p_i \rightarrow e^-X), \quad (3.6)$$

where  $f_i(\xi)$  are the parton distribution functions (PDFs). They give the probability to find a parton of the species  $i$  with fraction  $\xi$  of the proton momentum. PDFs will be the focus of the next three sections, where more details will be given. A common convention was also introduced in the last equation: partonic quantities wear a hat like the cross section  $\hat{\sigma}$ .

Like already mentioned before, the partonic cross section is just the scattering of point-like particles. Furthermore the cross section at fixed  $x$  should also be independent of  $Q^2$ , a feature known as Bjorken scaling. So the partonic cross section is given by the Rosenbluth formula with form factors  $F_1 = 1$  and  $F_2 = 0$ . These form factors encode the assumption of free partons; generic form factors would violate Bjorken scaling. Inserting the Rosenbluth formula into equation (3.6) one obtains the cross section prediction from the parton model:

$$\left( \frac{d\sigma(e^-P^+ \rightarrow e^-X)}{d\Omega dE'} \right) = \sum_i f_i(x) \frac{\alpha_e^2 Q_i^2}{4E^2 \sin^4 \frac{\theta}{2}} \left[ \frac{2m_p}{Q^2} x^2 \cos^2 \frac{\theta}{2} + \frac{1}{m_p} \sin^2 \frac{\theta}{2} \right], \quad (3.7)$$

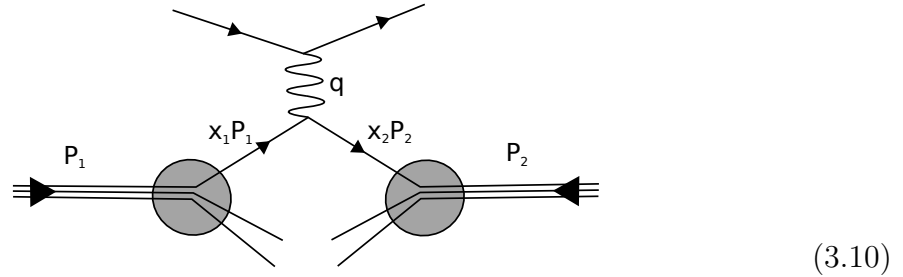
where  $Q_i$  is the fractional charge of the quark. With this equation the form factors of equation (3.2) can be given a concrete form:

$$W_1(x, Q) = 2\pi \sum_i Q_i^2 f_i(x), \quad (3.8)$$

$$W_2(x, Q) = 8\pi \frac{x}{Q^2} \sum_i Q_i^2 f_i(x). \quad (3.9)$$

These form factors fulfil the Callan-Gross relation  $W_1(x, Q) = \frac{Q^2}{4x^2} W_2(x, Q)$ , verifying that quarks are fermions with spin  $\frac{1}{2}$ .

The generalisation of this to proton-proton scattering is straightforward. An example diagram for one possible process looks like this:



(3.10)

Most of the interactions of partons in such collisions will be soft interactions, meaning that only small momentum exchanges are happening. These interactions cannot be treated perturbatively, but soft interactions give a background activity in experiments. In calculations, models of the evolution of this so-called underlying event are sometimes employed. But also some scatterings with high momentum exchange happen; these can be treated like above. For the process exemplified in (3.10) the cross section would look like this:

$$\sigma(p(P_1)p(P_2) \rightarrow YX) = \int_0^1 dx_1 \int_0^1 dx_2 \sum_i f_i(x_1) f_{\bar{i}}(x_2) \sigma(q_f(x_1P) \bar{q}_f(x_2P) \rightarrow Y), \quad (3.11)$$

where the sum runs over all quark flavours,  $Y$  is the final state of the hard interactions and  $X$  denotes the final state of everything else that is going on. In general all possible hard processes in proton-proton collisions that can produce the desired final state have to be taken into account for theoretical predictions. The general form of equation (3.11) still applies for all these processes, but the specific cross section and PDFs that have to be inserted can be different.

## 3.2 Parton distribution functions

Returning to the PDFs now. The PDFs are constructed as probabilities  $f_i(\xi)$  to find a specific parton species  $i$  inside the proton with a fraction  $\xi$  of the total proton momentum. To be used as probabilities the PDFs have to fulfil some constraints. Before these are worked out there are two points that need to be mentioned. As it will turn out at leading order QCD agrees with the parton model, but calculating loops

introduces corrections. Especially noteworthy is the logarithmic violation of Bjorken scaling in  $Q^2$  these corrections introduce and in turn the cross section and PDFs will be dependent on the scale  $Q^2$  of the process. Logarithmic corrections are a general sign of loop corrections and they will be discussed in the next chapter, where the DGLAP equations are at least motivated. Second, it is not obvious that the same PDFs can be used in every calculation i.e. that PDFs can be regarded as universal objects. This requires a proof of factorisation, which shows that short-range physics like the calculation of scatterings can be separated from the long-range physics encoded in the non-perturbative PDFs and so justifies the usage of the same PDFs in different processes. Factorisation will be motivated briefly after the DGLAP equations.

In the constituent quark model the proton consists of one down and two up quarks, also called the valence quarks. A PDF of down or up quarks integrated over all momentum fractions should reproduce these quantum numbers. Since in reality there are quark-antiquark pairs in the proton, one also has to take the PDF  $f_{\bar{q}}$  of the anti-quark into account for the normalisation. Since the quark number is a conserved quantity in QED and QCD this results in

$$\int d\xi [f_u(\xi) - f_{\bar{u}}(\xi)] = 2 \quad (3.12)$$

for the normalisation of the up quark PDFs. Similarly for down quarks:

$$\int d\xi [f_d(\xi) - f_{\bar{d}}(\xi)] = 1. \quad (3.13)$$

The PDFs of the four other quark flavours must obey

$$\int d\xi [f_i(\xi) - f_{\bar{i}}(\xi)] = 0, \quad (3.14)$$

where  $i$  refers to strange, charm, bottom and top quarks. There is no such sum rule associated with the gluon PDF  $f_g$ , since there is no conserved gluon number. It is easy to get the corresponding PDFs for a neutron from this. Due to isospin symmetry the up quark PDF of a proton should be equal to the down quark PDF of a neutron. Additionally all PDFs have to obey a constraint due to momentum conservation. When taking into account the momentum of all partons inside the proton one has to recover the total momentum of the proton:

$$\sum_j \int d\xi [\xi f_j(\xi)] = 1. \quad (3.15)$$



After working out all PDFs for the quarks one can use this last relation to restrain the gluon PDF, assuming that all momentum not accounted for is carried by gluons. To give a feeling for the actual momentum distribution, in a proton about 40% of the momentum is carried by the valence quarks. Depending on scale of the process 30 – 50% of the momentum is carried by gluons and the rest of the momentum is in sea quarks, the quark-antiquark pairs.

There are several collaborations that perform global fits to obtain the PDFs. For these fits, data available from many different processes like  $ep$ ,  $p\bar{p}$ , Drell-Yan process<sup>2</sup> etc. is taken. For a complete list of processes and data used one should check the available papers corresponding to the PDF set of interest. The different groups differ in the way they parametrise their PDFs and the weight they assign to each data set for example.

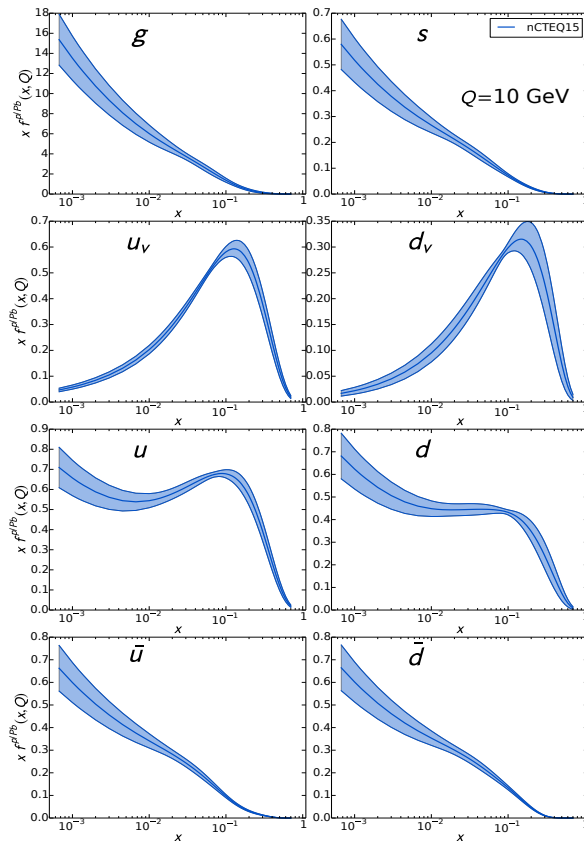


Figure 3.1: The nCTEQ15 fit for bound proton PDFs in lead. Taken from [32].

A further complication arises when theoretical predictions for collisions involving nucleons have to be calculated. Protons inside a larger nucleus have a modified substructure compared to free protons. Ideally, a set of PDFs would have to be constructed for each nucleus, where the constraints from above are modified to the appropriate quantum numbers. In the context of this thesis there will be a comparison between heavy ion collision data from the LHC using lead and theory, so a PDF for lead is needed. But in addition to the more involved analysis as a result of the increase in complexity of the composite objects, there is also less precise experimental data available. Therefore one introduces a modification factor for PDFs that is dependent on the number of protons and neutrons in the nucleus. Also some extra assumptions

<sup>2</sup>Lepton pair production in proton-proton collisions.

have to be made in order to constrain the PDFs over a large kinematic region, since this cannot be done with the available data alone. Collaborations also use different assumptions for these constraints. Nuclear PDFs (nPDFs) are therefore only available with larger uncertainties.

For the calculations in this thesis the nCTEQ15 [32] full nuclear PDFs, which are constructed for direct use in calculation, for lead and the equivalent free proton PDF are used. An example for the lead PDFs can be seen in Figure 3.1. The PDFs  $f_i^{(A,Z)}$  of a nucleus are constructed from PDFs  $f_i^{p/A}$  of bound protons in a nucleus  $A$  and the PDFs  $f_i^{n/A}$  of bound neutrons by

$$f_i^{(A,Z)}(x, Q) = \frac{Z}{A} f_i^{p/A}(x, Q) + \frac{A-Z}{A} f_i^{n/A}(x, Q), \quad (3.16)$$

where  $Z$  is the number of protons and  $A$  is the number of protons and neutrons. The nCTEQ15 PDFs use 16 parameters for their PDFs. To encode the uncertainties of PDFs for calculations of observables 32 error PDFs  $f_k^\pm$  are generated, where a pair of two error PDFs  $f_k^+, f_k^-$  corresponds to the uncertainty of a single parameter. Errors on observables dependent on PDFs can then be calculated as

$$\Delta X = \frac{1}{2} \sqrt{\sum_k (X(f_k^+) - X(f_k^-))^2}. \quad (3.17)$$

### 3.3 DGLAP equations

At leading order, the only process that can contribute to  $e^-p^+$ -scattering is  $\gamma^*q \rightarrow q$ . Returning to equation (3.2) and defining the hadronic tensor  $W^{\mu\nu}$  in terms of partonic quantities  $\hat{W}^{\mu\nu}(z, Q)$  given by the matrix element  $|\mathcal{M}(\gamma^*q \rightarrow X)|^2$  with  $z \equiv \frac{Q^2}{2p_i \cdot q}$ , the form factors  $W_1$  and  $W_2$  are recovered after some calculation. Before working out the corrections for this process it is useful to contract the hadronic tensor with the Minkowski metric  $g^{\mu\nu}$  to obtain the form factor  $W_0 \equiv -g^{\mu\nu}W_{\mu\nu}$ . One can regard  $W_0$  as the cross section for the unpolarised process. For large scales one can give this form factor as

$$W_0(x, Q) = 4\pi \sum_i Q_i^2 f_i(x), \quad (3.18)$$

which is also used as a definition of PDFs. At leading order the independence from  $Q$  still holds. At next-to-leading order there are three diagrams that additionally contribute to this process: A virtual correction diagram and two real-emission diagrams.

(3.19)

The full calculation of these diagrams in  $d = 4 - \varepsilon$  dimensions is lengthy and will not be given here; it can be found in textbooks. But there are a few results from this calculation that are worth highlighting. After having worked out the diagrams, one notices that the virtual diagram has a pole proportional to  $\frac{1}{\varepsilon^2}$ . The same pole exists in the real emissions as well, but to see the cancellation, one has to expand some expressions in  $\varepsilon$  and introduce the plus functions. These are defined as

$$\int_0^1 dz \frac{f(z)}{[1-z]_+} \equiv \int_0^1 dz \frac{f(z) - f(1)}{1-z} \quad (3.20)$$

so  $\frac{1}{[1-z]_+} = \frac{1}{1-z}$  for  $z \neq 1$ . With the help of the plus function one can give the distribution known as the DGLAP<sup>3</sup> splitting function:

$$P_{qq}(z) = C_F \left[ (1+z^2) \left[ \frac{1}{1-z} \right]_+ + \frac{3}{2} \delta(1-z) \right]. \quad (3.21)$$

The splitting function will return later in the context of parton showers. From the partonic structure function one can then again find an expression for the structure function:

$$W_0(x, Q) = 4\pi \sum_i Q_i^2 \int_x^1 \frac{d\xi}{\xi} f_i(\xi) \left[ \delta\left(q - \frac{x}{\xi}\right) - \frac{\alpha_s}{2\pi} P_{qq}\left(\frac{x}{\xi}\right) \left( \frac{2}{\varepsilon} + \ln \frac{\tilde{\mu}^2}{Q^2} \right) + \text{finite} \right] \quad (3.22)$$

<sup>3</sup>For Dokshitzer, Gribov, Lipatov, Altarelli and Parisi.

The remaining pole comes from the parton level and since

$$\int_0^1 P_{qq}(z) dz = 0 \quad (3.23)$$

the total cross section for DIS will be finite, given by integrating  $W_0$  over  $x$  at a fixed  $Q$ . So the physical prediction from DIS is finite, as it should be.  $W_0$  will however be divergent at fixed  $x$ , but the difference of  $W_0$  at scales  $Q$  and  $Q_0$  will be finite:

$$W_0(x, Q) - W_0(x, Q_0) = 4\pi \sum_i Q_i^2 \int_x^1 \frac{d\xi}{\xi} f_i(\xi) \left[ \frac{\alpha_s}{2\pi} P_{qq} \left( \frac{x}{\xi} \right) \ln \frac{Q^2}{Q_0^2} \right]. \quad (3.24)$$

Since QCD is renormalisable  $W_0(x, Q)$  should be finite in a full QCD calculation as well. The last divergence would be cut off by a physical scale like the mass of a quark. But this in turn would introduce new logarithms of the form  $\ln \frac{m_q}{Q}$ . For processes with scales  $Q \gg m_q$  these logarithms would be very large, so that the difference between two scales  $Q$  and  $Q_0$  would still be a more practical quantity. The calculation of differences can be replaced by a calculation with renormalised quantities. For this one says that equation (3.18) is exact at some reference scale  $Q_0$ . Like before with the running coupling, the cross section should be independent of this scale. This independence then leads to a RGE, which governs the dependence of the PDFs on the scale  $\mu$ :

$$\mu \frac{d}{d\mu} f_i(x, \mu) = \frac{\alpha_s}{\pi} \int_x^1 \frac{d\xi}{\xi} f_i(\xi, \mu) P_{qq} \left( \frac{x}{\xi} \right). \quad (3.25)$$

This equation is known as the DGLAP evolution equation. The scale introduced here is called the factorisation scale  $\mu_F$ ; usually it will be set equal to the renormalisation scale, so  $\mu = \mu_R = \mu_F$ . At next-to-leading order, gluons can also be part of the initial state, as can anti-quarks. With the probabilities to find these particles in the initial state, all of the corresponding PDFs actually mix in the RGE. For quarks and gluons the DGLAP equation can thus be given as:

$$\mu \frac{d}{d\mu} \begin{pmatrix} f_i(x, \mu) \\ f_g(x, \mu) \end{pmatrix} = \sum_j \frac{\alpha_s}{\pi} \int_x^1 \frac{d\xi}{\xi} \begin{pmatrix} P_{q_i q_j} \left( \frac{x}{\xi} \right) & P_{q_i g} \left( \frac{x}{\xi} \right) \\ P_{g p_j} \left( \frac{x}{\xi} \right) & P_{g g} \left( \frac{x}{\xi} \right) \end{pmatrix} \begin{pmatrix} f_j(\xi, \mu) \\ f_g(\xi, \mu) \end{pmatrix}, \quad (3.26)$$

with the additional splitting functions

$$P_{qg}(z) = T_F [z^2 + (1-z)^2], \quad (3.27)$$

$$P_{gq}(z) = C_F \left[ \frac{1 + (1-z^2)}{z} \right], \quad (3.28)$$

$$P_{gg}(z) = 2C_A \left[ \frac{z}{[1-z]_+} + \frac{1-z}{z} + z(1-z) \right] + \frac{\beta_0}{2} \delta(1-z). \quad (3.29)$$

In general these functions can be calculated as cross sections of processes like  $g \rightarrow gg$  or  $g \rightarrow q\bar{q}$ , like in [37].

### 3.4 Factorisation

So far everything in this chapter assumes factorisation, meaning that PDFs are universal objects. More exactly, that the cross section of any hadronic process can be written as  $\sigma = f \otimes H + \mathcal{O}\left(\frac{\Lambda_{QCD}}{Q}\right)$  with the PDFs  $f$  and the calculation of the hard process  $H$ . The  $\otimes$  denotes a convolution and also, since this separation cannot be completely right, an error term depending on the scale of the process.

On an intuitive level one can motivate factorisation quite easily. Starting with the scale  $Q$  of the hard process, a time scale  $1/Q$  can be associated with this process. This scale will be larger than the scale of internal processes in the proton. So the time scale of the scattering is much smaller than the time scale of the interaction. Add to that the Lorentz contraction, rendering the proton to be essentially a flat disk from the point of view of the electron. So during the scattering the electron sees a flat disk of frozen particles, which justifies the given notion and usage of PDFs.

Real proofs of factorisation are notoriously difficult, since it has to be shown that all energy scales that turn up in the process are large enough at any given time and many subtleties further obstruct the intuitive picture. And so far it could only be done for a few select processes such as the Drell-Yan process or inclusive DIS. A rigorous proof of the available processes would be way beyond the scope of the thesis.

### 3.5 Parton shower

The perturbative picture developed so far works well for the calculation of processes with small numbers of particles in the initial and final state, like general  $2 \rightarrow 2$  processes. But at high energy experiments a huge amount of particles is measured in detectors, especially in heavy-ion collisions. These particles accumulate into cone-like shapes called jets, streams of particles moving in roughly the same direction. The notion of jets will be the topic of the next chapter. To compare theory against experimental results, Monte Carlo (MC) event generators<sup>4</sup> are used. An important ingredient in these MC generators is a semi-classical approximation, called the parton shower. With the help of parton showers one can get to high multiplicity final states from an initial  $2 \rightarrow 2$  hard process. First the general approach will be described in this chapter, which will afterwards be formulated in a probabilistic fashion suited for MC methods.

As a start consider the real-emissions diagrams  $\gamma^*q \rightarrow qg$  from the DGLAP section again. Working out the cross section in four dimensions leads to

$$|\mathcal{M}|^2 = 2e^2Q_i^2C_Fg_s^2 \left( -\frac{\hat{t}}{\hat{a}} - \frac{\hat{s}}{\hat{t}} + \frac{2\hat{u}Q^2}{\hat{s}\hat{t}} \right), \quad (3.30)$$

with  $\hat{s} = (q + p_i)^2$ ,  $\hat{t} = (p_g - p_i)^2$  and  $\hat{u} = (p_i - p_f)^2$ . The cross section diverges as  $\hat{s}$  or  $\hat{t}$  go to zero, but at fixed incoming momenta the quantity  $\hat{s}$  will be greater than zero. Which leaves the divergence as  $\hat{t}$  goes to zero. Defining  $\theta$  as the angle between the gluon and quark in the center of mass (CMS) frame leads to

$$\hat{t} = (p_g - p_i)^2 = -2p_g \cdot p_i = -4E_gE_i \sin^2\left(\frac{\theta}{2}\right). \quad (3.31)$$

So the divergence in  $\hat{t}$  corresponds to the angle between gluon and quark going to zero, a so-called collinear divergence. One can then show that the emission of a gluon almost collinear to a quark or anti-quark has a universal nature in QCD. In the collinear limit the cross section for a real emission can always be given as

$$d\sigma(X \rightarrow Y + g) = d\sigma(X \rightarrow Y) dt dz \frac{1}{t} \left[ \frac{\alpha_s}{2\pi} C_F \frac{1+z^2}{1-z} + \mathcal{O}\left(\frac{t}{Q^2}\right) \right]. \quad (3.32)$$

---

<sup>4</sup>MC methods are generally defined as algorithms making decisions based upon comparing calculated probabilities with random numbers.

The variable  $t$  can be any variable; often used are the momentum transverse to the beam direction squared  $p_T^2$  [47], the virtuality  $Q$  [54] or the splitting angle  $\theta$  for example. Here  $z$  stands for the energy of the daughter quark after the splitting divided by the energy of the mother quark. Also the DGLAP splitting function  $P_{qq}$  (3.21) returns. The function can be interpreted as the probability for a quark to branch. The probability for a branching in very soft, collinear gluons is the largest, due to the growth with  $\frac{1}{t}$ , but this soft radiation cannot be resolved by detectors. Therefore in simulations the hardest emission is happening, or picked, first and afterwards it is evolved down to the softest emission in a Markov chain process.

Now to get the probability  $R(t)$  to find a gluon at a specific scale  $t$ , at which the collinear limit has to be valid, one has to integrate the splitting function over  $z$ . The energy fraction  $z$  can neither be one nor zero; the constraints can be worked out from kinematics, but the resulting expressions differ with the exact choice of  $t$ , so

$$R(t) = \frac{\alpha_s}{2\pi} C_F \frac{1}{t} \int_{z_{min}(t,Q)}^{z_{max}(t,Q)} dz \frac{1+z^2}{1-z}. \quad (3.33)$$

The Sudakov form factor  $\Delta(t_0, t)$  is defined as the probability to find no gluon between the two scales  $t$  and  $t_0$ . The calculation of the Sudakov factor is best done when considering infinitesimal shifts  $\delta t$  of the scale  $t$ . This can be expanded in a Taylor series  $\Delta(t_0, t + \delta t) = \Delta(t_0, t) + \delta t \frac{d}{dt} \Delta(t_0, t)$ . This also leads to

$$\Delta(t_0, t + \delta t) = \Delta(t_0, t) \left( 1 - \int_t^{t+\delta t} dt' R(t') \right) = \Delta(t_0, t) - R(t) \delta t \Delta(t_0, t). \quad (3.34)$$

From the two expressions a differential equation for  $\Delta(t_0, t)$  can be derived:

$$\frac{d}{dt} \Delta(t_0, t) = -R(t) \Delta(t_0, t). \quad (3.35)$$

With the condition  $t_0 = Q^2$  the solution of the differential equation is given by

$$\Delta(Q, t) = \exp \left( - \int_t^{Q^2} \frac{dt'}{t'} \int_{z_{min}}^{z_{max}} dz \frac{\alpha_s}{2\pi} C_F \frac{1+z^2}{1-z} \right). \quad (3.36)$$

So far, again, only the splitting of a quark into a quark and gluon was considered, but in calculations all possible splittings have to be considered. Also, after the initial splitting further splittings can happen. The starting scale in the form factor is then the scale  $t_h$  after the splitting, down to a cut-off scale  $t_c$ , which is usually of order  $\mathcal{O}(1 \text{ GeV}^2)$ . With this the Sudakov factor [36] becomes:

$$\Delta_a(t_h, t_c) = \exp\left(-\int_{t_c}^{t_h} \frac{dt'}{t'} \int_{z_{min}}^{z_{max}} dz \sum_b \frac{\alpha_s}{2\pi} P_{ab}(z)\right), \quad (3.37)$$

describing the probability that a mother parton  $a$  emits no resolvable radiation between the two scales. With this iterative procedure the many-particle final state can be reduced to the calculation of a hard  $2 \rightarrow 2$  process with subsequent splitting. This framework describes how final state radiation (FSR) is generated, but it is also possible to get radiation from the two incoming particles before the collisions. The usual strategy here is to first select a hard process and then evolve the two initial partons back in time. For this initial state radiation (ISR) the Sudakov factor has to be modified by

$$\Delta_a^{(IS)}(t_h, t_c, x) = \frac{f(x, t_c)}{f(x, t_h)} \Delta_a(t_h, t_c), \quad (3.38)$$

where  $f(x, t)$  are the PDFs. Here one views the probability of the parton being part of some mother parton at a higher scale. Constraints are set by the scale of the hard scattering as the lower limit and the maximum possible scale of the parton in the proton as the upper limit.

As closing remark for this section, the Sudakov factor performs a leading logarithmic resummation, which sends the previously divergent cross section for the emission of the hardest gluon at a given scale in the case  $t = 0$  to  $\sigma = 0$ . More information about the parton shower can be found in [36] and [46].

## 3.6 Hadronisation/Fragmentation

After calculating the hard process and evolving the initial outgoing partons via parton shower down to a multiparticle final state, one final component is still missing. The objects that remain after the parton shower are quarks and gluons, coloured objects. But as previously stated, only colour-neutral objects can be observed in detectors.



So one needs a mechanism to bind the quarks into hadrons (qqq-states) and mesons (q $\bar{q}$ -states). For this, phenomenological models have to be used, since this mechanism sets in at scales where perturbative methods break down. This mechanism is called fragmentation or (often used interchangeably) hadronization. Technically speaking fragmentation describes the initial formation of hadrons and mesons. These states can afterwards still decay and hadronisation includes the decay of the heaviest meson and baryon states down to the pseudostable states detected in experiments. One model, the Lund string model, will be discussed briefly. Further information about the exact implementation in PYTHIA 6 is given in their extensive manual [46].

The Lund string model is built upon the QCD potential of a quark-antiquark pair, that together form a colour singlet. This potential can approximately be given as

$$V_{\text{QCD}}(r) \approx -\frac{4}{3} \frac{\alpha_s}{r} + \kappa r, \quad (3.39)$$

where  $r$  is the distance between them and  $\alpha_s$  is the strong coupling [26]. From lattice calculations the string tension is  $\kappa \approx 1 \text{ GeV/fm}$ . Consider the case of a single initial quark-antiquark pair  $q_0\bar{q}_0$  being produced in a collision. The distance between them will grow with time after the collision, which is why the first term in the potential can usually be ignored. This increasing distance leads to an increase in potential energy, so that at some point a new pair  $q_1\bar{q}_1$  can be formed from the vacuum, leading to two colour singlets  $q_0\bar{q}_1$  and  $q_1\bar{q}_0$ , which is an energetically favourable configuration. This is also referred to as string breaking. For this it is also assumed that the colour of the produced pair match the original colour. These new pairs can then be subjected to string breaks as well, leading to the production of many new  $q\bar{q}$ -pairs.

What has to be considered now is which fraction  $z$  of the initial energy and longitudinal momentum  $E + p_z$  the hadron obtains. This is governed by the fragmentation function  $f(z)$ , which gives a probability for a fraction  $z$ . In the program a choice has to be made whether to start the fragmentation process from the quark or antiquark, but since this is arbitrary the final result should not depend on this. With this symmetry condition  $f(z)$  can be given as the Lund symmetric fragmentation function:

$$f(z) \propto \frac{1}{z} z^{a_\alpha} \left( \frac{1-z}{z} \right)^{a_\beta} \exp \left( -\frac{bm_\perp^2}{z} \right). \quad (3.40)$$

Where there is an  $a$  for each flavour, while usually picking all  $a_{\alpha,\beta}$  to be the same, and  $m_{\perp} = m^2 + p_x^2 + p_y^2$  is the transverse mass, with the direction of movement being along the  $z$ -axis.

To obey local conservation of flavour a  $q\bar{q}$ -pair has to be formed at one point. This is strictly speaking only possible if the pair has no transverse momentum or mass; otherwise they would have to be created at a certain distance, so that the field energy between them can be transformed into the transverse masses. To obtain pairs with a (common) transverse momentum tunneling can be used, the pair is then created at one point to obey flavour conservation and instantly tunneled to the appropriate distance. The corresponding probability can be given as

$$\exp\left(-\frac{\pi m_{\perp}^2}{\kappa}\right) = \exp\left(-\frac{\pi m^2}{\kappa}\right) \exp\left(-\frac{\pi p_{\perp}^2}{\kappa}\right), \quad (3.41)$$

where  $p_{\perp}$  is the transverse momentum.

After all the flavours of the  $q\bar{q}$ -pairs have been chosen, they have to be assigned to a meson multiplet. In PYTHIA 6 six meson multiplets, characterised by the valence quark spin  $S$  and internal angular momentum  $L$  coupling to  $J = L + S$ , are included. First the spin is chosen according to a probability based on the quark content of the meson. The default behaviour then is to assign  $L = 0$ , but it is possible to produce  $L = 1$  if wished. Then there are four additional probabilities, corresponding to the four possible states with  $L = 1$ . Baryons, which contain three quarks, have to also be included in this procedure somehow, since they are observed in experiments. But the production of baryons does not follow as nicely from the picture of the Lund string model, which inserts only new  $q\bar{q}$ -pairs. There is no unique generalisation to include baryons. There are three scenarios in PYTHIA: diquarks, simple and advanced popcorn. The diquark scenario just states, that instead of a quark-pair a diquark-pair in a colour triplet could be produced and subsequently form baryons. This happens basically as before, where probabilities to produce the various diquarks are given. In the popcorn scenarios the basic idea is that the formed quarkpair does not need to have the same colour as the original pair in every case. If the new pair also drifts apart a second pair can be formed between them, leading to configurations in which two baryons can be formed.

### 3.7 Glauber model

The Glauber model was originally formulated as an approach to quantum-mechanical scattering with composite particles. For usage in relativistic heavy-ion physics it is nowadays mostly used with regards to nuclear geometry. By introducing quantities like the number of participants  $N_{\text{part}}$  or the number of binary nucleon-nucleon collisions  $N_{\text{coll}}$  it makes comparisons between different reaction systems or measurements in different centrality bins possible. The notion of centrality will be briefly discussed later. The main relevance for this thesis is the application of the Glauber model to the particle production in pp and PbPb collisions. Due to factorisation, the only difference between collisions of the two systems should be an increase in parton flux for the PbPb collisions. This increase should correspond to a scaling of the particle yield with  $N_{\text{coll}}$ , the number of binary collisions. At least in the absence of any nuclear effects, violations of this relation are used to study the properties of the medium formed during heavy-ion collisions. More details on this will be given in chapter 5. For a more extensive review of the Glauber model see [35].

The collision of two nuclei can be formulated in terms of the interactions of individual constituent nucleons. This is done in the optical limit, meaning the high energy regime. There the overall phase shift of the collision is the sum over all phase shifts from two-nucleon interactions. The phase shift can be related to a cross section with the optical theorem. The model is based on some assumptions, namely that the nucleons can move independently inside the nucleus and that the nucleus is large compared to the nucleon-nucleon force.

Take now two heavy ions colliding at relativistic speed with an impact parameter  $\mathbf{b}$ , a vector characterising the distance between the center of the projectile B and the target A. For a sketch of the situation see Figure 3.2. This choice of naming is also used for experiments with two colliding beams. Consider a tube located at a displacement  $\mathbf{s}$  from the center of the target. The probability to find a nucleon per unit transverse area in this tube is given by:

$$T_A(\mathbf{s}) = \int \rho_A(\mathbf{s}, z_A) dz_A , \quad (3.42)$$

where  $\rho_A$  is the probability per unit volume for finding the nucleon at  $(\mathbf{s}, z)$ . There will be an overlap between this target tube and a tube in the projectile, displaced from

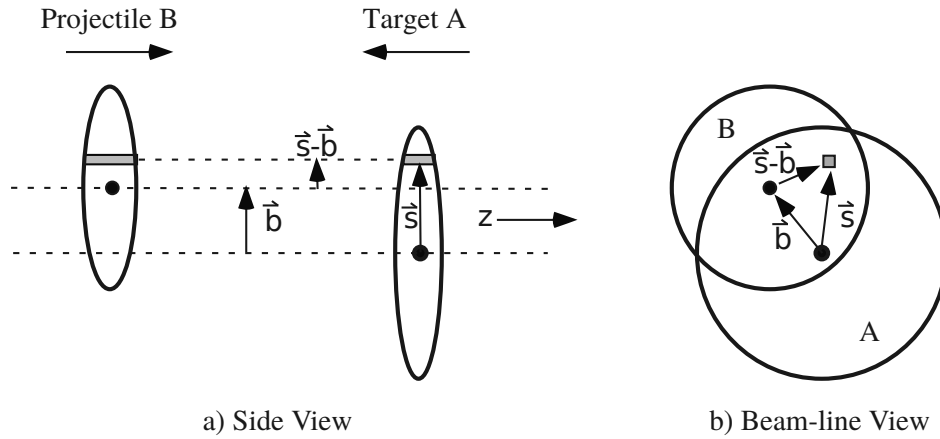


Figure 3.2: Sketch of the optical Glauber model geometry. Image taken from [35].

the center by  $\mathbf{s} - \mathbf{b}$ . The same expression holds for finding a nucleon in the projectile tube. With the help of these probabilities one can define the thickness function  $T(\mathbf{b})$ , giving the joint probability per unit area of nucleons being in the target and projectile tubes of differential area  $d^2s$ :

$$T_{AB}(\mathbf{b}) = \int T_A(\mathbf{s})T_B(\mathbf{s} - \mathbf{b}) d^2s \quad (3.43)$$

$T(\mathbf{b})$  can be interpreted as the overlap area in which a nucleon from A can interact with a nucleon from B. The probability of such an interaction happening can then be given by  $T(\mathbf{b})\sigma_{\text{inel}}^{\text{NN}}$ , where  $\sigma_{\text{inel}}^{\text{NN}}$  is the inelastic nucleon-nucleon cross section. As  $\sigma_{\text{inel}}^{\text{NN}}$  entails processes with low momentum transfers it cannot be calculated in pQCD and has to be measured in experiments. With the probability of one nucleon-nucleon interaction the probability of having  $n$  such interactions between nucleus A and B can be given by a binomial distribution:

$$P(n, \mathbf{b}) = \binom{AB}{n} [T_{AB}(\mathbf{b})\sigma_{\text{inel}}^{\text{NN}}]^n [1 - T_{AB}(\mathbf{b})\sigma_{\text{inel}}^{\text{NN}}]^{AB-n}. \quad (3.44)$$

Concerning the notation, a nucleus A consists of  $A$  nucleons and a nucleus B contains  $B$  nucleons. From this a total probability for an interaction between A and B is given by

$$\frac{d^2\sigma_{\text{inel}}^{\text{A+B}}}{db^2} \equiv p_{\text{inel}}^{\text{A+B}}(b) = \sum_{n=1}^{A+B} P(n, \mathbf{b}) = 1 - [1 - T_{AB}(\mathbf{b})\sigma_{\text{inel}}^{\text{NN}}]^{AB}. \quad (3.45)$$

For unpolarised scatterings the impact parameter can be given by a scalar distance. The total cross section can then be found through

$$\sigma_{\text{inel}}^{A+B} = \int_0^{\infty} 2\pi b \left\{ 1 - [1 - T_{AB}(\mathbf{b})\sigma_{\text{inel}}^{\text{NN}}]^{AB} \right\} db . \quad (3.46)$$

The total number of nucleon-nucleon collisions can be calculated as

$$N_{\text{coll}}(b) = \sum_{n=1}^{AB} nP(n, b) = AB T_{AB}(b)\sigma_{\text{inel}}^{\text{NN}} . \quad (3.47)$$

Lastly the number of participants, or the number of wounded nucleons (i.e. the number of nucleons that interact from A and B at impact parameter  $b$ ) is given by

$$N_{\text{part}} = A \int T_A(\mathbf{s}) \left\{ 1 - [1 - T_B(\mathbf{s} - \mathbf{b})\sigma_{\text{inel}}^{\text{NN}}]^B \right\} d^2s + \\ B \int T_B(\mathbf{s} - \mathbf{b}) \left\{ 1 - [1 - T_A(\mathbf{s})\sigma_{\text{inel}}^{\text{NN}}]^A \right\} d^2s . \quad (3.48)$$

These quantities are most often calculated in Monte Carlo implementations. There a discrete collection of nucleons is generated according to the probability  $\rho_A$  in three dimensions, as opposed to the continuous distributions used in the optical limit. Afterwards a random impact parameter is chosen from the distribution  $\frac{d\sigma}{db} = 2\pi b$ . The nucleons now travel in straight lines along the beam axis. Also  $\sigma_{\text{inel}}^{\text{NN}}$  is assumed to be independent of prior collisions of a given nucleon. A collision then takes place, in the simplest models, if the distance  $d$  between the two nucleons, in the plane orthogonal to the beam axis, satisfies  $d \leq \sqrt{\sigma_{\text{inel}}^{\text{NN}}/\pi}$ .

These Glauber quantities are not directly measurable quantities though. But mean values for them can be calculated in MC simulations and afterwards be connected to measurements from an experiment. For that one defines centrality classes in the measured distribution and the calculated distribution. The distributions share the same average Glauber quantities per centrality bin. The underlying assumption of centrality classes is that the impact parameter is directly and monotonically related to the number of produced particles. For large impact parameters one expects to find only a small amount of particles at mid rapidity and a large amount of particles in the beam direction. These collisions are called peripheral. Whereas for small impact parameters,

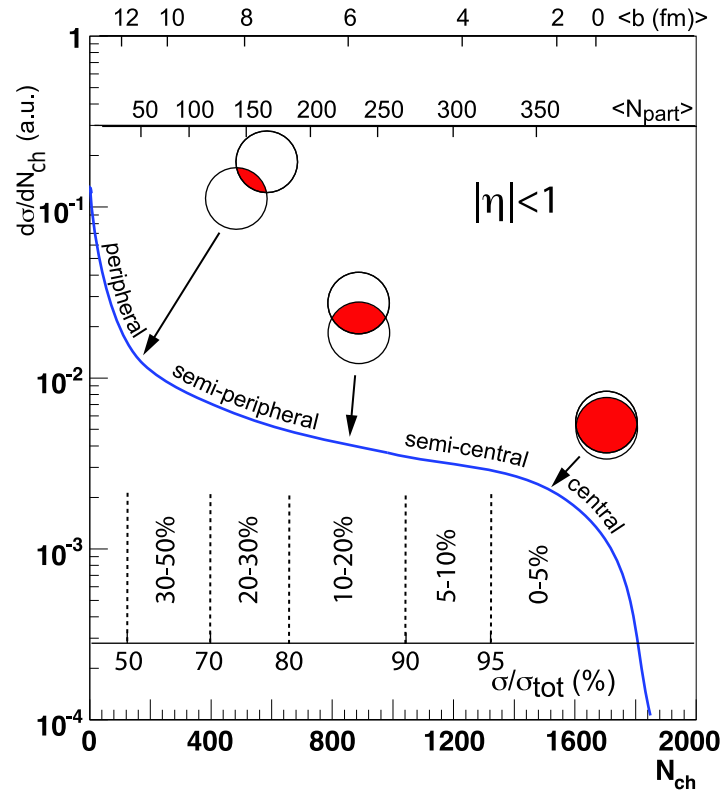


Figure 3.3: Illustration of the relation between the Glauber quantities and a final state observable. Taken from [35].

called central collisions, the reverse applies. In particle physics the rapidity, with the momentum along the beam axis  $p_z$ , is defined as

$$y = \frac{1}{2} \ln \frac{E + p_z}{E - p_z}. \quad (3.49)$$

Rapidity defined this way gives the boost needed along the beam axis from the lab frame to the frame in which the particle moves exactly perpendicular to the beam axis. Also the difference between the rapidities of two particles is invariant under Lorentz boosts. Alternatively the pseudorapidity  $\eta = \ln \left[ \tan \frac{\theta}{2} \right]$  is often used, since it is easier to measure in experiment. For massless particles or very high energies this is equivalent to the rapidity. For an illustration of centrality see Figure 3.3, which shows the relation between measurable quantities and Glauber parameters. The binning in centrality classes is done after an ensemble of events has been measured. Then the total integral of the distribution can be calculated. A centrality class is defined as a

fraction of the total integral. A centrality of 10 – 20% for example is defined by the boundaries which satisfy

$$\frac{\int_{\infty}^{n_{10}} \frac{dN_{\text{evt}}}{dN_{\text{ch}}} dN_{\text{ch}}}{\int_{\infty}^0 \frac{dN_{\text{evt}}}{dN_{\text{ch}}} dN_{\text{ch}}} = 0.1 \quad \text{and} \quad \frac{\int_{\infty}^{n_{20}} \frac{dN_{\text{evt}}}{dN_{\text{ch}}} dN_{\text{ch}}}{\int_{\infty}^0 \frac{dN_{\text{evt}}}{dN_{\text{ch}}} dN_{\text{ch}}} = 0.2, \quad (3.50)$$

where  $\frac{dN_{\text{evt}}}{dN_{\text{ch}}}$  is used as an example distribution corresponding to the number of charged particles produced in an event. These boundaries do not need to be identical for the measured and simulated distributions.

## 4 Jets

After establishing the theoretical tools to calculate predictions for scattering experiments with high particle multiplicities in the final state, it is now time to expand on the notion of jets. A jet is an obvious structure in detectors, consisting of many particles travelling in roughly the same direction. With this picture of jets a relation to the initial parton seems intuitive. The radiation from the initial parton due to the shower will mostly still travel in the same direction and by gathering all energies from the particles in a jet one relates this to the original parton and can therefore study parton distributions in the proton for example. Another usage of jets is the identification of decaying heavy particles. A jet can also stem from the additional emission of the gluon; the rate of jet production can then give information about the underlying process. One should keep in mind though that the identification of a jet coming from a single parton is ambiguous. Still the measurement of inclusive jet properties and also of the substructure are important sources of information. For a more extensive review see [38].

A jet is not a uniquely defined object; there are many different definitions of jets, mostly due to them being an essential part of many varied experiments over the last 30 years. It is not obvious what the "perfect" definition of a jet should be. So a jet definition is a set of rules by which criteria to gather particles into a jet and how to assign a momentum to the final jet. There are some agreed-upon guidelines of what general properties a jet definition should possess. These are gathered in the "Snowmass accord", which reads as follows:

1. Simple to implement in an experimental analysis.
2. Simple to implement in the theoretical calculation.
3. Defined at any order of perturbation theory.



4. Yields finite cross sections at any order of perturbation theory.
5. Yields a cross section that is relatively insensitive to hadronisation.

Jet definitions can be separated into two distinct categories: cone algorithms and sequential recombination algorithms. The first kind takes a cone of given radius  $R$  and uses the fact that branching and hadronisation leave the energy flow mostly unchanged. The radius  $R$  is a measure of distance in the plane spanned by the azimuthal angle  $\phi$  and the (pseudo-) rapidity ( $\eta$ )  $y$ . Cone algorithms are just mentioned for completeness and will not be discussed here. The different kinds of sequential recombination algorithms generally work in a similar fashion. Some sort of distance measure is introduced, a pair of particles that is closest with regards to this measure is then combined into a single particle. This process is repeated until only particles remain that fulfil a threshold condition; the remaining objects are called the jets. So sequential recombination can be seen as "reversing" the probabilistic splitting generated by the parton shower. An important factor in determining which jet algorithm to use was the difference in computation time. In the past, most sequential recombination algorithms were not usable for jet clustering of events with many particles, since their computation time scaled with the number of particles  $N^3$ . But with improvements in numerical techniques this has mostly been resolved: the anti- $k_T$  algorithm now only scales with  $N \ln N$ . A further important property of jet algorithms is the infrared and collinear (IRC) safety. An algorithm is IRC safe if the introduction of an arbitrary amount of "ghost" particles, particles with basically no energy or momentum, to the event does not change the properties of the jet, like its momentum or its active area.

The anti- $k_T$  algorithm is an example of a sequential recombination algorithm. It will be used later as the jet definition in calculations. This algorithm is IRC safe and has the nice property to produce circular jets around a hard seed. A comparison between different jet algorithms and the shapes they produce can be seen in Figure 4.1. The anti- $k_T$  algorithm introduces two distance measures:

$$d_{ij} = \min(p_{T_i}^{-2}, p_{T_j}^{-2}) \frac{\Delta R_{ij}^2}{R^2}, \quad \Delta R_{ij}^2 = (y_i - y_j)^2 + (\phi_i - \phi_j)^2, \quad (4.1)$$

$$d_{iB} = p_{T_i}^{-2}, \quad (4.2)$$

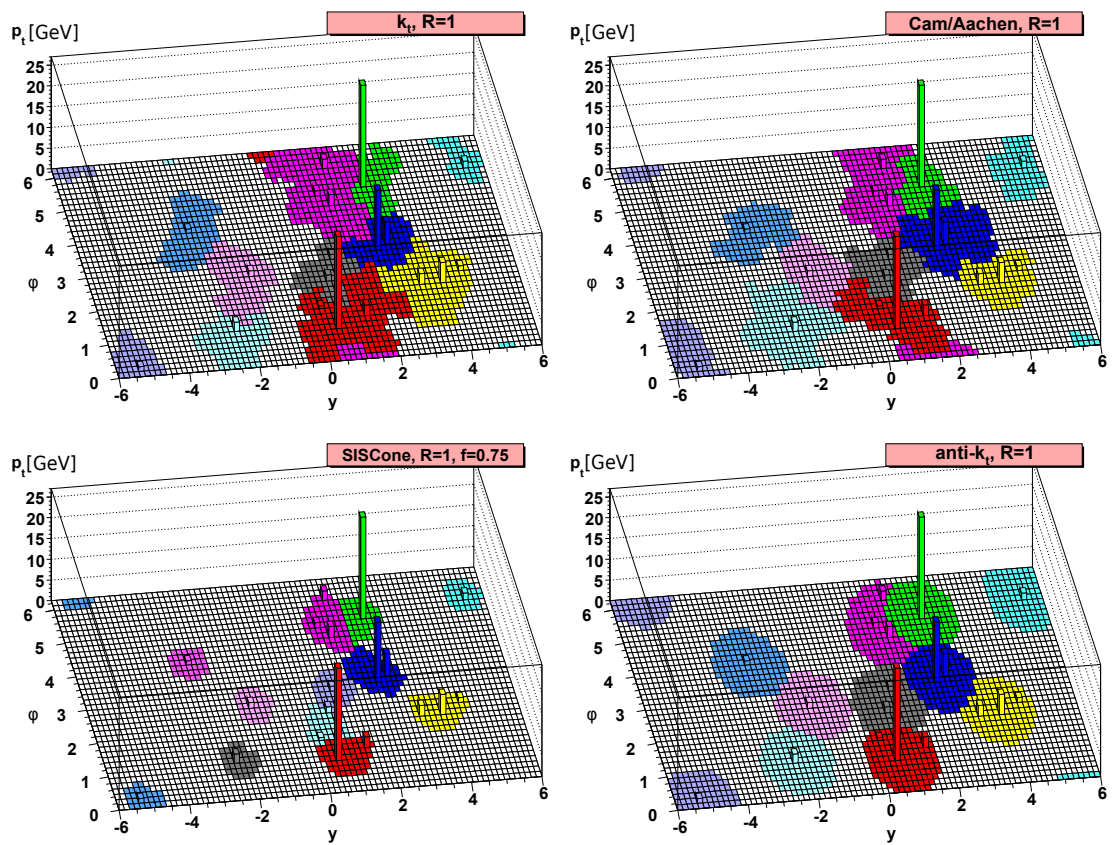


Figure 4.1: Example of clustering for a generated parton-level event with four different jet algorithms and an ensemble of soft "ghosts". The shaded area corresponds to the active area of the jet. Taken from [38].

where  $d_{ij}$  is a dimensionful distance between two particles  $i$  and  $j$ , given by the minimum of their squared transverse momentum and their distance in the rapidity-azimuthal angle plane, and  $d_{iB}$  is a distance used for defining final jets. These distance measures are invariant under longitudinal boosts. The algorithm then works as follows:

1. Work out all the  $d_{ij}$  and  $d_{iB}$  in an event.
2. Find the minimum of all distance measures.
3. If this is a  $d_{ij}$ , combine the particles  $i$  and  $j$  into a new particle and return to step 1.
4. If this is a  $d_{iB}$  declare  $i$  to be a jet and remove it from the particle list. Return to step 1.
5. Stop when no particles remain.

In this algorithm jets are fundamentally determined by the parameter  $R$ ; if no particle remains in a distance  $R$  then the particle will become a jet. Also all particles of the event will be included in a jet. This can lead to arbitrary soft particles becoming jets, therefore it is common to also specify a minimum amount of transversal momentum a jet should have. To give this momentum to a jet, a recombination scheme has to be used. Most widely used is the E-scheme or the four-vector recombination scheme. When merging two particles their corresponding four-vectors are just added. For comparison between experiment and calculation the same jet algorithm has to be used. The implementation of the anti- $k_T$  algorithm used later is provided by the FastJet package [17].

## 5 Quark-gluon plasma

After having worked out the behaviour of the fundamental building blocks of matter and being able to compare theoretical predictions to experimental measurements there are several questions one might ask: are there other states of matter and if these exist, how do transitions between these states happen? Our general understanding of physics works well for the densities of matter we encounter around us, from the 1 nucleon/m<sup>3</sup> density of the universe to the density of heavy nuclei of about 10<sup>14</sup> nucleon/m<sup>3</sup>. But we know of scenarios where the density should be much larger than this, for example in the early universe. Due to the expansion the universe tends towards lower densities, but shortly after the Big Bang there should have been a state of extreme density, by reversing this logic and going to higher density states of the universe if time runs backwards. And this very early state of the universe can correspond to a new state of matter. That such a new state should emerge at some point can be illustrated quite intuitively. Starting from a gas of nucleons, which usually possesses densities of about 10<sup>30</sup> nucleon/m<sup>3</sup>, as the low-density state of matter, the nucleons of the gas can form nuclei, where heavy nuclei possess a density of 10<sup>14</sup> nucleon/m<sup>3</sup>, like mentioned before. A schematic view of this can be seen in Figure 5.1, where the gas or atomic state corresponds to (a) and a heavy nucleus to (b). Increasing the density further leads to quark matter (c); the transition happens, as it turns out, at densities of 10<sup>15</sup> nucleon/m<sup>3</sup>. Using the fact that nuclei possess a substructure gives an intuitive understanding of why this happens. With increasing density the constituents of the nuclei come close to one another and at some point these constituents "forget" to which nucleus they originally belonged, forming an area of "free" quarks and gluons, the quark-gluon plasma (QGP). Of course quarks and gluons are not really free, rather the amount of other coloured particles in the direct vicinity renders the notion of bound states in this area obsolete. This is also enhanced by the effect of charge screening, known from solid state physics, which reduces the range of the strong force

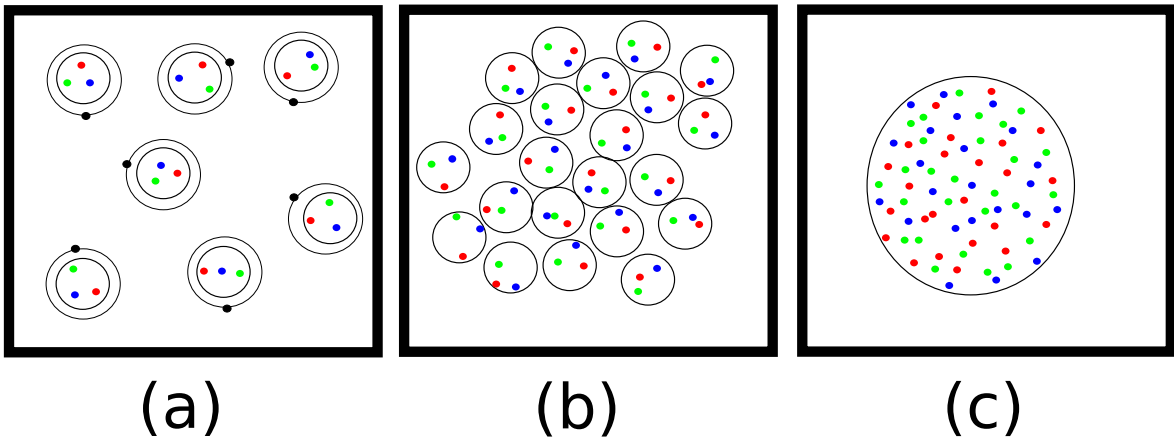


Figure 5.1: Schematic view for (a) atomic, (b) nuclear and (c) quark matter, corresponding to an increase in density. Taken from [39].

exponentially with the colour charge density, suppressing the development of long range effects.

The exact nature of this transition is still unknown though and under active investigation. An important source of information are calculations on the lattice. These calculations are e.g. calculations of the energy density with regard to the dependence on temperature. From the understanding of the running coupling it should be no surprise that this transition can also happen after a sufficient increase in temperature. There a significant growth in energy density is observed at temperatures around 170 MeV, which is in good agreement with values obtained from experimental observations. There are only few degrees of freedom in the low-temperature regime, corresponding to bound matter. The sudden increase in density corresponds to an increase in degrees of freedom. An in-depth discussion about phase transitions would require to involve renormalisation, scaling critical exponents and corresponding universality classes and will not be done here. Also there is debate about exactly what kind of medium is formed in experiments. Competing models are a plasma of quarks and gluons or a colour glass condensate. A more detailed account can be found here [39]. For the purpose of this thesis it is sufficient to state that a transitions happens at all.

In experiments the creation of this new state of matter is achieved in relativistic heavy nucleus collisions. For this a large amount of energy is deposited in a small area during a collision, heating the system up. This energy also leads to the production of new particles; one can show that after a certain energy threshold every further increase in energy directly goes into the production of new particles and not into further heating

the system, so a very high density is achieved. The next section will be a brief review of a model governing the spatial-temporal evolution of the QGP. After having established a model for the evolution of the medium, there will be a discussion about what can be learned about this medium from experiment. The focus will be put onto jet quenching, but other aspects will be briefly mentioned.

## 5.1 Bjorken Model

The Bjorken model is a 1D model of the space-time evolution in the central rapidity region after nucleus-nucleus collisions [14]. It formulates the evolution of the energy density in the context of a Landau hydrodynamic model. For hydrodynamics to be applicable it assumes that the medium reaches thermal equilibrium shortly after the collision, which is after 1 fm. Also assumed is the existence of a symmetric central-plateau, so that particle production is a function of rapidity. This implies that the evolution of the system is the same in every center-of-mass frame. In these frames the nuclei are flat disks or "pancakes", due to Lorentz contraction, receding from the collision at nearly the speed of light. So a symmetry is imposed on the initial conditions, which is respected by the hydrodynamic equation. Also implied by this is that the initial energy density is Lorentz-invariant and so is then necessarily the time evolution of the medium. The fluid should expand longitudinally and homogeneously near the collision axis  $z$  of the heavy nuclei in this model. While the fluid is at rest in the center of the collision, it should pick up a velocity  $z/t$  when moving away from this point, where  $t$  is the time after the collision. Of course this simplified approach only holds for short times scales. After some time, about 5 – 10 fm, transversal flows and a three-dimensional expansion take place, which leads to a rapid cooling of the medium. It is assumed that the medium very quickly goes out of thermal equilibrium at this stage. A complicated behaviour of (unstable) flows is expected here and pion production could take place in outer, cooler layers of the fluid. This behaviour is not described by the Bjorken model.

The applicability of hydrodynamics means that a local energy density  $\epsilon(x)$ , pressure  $p(x)$ , temperature  $T = \beta^{-1}(x)$  and four-velocity  $u_\mu(x)$  exist. For the velocity  $u^2 = u_\mu u^\mu = 1$  holds. With this, the energy-momentum tensor can be given as:

$$T_{\mu\nu} = (\epsilon + p)u_\mu u_\nu - g_{\mu\nu}p. \quad (5.1)$$

The tensor is a conserved quantity

$$\frac{dT_{\mu\nu}}{dx_\mu} = 0. \quad (5.2)$$

Natural variables for this problem are the proper time  $\tau = \sqrt{t^2 - z^2}$  and the rapidity  $y$ . But since the initial conditions are invariant under boosts, there should be no dependence on the later, therefore the evolution is completely governed by the proper time  $\tau$ . The variables and their initial conditions can thus be given as:

$$\epsilon = \epsilon(\tau) \quad \text{with} \quad \epsilon(\tau_0) = \epsilon_0, \quad (5.3)$$

$$u_\mu = \frac{\tilde{x}_\mu}{\tau} \quad \text{with} \quad u_\mu(\tau_0) = \frac{1}{\tau_0}(t, 0, 0, z) \equiv \frac{\tilde{x}_\mu}{\tau_0}. \quad (5.4)$$

Making use of the derivatives of the proper time and velocity with respect to  $x_\mu$  one can simplify equation (5.1) to

$$\frac{d\epsilon}{d\tau} = -\frac{(\epsilon + p)}{\tau}. \quad (5.5)$$

Requiring that the trace of  $T_{\mu\nu}$  is positive implies that  $\epsilon \geq 3p$ , which leads to

$$\left(\frac{\tau_0}{\tau}\right)^{\frac{4}{3}} \leq \frac{\epsilon(\tau)}{\epsilon(\tau_0)} \leq \left(\frac{\tau_0}{\tau}\right) \quad (5.6)$$

for equation (5.5). An ideal relativistic fluid has  $\epsilon = 3p$  and therefore a proper-time dependence of  $\tau^{-\frac{4}{3}}$ . Another feature of the hydrodynamic Landau model is the conservation of entropy  $S$ . An entropy density can be given as  $s = \frac{S}{V} = \beta(\epsilon + p)$  with a corresponding entropy current  $s_\mu \equiv su_\mu$ . A local conservation

$$\frac{ds_\mu}{dx_\mu} = 0 \quad (5.7)$$

is obtained by contracting equation (5.2) with  $u^\nu$ , which also gives

$$\frac{ds}{d\tau} = -\frac{s}{\tau}. \quad (5.8)$$

This equation governs the proper-time dependence of the entropy density, leading to

$$s(\tau) = s(\tau_0) \frac{\tau_0}{\tau}. \quad (5.9)$$

The model could thus be defined by giving an initial entropy density. The time dependence of the fluid can also be calculated. Starting again from equation (5.5) and expanding the derivative yields:

$$\frac{d\epsilon}{d\tau} = \frac{d\epsilon}{dp} \frac{dp}{dT} \frac{dT}{d\tau} = -\frac{(\epsilon + p)}{\tau} = -\frac{T s}{\tau}. \quad (5.10)$$

It is known from thermodynamics that the pressure is related to the free energy  $F$  and the volume  $V$  via  $p = -\frac{F}{V}$ . With the entropy  $S = -\left.\frac{dF}{dT}\right|_V$  it follows that

$$\frac{dp}{dT} = \frac{S}{V} = s. \quad (5.11)$$

Using the sound velocity

$$\frac{d\epsilon}{dp} = \frac{1}{v_s^2} \quad (5.12)$$

and putting all parts into equation (5.10) yields

$$\frac{1}{T} \frac{dT}{d\tau} = -\frac{v_s^2}{\tau} \quad (5.13)$$

for the time dependence of the temperature. The solution of this equation is given by

$$T(\tau) = T(\tau_0) \left(\frac{\tau_0}{\tau}\right)^{v_s^2}. \quad (5.14)$$

The velocity of sound depends on the exact equation of state. In the context of this model it is usually given by  $v_s^2 \leq \frac{1}{3}$ , which results in a slow decrease of temperature during this phase of one-dimensional expansion.

## 5.2 Probing the QGP

Having established an intuitive view of the medium formation in heavy-ion collisions and a model for the expansion of this medium, the question of how to extract actual information about this medium arises naturally [39]. For probing the internal structure of this medium we need to resolve its substructure, so a probe with wave-length  $\lambda < L$



is needed, which in the case of a hot QGP coincides with  $\lambda < 1/T$ . For this approach a possible probe are hard electromagnetic radiation, consisting of photons or heavy lepton pairs. Since they only interact electromagnetically these will pass the medium relatively unscathed and information about the conditions of the formation can be extracted from them. But especially in the case of photons, there are many additional competing sources of photon production, like particle-antiparticle annihilation or just thermal radiation, since every object is hotter than the vacuum and thus emits radiation, and pion decays. The contributions of each process have to be taken into account. The production rate of heavy quark resonances like  $J/\Psi$  or  $\Upsilon$  can also be used as a probe, comparing the cases with and without medium. Due to screening effects in the medium these resonances can be dissolved, if the temperature is high enough, reducing the rate of production. Lastly the energy loss of jets resulting from strongly interacting partons, called jet quenching, gives information about the medium. The last mechanism will be the main focus now. One additional approach deserves mention. The outermost layers of the plasma are colder than the interior of the plasma, so hadronisation takes place here first. Measuring interferences of identical hadronic particles in ‘‘HBT’’ detector set-ups allows estimates of source sizes. The source size should be dependent on the initial temperature of the medium, since a hotter medium needs to expand more to cool down. The initial temperature is connected to the initial energy density, which in turn is related to the collision energy, meaning that higher collision energies should result in larger source sizes. This generally agrees with estimates from experiments.

Returning now to jet quenching. After the formation of the QGP it is reasonable to assume that any initial quark or gluon of the hard event passes through several fm of QGP, before leaving and hadronising. The basic picture here is the same as an electric charge passing through matter with other (bound) charges. With sufficiently high energy, direct scatterings between the charges take place and result in energy loss due to the radiation of photons. In the familiar energy regime from e.g. experimental exercises, the energy of the photon is on average  $\omega \sim E$ , leading to an energy loss per unit length of

$$-\frac{dE}{dz} \sim E \quad (5.15)$$

assuming successive scatterings of a probabilistic nature. But this breaks down at high energies, where the scatterings cannot be viewed as  $n$  independent scatterings. Destructive interference between the photon emissions arises, which for the case of a

crystal leads to the complete cancellation of all photon emissions except for the first and last photon. This is called the Landau-Pomeranchuk-Migdal (LPM) effect, which actually reduces the radiative energy loss. An adequate effect can be derived for QCD, but since the QGP is not a crystal a total cancellation should not occur. Only a general sketch of the LPM effect will be given here. The basic idea is to look at the time scale  $t_c$  that is needed for the emission of the gluon after a scattering. This can be given as

$$t_c = \frac{E}{2P'k}, \quad (5.16)$$

where  $E$  is the energy,  $P'$  is the momentum of the colour charge after the gluon emission and  $k$  is the gluon momentum. Of interest is the transversal momentum of the gluon, while still requiring  $k_L \gg k_T$  (that the longitudinal momentum is much larger); this leads to

$$t_c \simeq \frac{\omega}{k_T^2}. \quad (5.17)$$

Any scattering taking place during this formation time will interfere destructively, meaning that only one gluon will be emitted. The formation time can be associated with a coherence length  $z_c$ , or with any scattering taking place in this distance interfering destructively. The same proportionality as in equation (5.16) follows. Still, for each scattering the charge will pick up a  $k_T$ -kick proportional to the mean free path length  $\lambda$  of the medium and the screening mass  $\mu$ :

$$k_T^2 \simeq \mu^2 \frac{z_c}{\lambda}. \quad (5.18)$$

With this one can give the formation length in terms of the mean free path and medium mass as

$$z_c \simeq \sqrt{\frac{\lambda}{\mu^2} \omega}. \quad (5.19)$$

The distinction between coherent and incoherent regime can now be given by comparing the two length scales  $z_c$  and  $\lambda$ . For  $\lambda > z_c$  the scatterings are incoherent and can be viewed as  $n$  scatterings leading to

$$-\frac{dE}{dz} \simeq \frac{3\alpha_s E}{\pi \lambda}, \quad (5.20)$$

while for  $\lambda < z_c$  there is coherent scattering with the destructive interference, leading to the LPM bulk expression

$$-\frac{dE}{dz} \simeq \frac{3\alpha_s}{\pi} \sqrt{\frac{\mu^2 E}{\lambda}}. \quad (5.21)$$

The thickness  $L$  of the medium has also be taken into account, since for  $L = z_c$  only one gluon can be emitted in the coherent region. For a fixed energy one can thus give a critical thickness as  $L_c = \sqrt{\frac{E\lambda}{\mu^2}}$ . The bulk LPM behaviour takes place for the case  $L > L_c$ , while for  $L < L_c$  there is still energy loss, since scatterings are taking place, albeit reduced.

## 6 JEWEL

Final state parton showers should evolve for several fm/c, which is comparable to the extension of the QGP in heavy-ion collisions. The fundamental idea of parton shower evolution in a vacuum has been talked about in chapter 3. In the presence of a QGP this evolution has to be modified to reproduce jet quenching behaviour. One possible model of this modification is given in the MC event generator JEWEL (Jet Evolution With Energy Loss), which is used for the calculations in the next chapter. Here interactions of the partons with constituents of the medium are treated as standard  $2 \rightarrow 2$  QCD processes, like the initial hard interaction. Coupling this with the parton shower leads to a framework where energy loss due to scattering and radiation, i.e. bremsstrahlung, takes place naturally and in a probabilistic fashion. A non-Abelian version of the LPM effect is also included in JEWEL. Details of the implementation will be discussed briefly in the following. For further details and references see the corresponding JEWEL publications [50] [51] [52] [53] [54] and [55].

### 6.1 Process Generation

The event generation with JEWEL takes place in three steps:

1. A hard matrix-element is generated by PYTHIA 6.4 according to the specified phase space cuts. PYTHIA also generates the virtuality-ordered initial-state radiation. Multi-parton interactions and the calculation of the underlying event are turned off.
2. JEWEL takes the outgoing hard partons and chooses an impact parameter. Afterwards the final state parton shower is generated

3. The final state is handed back to PYTHIA for hadronisation and written in the event record.

There is an option to run JEWEL without a medium. In this case the three steps are also followed, but the parton shower reduces to the virtuality-ordered parton shower in the vacuum. This is useful to generate pp-baselines for the process of interest.

## 6.2 Medium Modifications

While there are some theoretical insights about jet evolution in a dense and strongly interacting hot plasma these are mostly restrained to some limiting case, like the high energy eikonal limit for example. In general the kinematic constraints for these insights to be valid cannot be assumed to hold for the full evolution of a jet in the plasma. Therefore some assumptions are needed to construct a framework for full jet evolution. The base assumptions of JEWEL are:

1. The jet can resolve individual partons of the medium, so the medium can be viewed as a collection of partons with a distribution in phase space. Factorisation holds for all scatterings of a jet with a parton of the medium.
2. Many scatterings between jet and medium will be soft. A continuation of the QCD matrix elements into the infra-red region can describe the dominating effect of these soft scatterings.
3. Emissions can be attributed a formation time. JEWEL will discriminate between competing sources of radiation based on the associated emission times.
4. The basic physical picture of the LPM effect, which is formally derived in the eikonal limit, also holds in the non-eikonal region.

As mentioned before, in the case that no medium is generated JEWEL is just a normal parton shower. In the medium, scatterings can take place and these secondary scatterings are treated like the initial hard scattering. What happens when a parton associated with a parton shower that is not finalised scatters in the medium is governed

by formation times. The formation is dependent on the emitting parton's energy  $E$  and virtuality  $Q$ :

$$\tau = \frac{E}{Q^2}. \quad (6.1)$$

If a parton is due to split at a scale  $Q_1$  on a timescale  $\tau_1$  and simultaneously or shortly before that a scattering at scale  $t_2^s$  takes place, then JEWEL initiates a hypothetical parton shower with starting scale  $t_2^s$ . If this hypothetical shower does not produce radiation it is discarded and the splitting at  $t_1$  takes place. If the hypothetical shower produces radiation at a scale  $t_2$  with the corresponding time scale  $t_2$  a comparison between the scales  $t_1$  and  $t_2$  takes place. The splitting associated with the shorter formation is chosen, while the other one is discarded and the parton shower evolution continues normally until the next rescattering happens. Also the exact kinematic of every splitting in the medium is directly calculated, which for the vacuum case complicates the calculation, but is necessary to avoid difficulties related to the treatment of possible rescatterings.

Though to treat the rescattering in the medium like the  $2 \rightarrow 2$  hard process with parton showers some notion of PDF is required to correctly treat initial-state radiation. But the partons of the medium were not constituents of an incoming nucleus before the scattering; the same holds for the parton of the shower evolution. Therefore JEWEL invokes the notion of "partonic PDFs", which give a density of partons inside of partons. These are constructed in a way that a cut-off scale  $Q_c$  is introduced. No radiation is possible for processes at or below this scale. Above the scale  $Q_c$  radiation can be generated, so one can think of this as sort of an resolution scale. The partonic PDFs are computed with the DGLAP equation obeying the boundary condition

$$f_i^j(x, Q_c^2) = \begin{cases} \delta(1-x) & \text{if } i = j \\ 0 & \text{if } i \neq j \end{cases}. \quad (6.2)$$

So elastic processes, inelastic processes with many particle final states and scatterings with bremsstrahlung can be generated by the same process.

Since many interactions in the medium will be soft, an infra-red regulator is introduced to the matrix element. The cross section for  $2 \rightarrow 2$  processes is given as

$$\sigma_i(E, T) = \int_0^{\hat{Q}_{\max}^2(E, T)} d\hat{Q}^2 \int_{x_{\min}(\hat{Q}^2)}^{x_{\max}(\hat{Q}^2)} dx \sum_{j \in q, \bar{q}, g} f_j^i(x, \hat{Q}^2) \frac{d\hat{\sigma}_j}{d\hat{Q}^2}. \quad (6.3)$$

The maximum momentum transfer  $\hat{Q}_{\max}^2 = 2m_s(T)[E_p - m_p]$  is determined by the initial kinematics, where  $m_s(T)$  is the temperature-dependent mass of the medium parton and  $E_p$  and  $m_p$  are the energy and the (virtual) mass of the projectile parton. The boundaries on  $x$  are given by  $x_{\min}(\hat{Q}^2) = \frac{Q_c}{4\hat{Q}^2}$  and  $x_{\max}(\hat{Q}^2) = 1 - \frac{Q_c}{4\hat{Q}^2}$ . The partonic cross sections are regularised by a Debye mass  $\mu_D \approx 3T$ :

$$\frac{d\hat{\sigma}}{d\hat{Q}^2} = C_R \frac{\pi}{\hat{s}^2} \alpha_s^2 (\hat{Q}^2 + \mu_D^2) \frac{\hat{s}^2 + (\hat{s} - \hat{Q}^2)^2}{(\hat{Q}^2 + \mu_D^2)^2} \rightarrow C_R 2\pi \alpha_s^2 (\hat{Q}^2 + \mu_D^2) \frac{1}{(\hat{Q}^2 + \mu_D^2)^2}, \quad (6.4)$$

where  $C_R = \frac{4}{9}$  for quark-quark,  $C_R = 1$  for quark-gluon and  $C_R = \frac{9}{4}$  for gluon-gluon scattering.

Now only the implementation of the LPM in JEWEL is left. This is done in a probabilistic fashion, meaning that, like with any other emission, the gluon emission is associated with a formation time  $\tau = \frac{k_T^2}{2\omega}$ , where  $\omega$  is the energy of the gluon. Additional scatterings taking place during this time act coherently, meaning their momentum transfers  $q_{\perp}$  are added in a vector sum to give the total momentum transfer  $Q_{\perp} = \sum_i q_{\perp,i}$ . After every scattering  $Q_{\perp}$  and  $k_T$  are calculated and the formation time is updated accordingly. When the last scattering is still within this update time, counted from the first scattering, it is included, otherwise rejected. When there are no further coherent scatterings the emission of the gluon is accepted with a probability of  $\frac{1}{N_{\text{scat}}}$ , where  $N_{\text{scat}}$  is the number of coherent scatterings. There is one complication in the non-eikonal limit, namely the formation there is not related to the scale  $t^s$  of the momentum transfer but to the scale of the emission, which can be between that and the cut-off scale  $t_c$ . Now considering the scale  $t_1^s$  before the last scattering, the scale  $t_2^s$  after the last scattering, including the momentum transfer, may now be larger or smaller than before the scattering, since the momentum transfer is added vectorially. Since the scale before the scattering might be a scale in a parton shower one has to correct the phase space, emission probability and account for possible existing radiation at a scale  $t_1$  when updating this scale. The different cases are

- $t_2^s < t_c$ : No radiation is possible, existing radiation is rejected.
- existing radiation,  $t_2^s > t_1^s$ : The emission scale might have to be redetermined. The old scale is kept with a probability given by the Sudakov form factor  $\Delta(t_2^s, t_1^s)$ . Otherwise the new scale  $t_2$  from this interval is chosen.

- existing radiation,  $t_1^s > t_2^s > t_c$ : The existing emission is rejected with a probability of  $(1 - \Delta(t_1^s, t_c))/(1 - \Delta(t_2^s, t_c))$ . If it is not rejected but the scale  $t_1$  is larger than  $t_2^s$ , a new scale from the interval has to be chosen.
- no existing radiation,  $t_2^s > t_1^s$ : A new emission with probability  $1 - \Delta(t_2^s, t_1^s)$  is chosen at a scale  $t_2$  between the scales before and after the scattering.
- no existing radiation,  $t_1^s > t_2^s > t_c$ : Nothing happens in this case, because the probability of emission is smaller and nothing has to be reweighted.

JEWEL uses a Bjorken model for the evolution of the medium. The the initial energy density  $\epsilon_i$  is related to the initial temperature  $T_i$  at the proper formation time  $\tau_i$  by  $\epsilon_i \propto T_i^4$ . Depending on the centrality of the collision this is further modified by

$$\epsilon(x, y, b, \tau_i) = \epsilon_i \frac{n_{\text{part}}(x, y, b)}{\langle n_{\text{part}} \rangle} (b = 0) \quad \text{with} \quad \langle n_{\text{part}} \rangle (b = 0) \approx \frac{2A}{\pi R_A}, \quad (6.5)$$

where  $n_{\text{part}}$  is the density of participating nucleons in the transversal plane and  $b$  the impact parameter. This leads to a decrease of initial temperature or energy density with centrality. Also symmetric  $A + A$ -nuclei collisions are assumed. The default critical temperature is given by  $T_c = 170$  MeV; scatterings stop when the temperature drops below this value.

### 6.3 Background subtraction

In experiments there is a large background activity in heavy-ion collisions. Estimates of these backgrounds are calculated and afterwards they are subtracted from the measured jets, to obtain the spectrum of the "true" jets. While JEWEL does not simulate the underlying events, the way it handles the recoil partners of the hard partons in the medium requires a subtraction procedure to correct jets as well. For more details on this see [33]. If a recoil happens, the parton from the medium is, without further interaction in the medium, taken into the colour string and included in the hadronisation process. The momentum of this parton then has two components, its original thermal momentum and the momentum transferred in the scattering. Only the latter component contains information about medium responses and the thermal component has to be subtracted from the jets. In the calculations the subtraction method 4Mom-



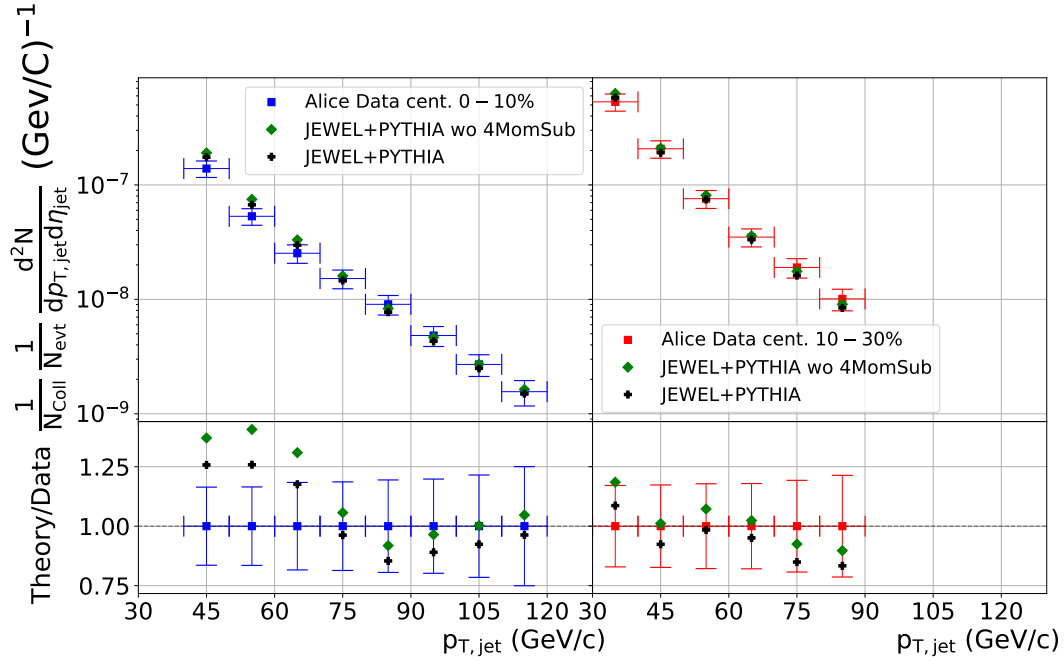


Figure 6.1: Comparison of the jet yield scaled by  $N_{\text{coll}} = 1501$  (left) and 743 (right) calculated with and without the 4MomSub algorithm, at  $\sqrt{s_{NN}} = 2.76$  TeV and a jet-rapidity of  $|\eta| < 0.5$  for the centrality bins 0 – 10% (left) and 10 – 30% (right). The anti- $k_T$  algorithm with  $R = 0.2$  was used. The data points are taken from [8].

Sub from the referenced paper was used, which exactly removes all thermal momenta. To do this two things have to be done. First, all thermal momenta of recoil partners have to be stored in the event record and second, a large set of "ghosts" has to be introduced. As mentioned before, these ghosts do not change the jet's momentum or structure, since they are IRC safe. But they make the matching of a thermal momentum with its corresponding jet in the rapidity-azimuthal angle plane easier, since they inflate the number of particles belonging to each jet and thus make the area of the jet more concise.

The 4MomSub algorithm proceeds as follows:

1. Cluster all particles into jets.
2. Find all thermal momenta in the final state (HepMC status code 3).
3. For each jet find all the thermal momenta within a distance  $\Delta R < 10^{-5}$  of a jet constituent.
4. Sum up all the thermal momenta for each given jet.

5. Subtract the sum of thermal momenta from the jet's four momentum to obtain the corrected jets.
6. Jet observables can now be calculated with the corrected four-momenta.

A comparison between the jet yield in PbPb-collision with and without the use of the algorithm can be seen in Figure 6.1.

## 7 Experimental data of jet production in lead-lead collisions from the LHC

This chapter provides a brief overview of published papers about lead-lead collisions (PbPb) and measurements of jet properties from the main experiments at the LHC. For completeness' sake we first gather some definitions of variables used in the table<sup>1</sup> and clarify some notations.

Generally the transverse momentum will be called  $p_T$ . A number in the  $p_T$ -column that is written like 120(50) signifies cuts on dijet systems. The first number is the requirement on the leading jet's transverse momentum called  $p_{T1}$ , the second on the subleading jet's called  $p_{T2}$ . The jet mass is called  $m$ . The rapidity is denoted by  $y$ , the pseudorapidity by  $\eta$  and  $\varphi$  is the azimuthal angle. Now for some observables, starting with the dijet momentum balance  $A_j$ . It is calculated as:

$$A_j = \frac{p_{T1} - p_{T2}}{p_{T1} + p_{T2}}. \quad (7.1)$$

The nuclear modification factor  $R_{AA}$  is defined as the jet yield  $N$  in PbPb-collisions divided by the differential cross section in pp-collisions scaled by  $T_{AA}$  :

$$R_{AA} = \frac{\frac{1}{N_{evt}} \frac{d^2N}{dp_T dy}}{\langle T_{AA} \rangle \frac{d^2\sigma}{dp_T dy}}. \quad (7.2)$$

---

<sup>1</sup>One should check the exact definition used in the specific paper of interest. Also one should in any case check the exact cuts and if further selection criteria are applied, like e.g. particle tracks with a minimum  $p_T$  in a jet.

Angularity or girth  $g$  is defined as the the sum over the  $p_{T,i}$  of all jet constituents divided by the jet  $p_T$  times the distance  $\Delta R_{\text{jet},i}$  in the  $(\eta, \varphi)$  plane of the constituent and the jet axis:

$$g = \sum_{i \in \text{jet}} \frac{p_{T,i}}{p_{T,\text{jet}}} \Delta R_{\text{jet},i}. \quad (7.3)$$

Another jet shape observable is the momentum dispersion  $p_T D$ :

$$p_T D = \frac{\sqrt{\sum_{i \in \text{jet}} p_{T,i}^2}}{\sum_{i \in \text{jet}} p_{T,i}}. \quad (7.4)$$

This list obviously does not claim completeness, things like multi-particle correlations and similar analysis have been left out. One can always check arXiv for newer analysis as well. Here comes the list:

arXiv	Coll.	$\sqrt{s}$ [TeV]	Observable	$p_T$ [GeV]	$ y $	Jet alg.	R
1809.07280	ATLAS	5.02	Jet to photon $p_T$ ratio [3]	$> 31.6$	2.8	Anti- $k_T$	0.4
1807.06854	ALICE	2.76	Jet shapes, angularity, momentum dispersion [7]	40 – 60	0.7	anti- $k_T$	0.2
1805.05635	ATLAS	5.02	$R_{AA}$ , $R_{AA}$ ratios for different y-bins [4]	50 – 1000	2.8	Anti- $k_T$	0.4
1805.05424	ATLAS	5.02	Fragmentation functions, $R_D$ [2]	126 – 398	2.1	Anti- $k_T$	0.4
1805.05145	CMS	5.02	Groomed jet mass [44]	$> 140$	1.4	Anti- $k_T$	0.4
1803.00042	CMS	5.02	jet shapes $\rho(\Delta r)$ [43]	$> 120$	1.6	Anti- $k_T$	0.4
1802.00707	CMS	5.02	b tagged jets, $p_{T2}/p_{T1}$ and $\Delta\varphi$ [42]	$> 100(40)$	1.5	Anti- $k_T$	0.4

arXiv	Coll.	$\sqrt{s}$ [TeV]	Observable	$p_T$ [GeV]	$ y $	Jet alg.	R
1711.09738	CMS	5.02	$\varphi$ and $p_T$ correlations of photons and jets [45]	$> 30$	1.6	Anti- $k_T$	0.3
1706.09363	ATLAS	2.76	Dijet momentum fraction $x_j$ [1]	$> 25$	2.1	Anti- $k_T$	0.3 0.4
1702.01060	CMS	5.02	Z-jet $p_T$ -fraction, $R_{jZ}$ average number of jet partners [41]	30	1.6	Anti- $k_T$	0.3
1702.00804	ALICE	2.76	$\frac{d\sigma^{PbPb}}{dM} / \frac{d\sigma^{pPb}}{dM}$ , $\langle M \rangle$ [6]	60 – 120	0.4	anti- $k_T$	0.4
1611.01664	CMS	5.02	$R_{AA}$ in PbPb and pPb [30]	1 – 400	1	Anti- $k_T$	0.4
1609.06667	ALICE	2.76	Peak shapes in $\Delta\varphi$ and $\Delta\eta$ (Two particle correlations) [11]	1 – 8			
1609.06643	ALICE	2.76	Similar to above [10]				
1609.05383	CMS	2.76	$R_{AA}$ [31]	70 – 300	2	Anti- $k_T$	0.2 0.3 0.4
1609.02466	CMS	2.76	Jet shape $\rho(\Delta r)$ , az. distribution of ch.particle $p_T$ , $A_j$ [28]	$> 120(50)$	2	Anti- $k_T$	0.3

arXiv	Coll.	$\sqrt{s}$ [TeV]	Observable	$p_T$ [GeV]	$ y $	Jet alg.	R
1601.00079	CMS	2.76	Jet-track angular correlations, symmetrized $\Delta\eta$ and $\Delta\varphi$ for ch.tracks [27]	$> 120(50)$	2	Anti- $k_T$	0.3
1509.09029	CMS	2.76	$p_T$ balance against opening angle and jet radius, dijet asymmetry [29]	$> 120(50)$	2	Anti- $k_T$	0.2 0.3 0.4 0.5
1502.01689	ALICE	2.76	$R_{AA}$ [8]	40 – 120	0.5	Anti- $k_T$	0.2
1205.5872	CMS	2.76	Fragmentation function, $z = p_{\parallel}^{track}/p_{jet}$ , (sub)leading $p_T$ distributions [20]	$> 100(40)$	2	Anti- $k_T$	0.3
1202.5022	CMS	2.76	$\Delta\varphi$ , $A_j$ , $p_{T2}/p_{T1}$ [19]	$> 120(30)$	2	Anti- $k_T$	0.3
1102.1957	CMS	2.76	$\Delta\varphi$ , Subleading vs. leading $p_T$ , leading jet- $p_T$ , $A_j$ , $(p_{T1}-p_{T2})/p_{T1}$ [18]	$> 120(50)$	2	Anti- $k_T$	0.5

Table 7.1: Papers on arXiv for jet-measurements in lead-lead collisions at the LHC.

## 8 Results

At last, it is now time to compare results obtained by JEWEL with experimental measurements. For this thesis, the jet observable of interest is the nuclear modification factor  $R_{AA}$ ; it is defined as

$$R_{AA} = \frac{\frac{1}{N_{\text{Evt}}} \left. \frac{d^2 N_{\text{jets}}^{AA}}{dp_T d\eta} \right|_{\text{cent}}}{\langle T_{AA} \rangle \left. \frac{d^2 \sigma_{\text{jets}}}{dp_T d\eta} \right|_{\text{pp}}}, \quad (8.1)$$

where  $N_{\text{jets}}^{AA}$  is the jet yield in Pb+Pb collisions for a given centrality range, binned in the transverse momentum  $p_T$  and rapidity  $\eta$ .  $N_{\text{Evt}}$  is the number of Pb+Pb collisions; some more comments on this normalisation will be given below. The jet yield is then scaled by the nuclear thickness function  $T_{AA}$  and divided by the jet cross section  $\sigma_{\text{jets}}$  in pp collisions. As discussed in chapter 3, the difference between pp and Pb+Pb can, in geometric terms, be accounted for by the Glauber model.  $T_{AA}$  thus sufficiently normalises the yield in Pb+Pb collisions; without a medium the ratio should therefore be equal to one; deviations arise due to jet quenching effects in a medium. Partons going through the QGP lose energy, so the jet yield should be reduced for a given  $p_T$ -range. How much the yield is suppressed depends on the nature and density of the medium.

JEWEL is compared to the results of three papers, one from the ALICE collaboration [8], one from CMS [31] and one from ATLAS [4]. These papers differ in the  $p_T$ -range of the jets, the rapidities, the jet radius and also the center-of-mass (CMS) energy, so theoretical predictions can be compared to experiments over a range of parameters. Before results are presented, there are a few things that need to be talked about: event generation, the normalisation of the Pb+Pb calculations and also some modifications to JEWEL, which were made in the context of this thesis.

Starting with process generation. A user can choose various parameters for the run: the

number of events  $N_{\text{sim}}$  to be generated,  $\eta$  and also a minimum transverse momentum  $p_{\text{min}}$  and a maximum transverse momentum  $p_{\text{max}}$ , which have to be smaller/larger than the  $p_{\text{T}}$ -range of the measurement. The rapidity should be chosen large enough to cover the range of the experiment and  $N_{\text{sim}}$  should be sufficiently large to ensure a small statistical error. The events will then be generated according to the chosen parameters, where a  $p_{\text{T}}$  in the specified range is drawn from a distribution given by the cross section. Since the cross section decreases massively over several orders of magnitude for typical  $p_{\text{T}}$ -ranges measured in experiments, most events generated would have small  $p_{\text{T}}$ , so getting sufficient statistics in high- $p_{\text{T}}$  bins is very costly, considering computation time. There are two ways to circumvent this [46]: the first is to cut the whole  $p_{\text{T}}$ -range into  $n$  intervals with interval edges  $p_i$ ,  $i = 0, \dots, n$ , where  $p_0 = p_{\text{min}}$  and  $p_n = p_{\text{max}}$ . Starting runs in each interval makes sure that there is sufficient statistics of high- $p_{\text{T}}$  events; also each of these runs can be viewed as independent, since they probe different areas of phase space. This in turn implies that each run has to be normalised independently and the results from different intervals can be summed to obtain the theoretical prediction. Results are usually given as histograms, for the above-mentioned papers binned in  $p_{\text{T}}$ . For this the number of events that survive the  $p_{\text{T}}/\eta$ -cuts or other requirements specific to the analyses are counted in the corresponding bin of the histogram. The normalisation then happens as follows: take for example the doubly differential cross section  $\frac{d^2\sigma}{dp_{\text{T}} d\eta}$  and let  $i$  denote a  $p_{\text{T}}$ -bin of the histogram. The end result is given by summing over the contribution of each of the  $n$  intervals for this bin:

$$\frac{d^2\sigma}{dp_{\text{T}} d\eta}[i] = \sum_{j=1}^n \frac{\sigma_j}{N_j} \frac{N_{\text{acc},j}[i]}{\Delta p_{\text{T}} \Delta \eta}, \quad (8.2)$$

where  $\sigma_j$  is the cross section of the given interval, usually given by the event generator.  $N_j$  is the number of events generated in the interval. This is then multiplied by the number of events in the bin that got through the analysis  $N_{\text{acc},j}$  and divided by the width of the transverse momentum  $\Delta p_{\text{T}}$  and the rapidity range  $\Delta \eta$ .

The other possibility is to work with weighted events. This means that one takes the whole  $p_{\text{T}}$ -range for event generation, but oversamples the high- $p_{\text{T}}$  region, so events are generated according to a flat distribution in  $p_{\text{T}}$ . To still retain the original decrease in the cross section, generated events are associated with a event weight  $\omega_i$ , which decrease for high  $p_{\text{T}}$ . For the normalisation one gathers all the event weights in a bin and divides by the sum of all event weights. When combining different runs it has to be



ensured that all the event weights are added in such a way that the result corresponds to a single large run. By contrast, the way to generate events mentioned first is also referred to as working with unweighted events; there, each event carries the weight 1.

The normalisation of the jet yields in Pb+Pb collisions requires some attention as well. JEWEL calculates hard events and supplements these with a parton shower evolution, but the normalisation of the yield is the number of nucleus-nucleus collisions. So a way to relate hard events in a given  $p_T$ -range to the number of Pb+Pb collisions is needed. Working with weighted events, a significant dependence of the normalisation on  $p_{\min}$  can be observed when one naively sets  $N_{\text{Evt}} = N_{\text{sim}}$ . A correct normalisation of the generated events should be independent of  $p_{\min}$ , if it is chosen sufficiently small. The normalisation used here for the Pb+Pb events is constructed with the Glauber model. Let  $\sigma_{\text{hard}}$  be the cross section of the hard process, which is given by the event generator. Going with the Glauber model this can be viewed as the cross section for a hard nucleon-nucleon collision. One can also give a total cross section for inelastic nucleon-nucleon collisions  $\sigma_{\text{inel}}^{\text{NN}}$  from experiments. Not all contributions to the total cross section can be given perturbatively, so it cannot be calculated. The number of hard events  $N_{\text{hard}}$  divided by  $N_{\text{Evt}}$  for nucleon-nucleon interactions is then given by the ratio of  $\sigma_{\text{hard}}$  over  $\sigma_{\text{inel}}^{\text{NN}}$ . In a single nucleus-nucleus collision an average of  $\langle N_{\text{coll}} \rangle$  of these collisions happen in a given centrality. Taking everything together leads to

$$\frac{N_{\text{hard}}}{N_{\text{Evt}}} = \langle N_{\text{coll}} \rangle \frac{\sigma_{\text{hard}}}{\sigma_{\text{inel}}^{\text{NN}}}. \quad (8.3)$$

So the normalisation of the generated hard events is obtained by

$$N_{\text{Evt}} = \frac{N_{\text{hard}}}{\langle N_{\text{coll}} \rangle} \frac{\sigma_{\text{inel}}^{\text{NN}}}{\sigma_{\text{hard}}}, \quad (8.4)$$

where  $N_{\text{hard}}$  can be set equal to the number of generated events. Taking the parametrisation from PYTHIA-8.2 [48] one obtains  $\sigma_{\text{inel}}^{\text{NN}} = 62.0403 \text{ mb}$  for  $\sqrt{s_{\text{NN}}} = 2.76 \text{ TeV}$  and  $\sigma_{\text{inel}}^{\text{NN}} = 67.8932 \text{ mb}$  for  $\sqrt{s_{\text{NN}}} = 5.02 \text{ TeV}$ .

JEWEL is based upon PYTHIA-6.4, which uses LHAPDF5 [49] for PDF's. In JEWEL one chooses a proton PDF, which then gets modified by the EPS09 [25] nuclear factor to construct a bound proton PDF of the given nucleus. There are newer nPDF sets available, but they are only part of LHAPDF6 [16]. Here one can use an interface called LHAGLUE for legacy code built around LHAPDF5. This interface gives the

illusion of using LHAPDF5, while actually working with LHAPDF6, so that one can use the newer PDF sets. For the calculation of  $R_{AA}$  the nCTEQ15-full\_nuclear [32] set for lead together with the free proton PDF from nCTEQ15 is used. The full nuclear PDF is constructed as the PDF of an average parton in the nucleus, so using it as the "proton" PDF in JEWEL and turning off the modification factor from EPS09 gives the right initial state for hard Pb+Pb collisions. Due to the construction of bound PDF's with the EPS09 factor, JEWEL has to differentiate between the PDF's of protons and neutrons. Neutron PDF's are constructed via isospin-symmetry. So there are process sub-channels for proton-proton, proton-neutron and neutron-neutron collisions, into which the total number of events is distributed. Since the used nPDF now describes an average parton, it is sufficient to only consider the pp-channel. For consistency with the nCTEQ15 parametrisation the number of flavours to evaluate  $\alpha_s$  is taken to be 5 and the Landau pole is set to 0.226 GeV. The PDF errors are calculated with the 32 error PDF's. This is then also compared to, at least, the central value of the EPPS16 nPDF [24]. For the EPPS16 to work with JEWEL there are some minor adjustments to be made. JEWEL uses the Landau pole and a number of flavours to calculate  $\alpha_s$ , but EPPS16 is parametrized by the mass of the Z-boson and the value of  $\alpha_s$  at that scale. With the help of RunDec [21] one easily obtains the values necessary for JEWEL as  $\Lambda_{QCD} = 0.208364$  GeV for five flavours evaluation of  $\alpha_s$ . Each PDF set in LHAPDF comes with an info file, where general information about scales and number of set members are given, that are read out before the PDF's are used. An entry AlphaS\_Lambda5 equal to the value given above has to be added to the EPPS16 info file. Also there is a flag titled Particle that needs to be modified. There the number 1000822080 is given, which is the PDG ID code for lead, but in the initial state of JEWEL there is a proton, so this needs to be changed to 2212, which stands for proton. The EPPS16 grids for lead available on the LHAPDF website are also constructed as the PDF's of an average parton inside the nucleus, as stated by their website<sup>1</sup>, so following the logic from above this should then also give hard events in Pb+Pb collisions with JEWEL.

One further modification is introduced to JEWEL; additional parameters to vary the renormalisation and factorisation scale in the initial hard process. PYTHIA-6 [46] contains several switches for exactly this purpose. The parameter mstp(33) has to be set to 3, then one has the parameter parp(33) for variations of the renormalisation scale

<sup>1</sup><http://r.jyu.fi/ufd>, accessed 07.05.2019.

$\mu_R$  of the hard process. The factorisation scale for the evaluation of the PDF can be varied with `parp(34)`. The scales come in as a factor in the calculation of  $\alpha_s$ . It is easy to then introduce additional flags for the parameter file in the main program to be read in and expand the initialisation routine for PYTHIA with parameters mentioned above, set to the read-in value. For the estimation of scale uncertainties the so-called seven-point method is used, which means that every calculation is repeated six additional times. In this method both scales are varied in certain steps; the exact values for the factors are given in the following table:

	$\mu_R$	$\mu_F$
1.	0.25	0.25
2.	1	0.25
3.	0.25	1
4.	1	1
5.	4	1
6.	1	4
7.	4	4

The per-event analysis has been done with Rivet [15], where the anti- $k_T$  algorithm is used as the jet definition. All the following plots were created with the Python code `matplotlib` [22]. The data points of the experimental measurement were taken from the corresponding entry in the HEPdata archive [34] for the three papers.

## 8.1 ALICE

First comes the ALICE paper [8]. There the  $p_T$ -spectrum of jets and the nuclear modification factor were measured at  $\sqrt{s_{NN}} = 2.76$  TeV in the rapidity range  $|\eta| < 0.5$ . The anti- $k_T$  algorithm with  $R = 0.2$  was used to reconstruct the jets. Two centrality ranges for Pb+Pb collisions are given, with a  $p_{T,\text{jet}}$ -range of  $40 < p_{T,\text{jet}} < 120$  GeV/c in 0 – 10% and  $30 < p_{T,\text{jet}} < 100$  GeV/c in 10 – 30% collisions. Additionally each jet needs to contain one particle track with  $p_T > 5$  GeV/c. This is done to decrease the number of jets that are constructed purely from background activity in the experiment. For more details on the exact experimental set-up and data unfolding see the referenced paper. Before looking at the nuclear modification factor it is instrumental to look at its two

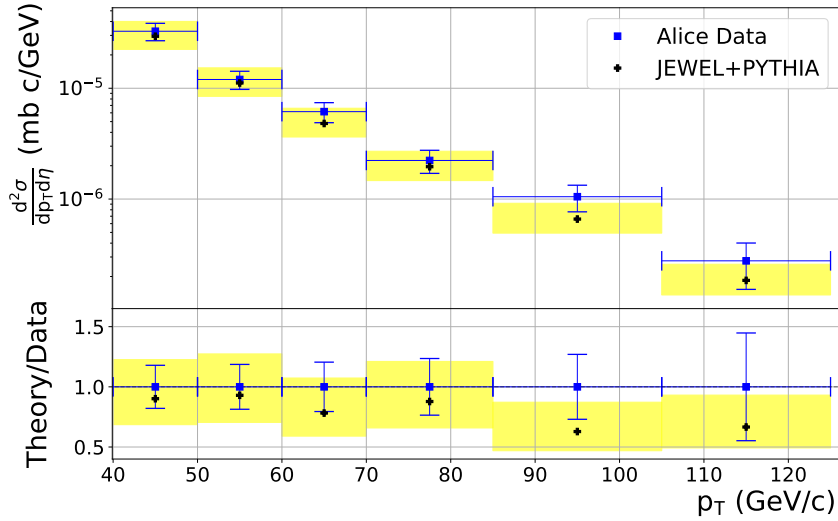


Figure 8.1: Comparison between the differential jet cross section for pp collisions at  $\sqrt{s} = 2.76$  TeV for jet radius  $R = 0.2$  and  $|\eta| < 0.5$  obtained by ALICE and JEWEL. The yellow shaded bands give the scale uncertainties. Data points taken from [5].

parts, the differential cross section for pp-collisions and the jet yield in Pb+Pb collisions separately at first, in order to quantify possible sources of deviation in  $R_{AA}$ . Starting with the differential cross section in pp-collisions. A comparison between measurement and the prediction of JEWEL can be seen in Figure 8.1. The yellow bands correspond to the scale uncertainties obtained with the seven point scale variation; a ratio of the theoretical prediction over the experimental data can be seen in the bottom panel, where basically everything is just divided by the reported experimental value. Statistical errors from the MC simulations are not included in all of the following figures. The data points for this figure were actually taken from [5], which uses the same cuts as the above-mentioned analysis, but without the track requirement, since the original paper above does not give the differential cross section. A good agreement between JEWEL and experiment can be reported. Taking into account the missing track requirement on the data points from ALICE, the JEWEL results should actually be slightly better. Only slightly, because no significant impact of this requirement on jets was reported in [8]. The scale uncertainties are fairly large, as is to be expected for a leading-order calculation.

Next is the jet yield in Pb+Pb collisions. The result can be seen in Figure 8.2, where the green shaded bands correspond to the uncertainty of nCTEQ15, estimated with the

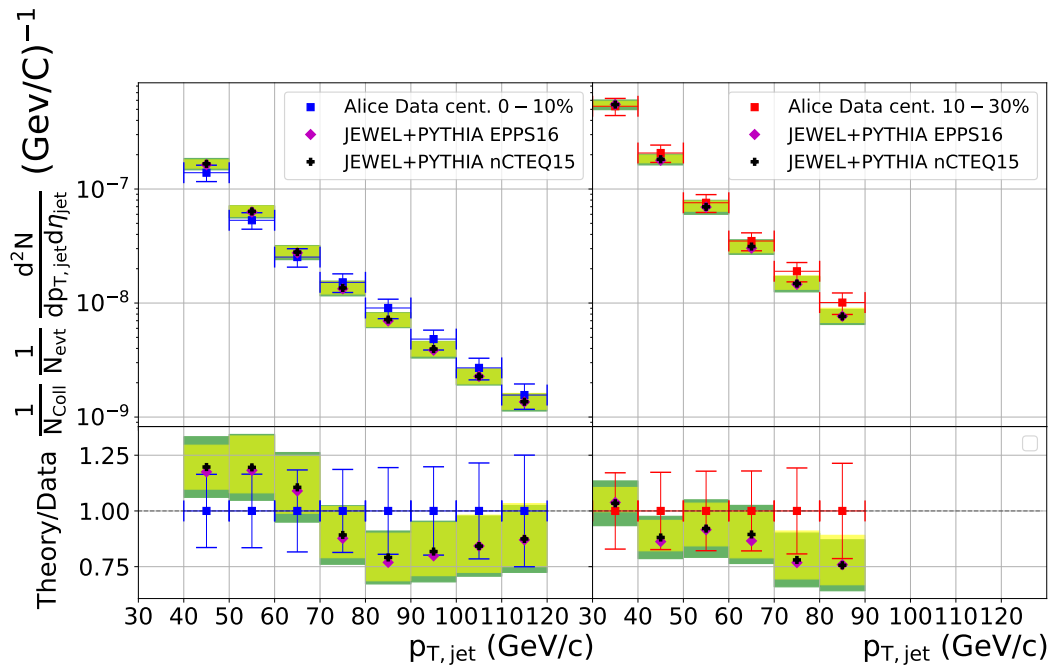


Figure 8.2: Comparison between the differential jet yield in Pb+Pb collisions at  $\sqrt{s} = 2.76$  TeV for jet radius  $R = 0.2$  and  $|\eta| < 0.5$  obtained by ALICE and JEWEL in the centrality ranges 0 – 10% (left) and 10 – 30% (right). The yellow shaded bands give the scale uncertainties and the green shaded bands correspond to PDF uncertainties. Data points taken from [8].

error PDF sets. The yellow shaded band corresponds to the scale uncertainty, again. For comparison the central PDF of EPPS16 is also included. The jet yields are given for the centrality ranges 0 – 10% on the left and 10 – 30% on the right. Here again a very good agreement between JEWEL and the experimental values is seen, where the result for the most central collision seems to fare slightly better. The central values of both PDF sets also seem to agree very well, with some minor deviations. Uncertainties due to the scale and the nCTEQ-PDF are approximately of the same size. These calculations were not done for the EPPS16 set, since the JEWEL calculation in the presence of a medium are very time-intensive. As a rule of thumb, turning the medium off for calculations reduces the time required for generating the same number of events by a factor of 25.

Combining the two previous results then gives the nuclear modification factor  $R_{AA}$ , as defined in Equation (8.1). This can be seen in Figure 8.3, where the results agree well with experimental data. This comes as no surprise, since the two previous results are in good agreement with the data. The general trend of a slight increase in  $R_{AA}$  with  $p_T$  can be replicated by JEWEL. JEWEL seems to overestimate  $R_{AA}$  in the low- $p_T$

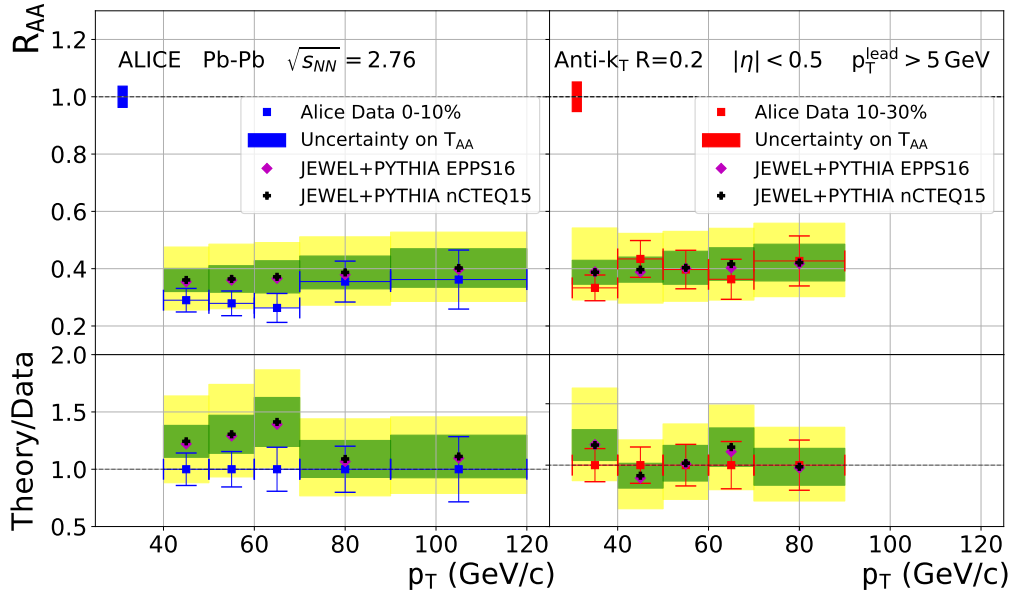


Figure 8.3: Comparison between the nuclear modification factor  $R_{AA}$  at  $\sqrt{s} = 2.76$  TeV for jet radius  $R = 0.2$  and  $|\eta| < 0.5$  obtained by ALICE and JEWEL in the centrality ranges 0 – 10% (left) and 10 – 30% (right). The yellow shaded bands give the scale uncertainties and the green shaded bands correspond to PDF uncertainties. Data points taken from [8].

region for  $-10\%$  centrality though, but the results agree within their margin of error. The scale uncertainty is dominant now.  $R_{AA}$  was calculated for each of the seven scale combinations separately. The plotted points correspond to  $\mu_R = \mu_F = 1$  and the band was generated by searching for the maximum and minimum in the remaining six combinations. Proceeding like this can be viewed as a rather conservative estimate of the scale uncertainty for a combined observable like  $R_{AA}$ , but like mentioned before, it is now considerably larger than the PDF uncertainty.

The critical temperature in JEWEL is by default given as  $T_C = 170$  MeV, also an initial temperature of  $T_I = 360$  MeV is given. Newer values for these temperatures deviate from this, because at the time of writing JEWEL is already a few years old. So as a last step the effect of varying the initial and critical temperature on the jet yield in Pb+Pb collisions is quantified. The critical temperature is given by latest lattice calculations as  $T_C = (156.5 \pm 1.5)$  MeV [12]. Giving a value for the initial temperature is more difficult, see for example [9]. Depending on the initial time of the evolution and the model calculation estimates range from 300 to 700 MeV. Additionally a decrease of  $T_I$  with centrality can be observed. Starting with the critical temperature.

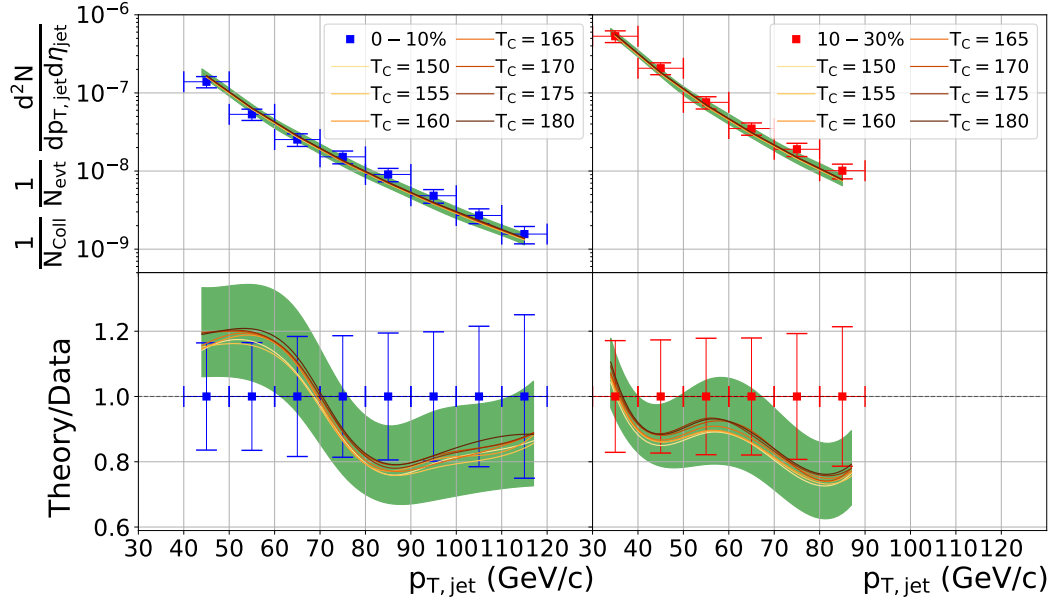


Figure 8.4: Dependence of the jet yield on the critical temperature  $T_C$  of the QGP. The default value in JEWEL for  $T_C$  is 170 MeV. The PDF uncertainties correspond to the green shaded band.

The effect of increasing it from 150 MeV to 180 MeV in steps of 5 MeV can be seen in Figure 8.4. There a spline interpolation for the points from JEWEL and the PDF uncertainty was used for better visibility. Since the scale uncertainties are roughly equal to the PDF uncertainty they are not shown here. The dependence is what one would expect. A higher  $T_C$  corresponds to shorter duration for the medium evolution, which in turn implies fewer opportunities for partons from the hard event to interact with the medium. So jets should be less suppressed for higher  $T_C$ , which is seen in the plot. The dependence on  $T_C$  is rather small for the jet yield though and well within uncertainties from the PDF. So no real conclusions can be drawn with the current size of uncertainties related to nPDF. Figure 8.5 shows the dependence on  $T_I$ , where only two different values have been used. Here the same logic from above applies, but a higher  $T_I$  corresponds to a longer evolution of the medium and thus more suppression. While, again, the shape remains relatively unchanged, the suppression is more pronounced and larger than PDF-related uncertainties. So some conclusions about initial temperatures can be gained from calculations. Also the aforementioned decrease of temperature with centrality can be observed. While the "ideal" critical temperature for centrality 0 – 10% appears to be slightly higher than the default value. In contrast,

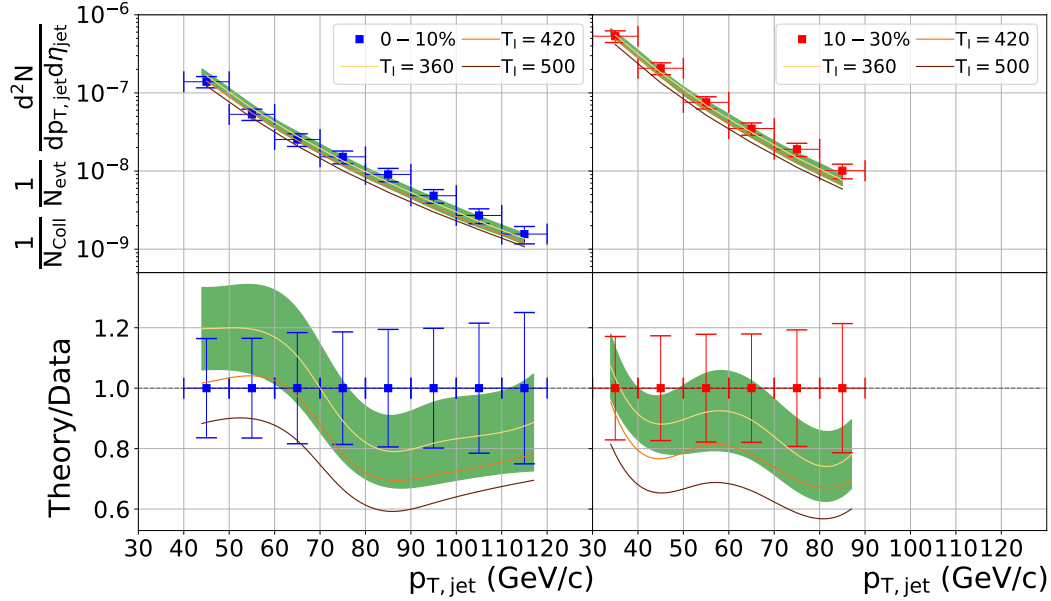


Figure 8.5: Dependence of the jet yield on the initial temperature  $T_I$  of the QGP. The default value in JEWEL for  $T_I$  is 360 MeV. The PDF uncertainties correspond to the green shaded band.

for centrality 10 – 30% a value lower than default would describe the ALICE data better. A point to remember, though, is that the JEWEL medium is based on a Bjorken model and thus a one-dimensional expansion, which corresponds to a rather slow cooling of the medium, as seen in section 5.1. A full three-dimensional expansion would induce a faster cooling and in turn reduce the effect of these temperature variations. To get more precise one would need to calculate the expansion in separate simulations to obtain sensible initial and critical temperatures for JEWEL, consistent with newer experimental values by comparison. Another caveat is the more general question about how well one- and three-dimensional medium models can be compared at all and three dimensional expansion is definitely happening in the experiment. But it is good to see that the jet yield behaves as expected with regard to temperature variations.

## 8.2 CMS

Next is the CMS analysis [31]. The general procedure will be exactly as outlined above; only the experimental cuts for the jets have changed. The CMS analysis also happens at  $\sqrt{s_{NN}} = 2.76$  TeV, but now a rapidity range of  $|\eta| < 2$  is considered. The results



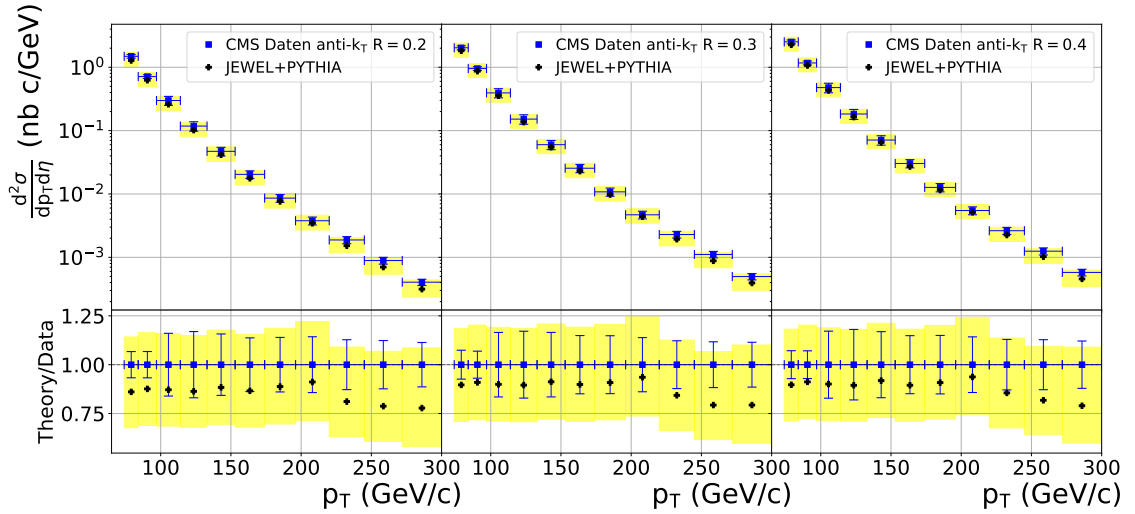


Figure 8.6: Comparison between the differential jet cross section for pp collisions at  $\sqrt{s} = 2.76$  TeV for different jet radii and  $|\eta| < 2$  obtained by CMS and JEWEL. The yellow shaded bands give the scale uncertainties. Data points taken from [31].

are reported for the anti- $k_T$  algorithm with three jet radii  $R = 0.2, 0.3$  and  $0.4$  in a  $p_T$ -range of  $70 < p_{T,\text{jets}} < 300$  GeV. For the comparison with JEWEL only the centrality  $0 - 5\%$  is used.

Starting again with the differential cross section in pp-collisions. The result can be seen in Figure 8.6, yellow shaded bands corresponding to the scale uncertainty. While the agreement of the shape generated by JEWEL is reasonable, with a slight drop in the high- $p_T$  bins, for the three jet radii, the overall prediction is too small. These deviations become smaller with increasing jet radius. For the most part, JEWEL is well within the experimental margin of error. The scale uncertainties are again quite large; comparable in size to the previous analysis. All experimental values are within these uncertainties.

Moving on to the jet yield in Pb+Pb collisions, shown in Figure 8.7. Green shaded bands correspond to the nCTEQ15 uncertainty and only the central member of EPPS16 is plotted as a comparison. The result obtained by JEWEL here is overall worse, at least compared to the ALICE analysis. For  $R = 0.2$  the first few bins agree nicely with experiment, but overall the jet yield is dropping too rapidly, with not even the errors from experiment and calculation overlapping. For the two larger jet radii the agreement is better, but also here the jet yield drops too rapidly in the last bins, with a tendency to decrease with an increase in jet radius. But at the same time larger jet

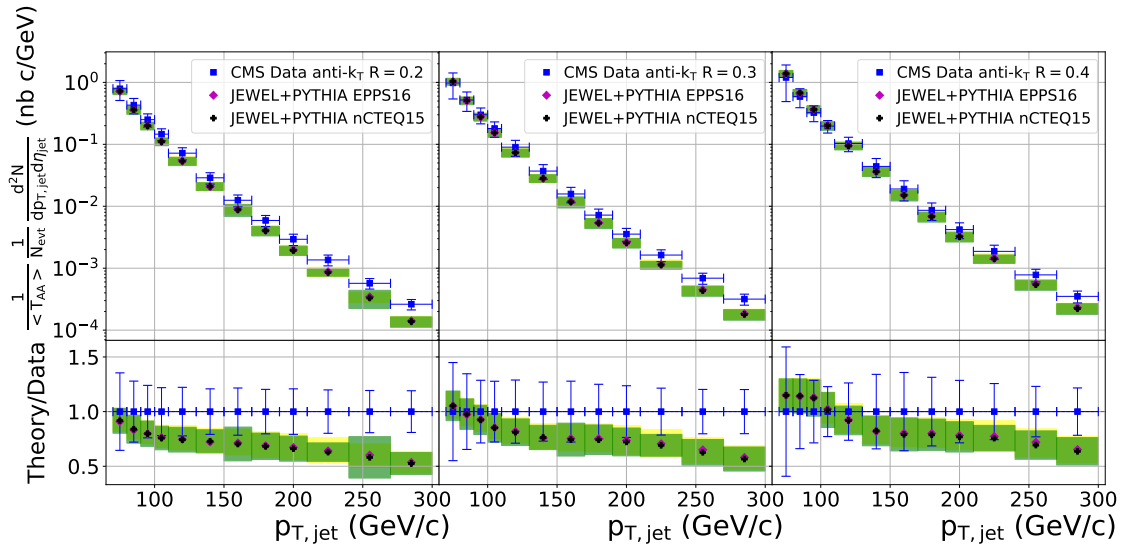


Figure 8.7: Comparison between the differential jet yield in Pb+Pb collisions at  $\sqrt{s} = 2.76$  TeV for different jet radii and  $|\eta| < 2$  obtained by CMS and JEWEL in the centrality range 0 – 5%. The yellow shaded bands give the scale uncertainties and the green shaded bands correspond to PDF uncertainties. Data points taken from [31].

radii seem to over-predict the jet yield in the low- $p_T$  region. In the given errors the results for  $R = 0.3$  and  $0.4$  agree quite nicely with experiment though. Here again the deviations from the central members of nCTEQ15 and EPPS16 are very small and uncertainties due to scale and PDF are roughly of equal size again.

Combing both for the nuclear modification factor results in Figure 8.8. The fact that the differential cross section and the jet yield are both too small on their own cancels somewhat in the ratio, so the prediction for  $R_{AA}$  is not too bad. But the sharper increase in the first bins is not replicated by JEWEL. While there is again an initial increase with  $p_T$ , this is not pronounced enough. The error margins of the experiment are especially large in these first bins and a JEWEL lies within these errors. Also for the last bins  $R_{AA}$  starts to drop, which corresponds to the behaviour of the jet yield, which decreases too strongly with larger  $p_T$ 's. For  $R = 0.3$  and  $0.4$  the nearly constant  $R_{AA}$  for the mid- $p_T$  range is replicated nicely. The error of  $R_{AA}$  is again dominated by the scale uncertainties, which were estimated in the same way as outlined above. In the margin of error there is a good general agreement between between JEWEL and data, which is satisfactory for a leading-order calculation.

The variation of  $T_C$  and  $T_I$  was also done for this analysis. The results for  $T_C$  can be seen in Figure 8.9 and for  $T_I$  in Figure 8.10. In general all the points mentioned for

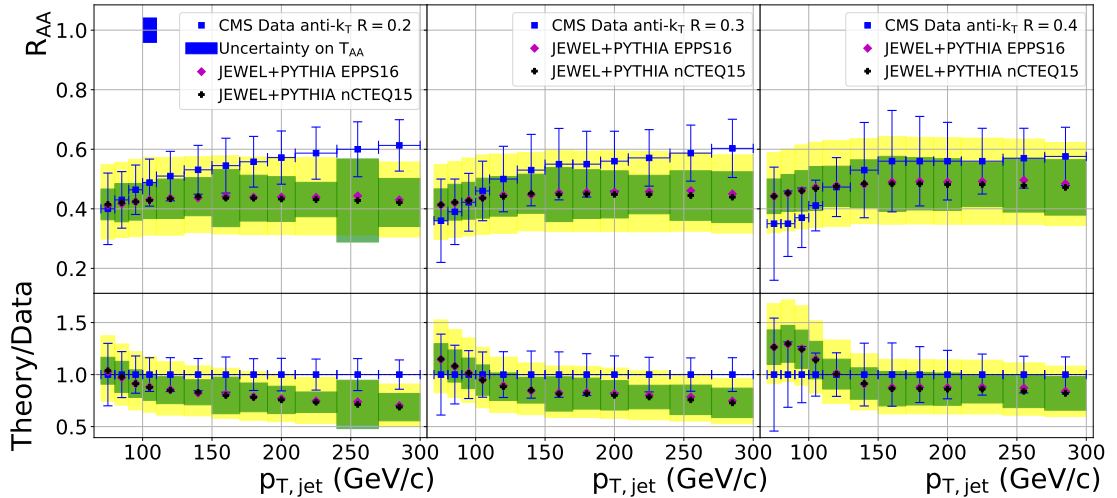


Figure 8.8: Comparison between the nuclear modification factor  $R_{AA}$  at  $\sqrt{s} = 2.76$  TeV for different jet radii and  $|\eta| < 2$  obtained by CMS and JEWEL in the centrality range 0 – 5%. The yellow shaded bands give the scale uncertainties and the green shaded bands correspond to PDF uncertainties. Data points taken from [31].

the temperature variation above apply here as well, with the effect of  $T_C$  appearing to be even smaller here. The behaviour of  $T_I$  at around 200 GeV seems curious. But since the statistical error, not shown here, also increases significantly at this point, it most likely is just a fluctuation caused by numerics, since the statistics of the runs are rather small. Further runs or runs with higher statistics will probably resolve this, but due to time constraints, pointing to the large error in these fluctuations has to suffice for ruling out anything special happening there. The fluctuation is at the same place for each jet radius since the underlying events are the same and just the jet radius has been varied in the analysis.

A further point to consider is the used rapidity interval. The rapidity-interval considered for these calculations with temperature variations may have been chosen too small. Due to scatterings in the medium, some partons, that would originally move within the cuts, can have their direction changed and not be included after analysis cuts have been applied. The reverse applies as well: partons that would not be included without medium can have their direction altered to land inside the analysis cuts. Because of this, the rapidity has to be larger than the analysis cuts, which in turn needs to be chosen even larger, if more interactions in the medium can happen with higher initial temperatures.

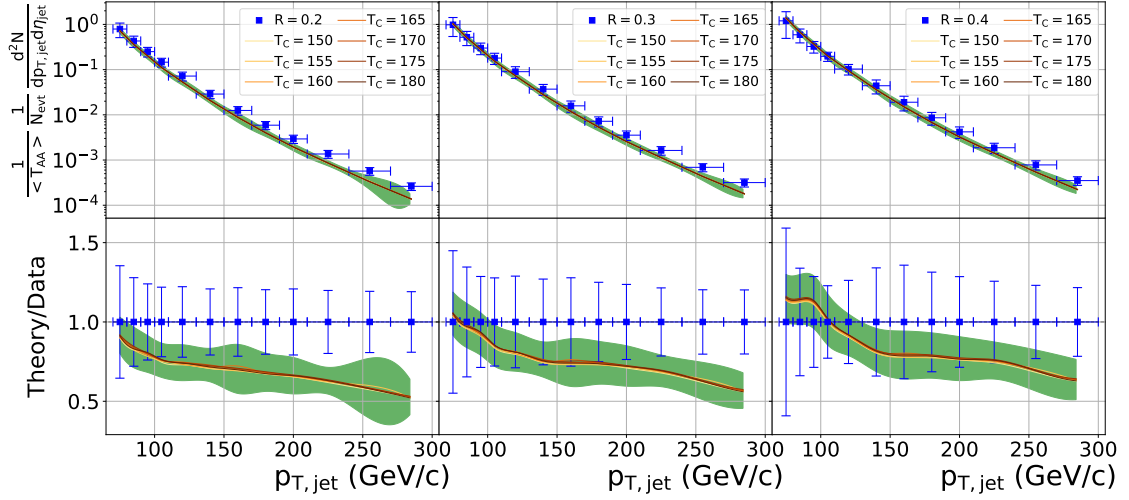


Figure 8.9: Dependence of the jet yield on the critical temperature  $T_C$  of the QGP. The default value in JEWEL for  $T_C$  is 170 MeV. The PDF uncertainties correspond to the green shaded band.

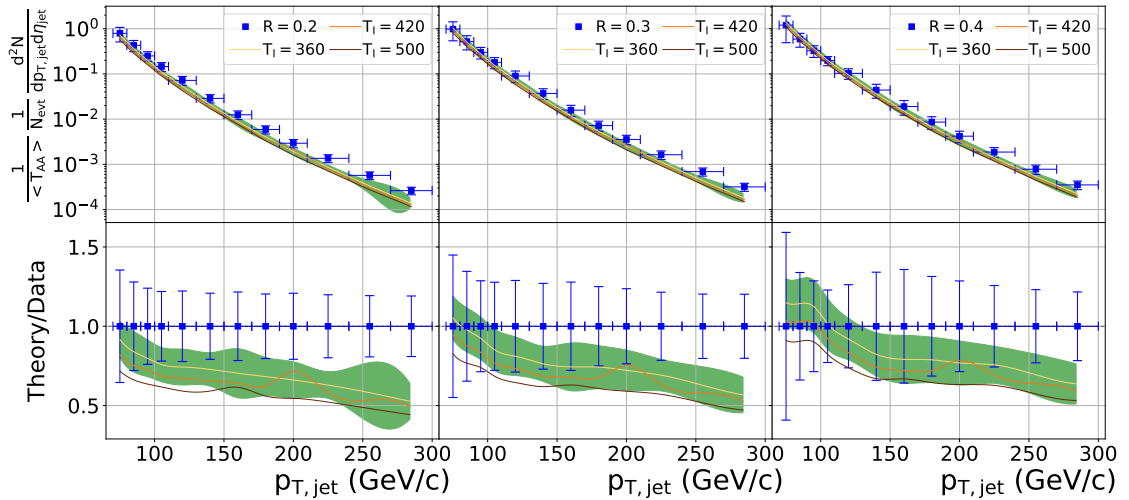


Figure 8.10: Dependence of the jet yield on the initial temperature  $T_I$  of the QGP. The default value in JEWEL for  $T_I$  is 360 MeV. The PDF uncertainties correspond to the green shaded band.

Due to time constraints, the effect of varying the rapidity range could not be included in this thesis. Increasing the initial temperature like this almost doubles the computation time again, while a larger rapidity range also has a noticeable effect. But in general the same conclusion as before follows, the effect of higher initial temperatures is larger

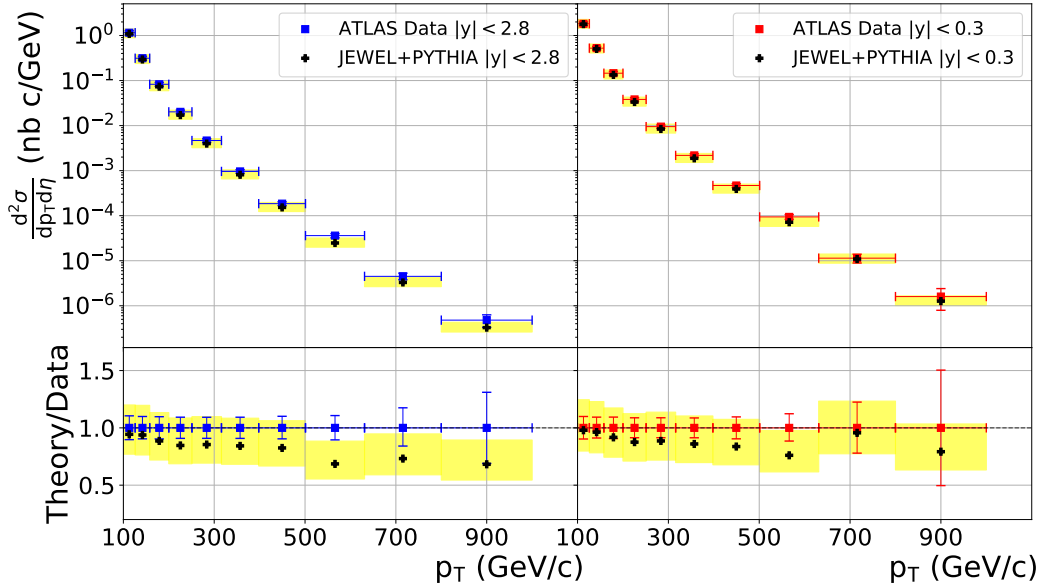


Figure 8.11: Comparison between the differential jet cross section for pp collisions at  $\sqrt{s} = 5.02$  TeV for jet radius  $R = 0.4$ ,  $|\eta| < 2.8$  (left) and  $|\eta| < 0.3$  (right) obtained by ATLAS and JEWEL. The yellow shaded bands give the scale uncertainties. Data points taken from [4].

than underlying uncertainties. The plot also shows a first hint of reduced suppression for high- $p_T$  jets. This will be discussed more below, since this effect is more pronounced in the next analysis.

### 8.3 ATLAS

Coming now to the last experimental analysis considered [4]. This ATLAS paper reports the jet yield and nuclear modification factor at  $\sqrt{s_{NN}} = 5.02$  TeV. In turn the  $p_T$ -range of the jets is considerably higher; it ranges from 100 GeV up to 1000 GeV in a rapidity interval  $|\eta| < 2.8$ . The anti- $k_T$  algorithm was used again with  $R = 0.4$ . Only the most central events in a centrality range of 0 – 10% are compared to predictions from JEWEL.

The differential cross section for pp-collisions can be seen in Figure 8.11 for  $|\eta| < 2.8$  on the left and  $|\eta| < 0.3$  on the right; yellow shaded bands corresponding to scale uncertainties. JEWEL is in good agreement with the measured differential cross section, with the prediction for the last  $p_T$ -bins being too small again. The results achieved for

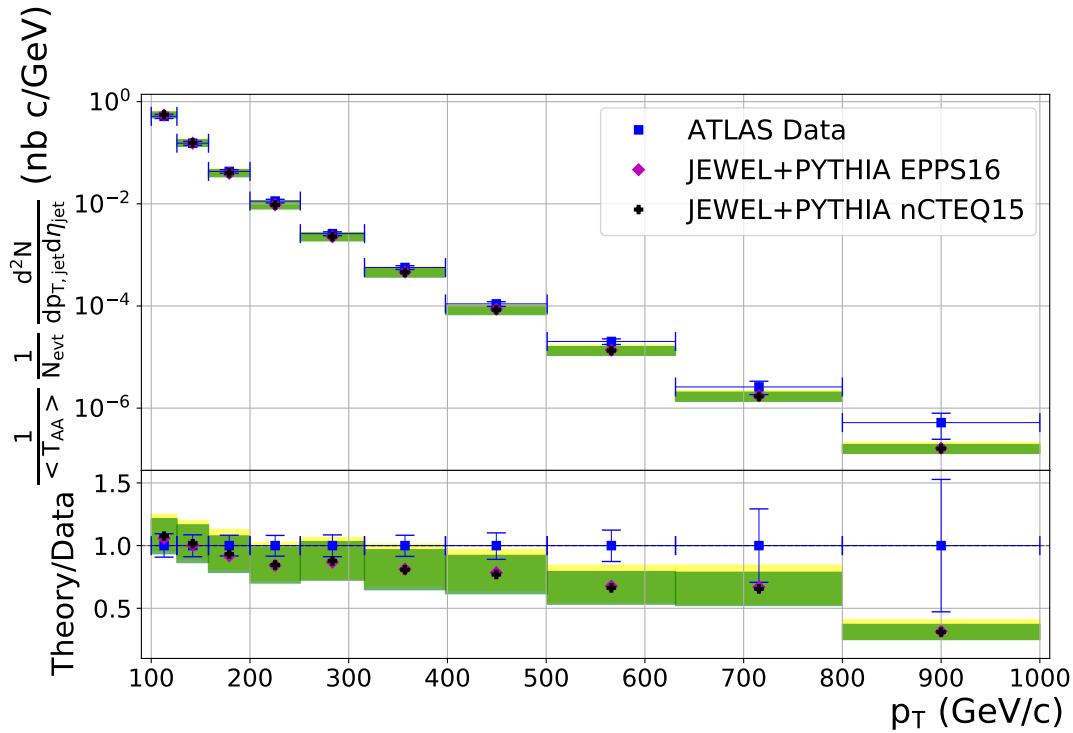


Figure 8.12: Comparison between the differential jet yield in Pb+Pb collisions at  $\sqrt{s} = 5.02$  TeV for jet radius  $R = 0.4$  and  $|\eta| < 2.8$  obtained by ATLAS and JEWEL in the centrality range 0 – 10%. The yellow shaded bands give the scale uncertainties and the green shaded bands correspond to PDF uncertainties. Data points taken from [4].

smaller rapidity intervals seems to fair better again, a trend also previously observed. The agreement here is excellent. The scale uncertainties are again quite large, with the upper edge of the band describing the data better again in general, as was the case with the CMS analysis. For leading-order the agreement is very satisfactory.

The differential jet yield in Pb+Pb collisions can be seen in Figure 8.12, where the green shaded bands correspond to the PDF uncertainties again. As in the previous analyses, scale and PDF uncertainties are roughly of equal magnitude. All in all JEWEL manages to replicate the measured data very nicely, minus the last  $p_T$ -bin, which JEWEL drastically underestimates. Also both central PDF members produce results in good agreement with each other.

Combining both gives the nuclear modification factor in Figure 8.13. Here again JEWEL under-predicts the initial increase in  $R_{AA}$ , but only slightly now. After a  $p_T$  of 200 GeV the agreement of JEWEL with data is excellent, reproducing  $R_{AA}$  over accurately over a very large  $p_T$ -range. Here again the scale uncertainties are the dominant factor, with all PDF uncertainties lying well within the yellow band.

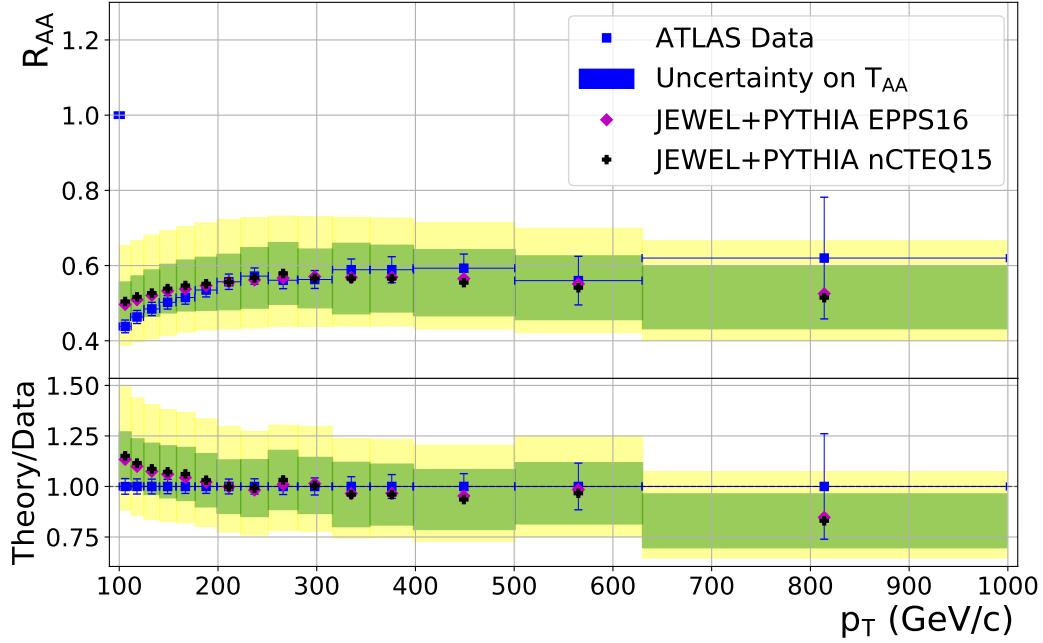


Figure 8.13: Comparison between the nuclear modification factor  $R_{AA}$  at  $\sqrt{s} = 5.02$  TeV for jet radius and  $|\eta| < 2.8$  obtained by ATLAS and JEWEL in the centrality range 0 – 10%. The yellow shaded bands give the scale uncertainties and the green shaded bands correspond to PDF uncertainties. Data points taken from [4].

A variation of the critical temperature, Figure 8.14, has also been done. The influence of this variation on the jet yield is again negligible. A more interesting result is the variation of the initial temperature seen in Figure 8.15. The irregular bumps in the plot are again due to statistics. The interesting point is, that the suppression is stronger for low- $p_T$  jets, where it produces effects that are larger than the PDF errors. For the high- $p_T$  jets this suppression is reduced, lying well within the margin of error. This suggests that very hard jets can pass the medium relatively unaffected. Following this train of thought leads to the conclusion, that the best strongly interacting probe for properties of the QGP are low-momentum jets, since these are especially sensible to medium effects. Also from the theoretical point this is the only regime where the effect is of comparable size to the underlying uncertainties.

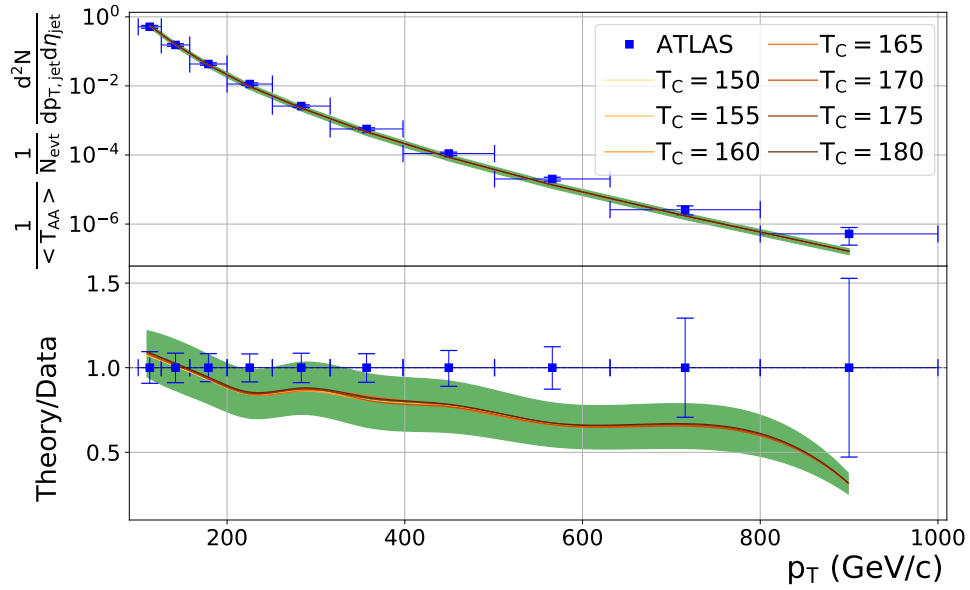


Figure 8.14: Dependence of the jet yield on the critical temperature  $T_C$  of the QGP. The default value in JEWEL for  $T_C$  is 170 MeV. The PDF uncertainties correspond to the green shaded band.

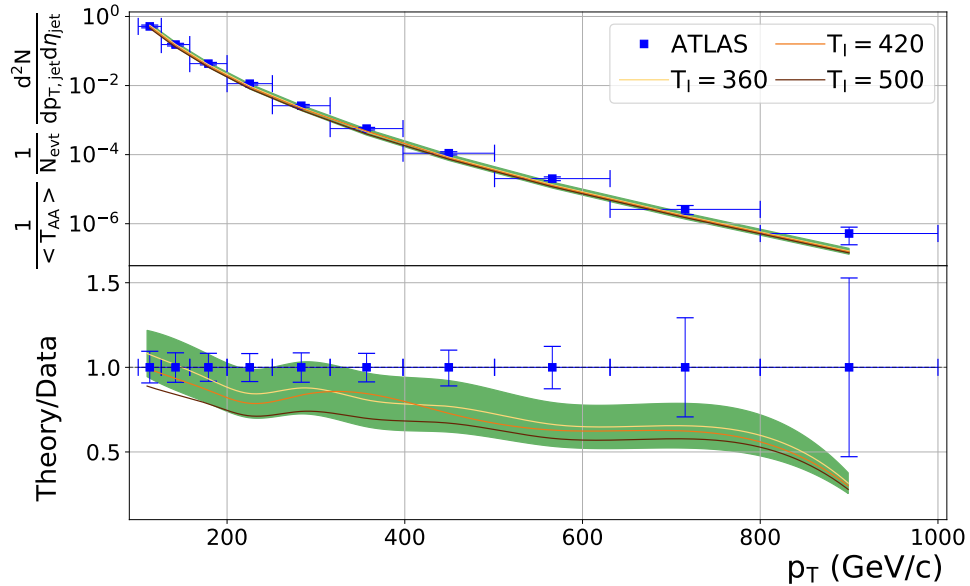


Figure 8.15: Dependence of the jet yield on the initial temperature  $T_I$  of the QGP. The default value in JEWEL for  $T_I$  is 360 MeV. The PDF uncertainties correspond to the green shaded band.



## 9 Conclusion

To recap, with the help of the LHAGLUE-interface it is possible to run code like JEWEL, that was built around PYTHIA-6.4, with up-to-date PDF sets like nCTEQ15 and EPPS16. The predictions of JEWEL for the nuclear modification factor were then tested against three experimental analyses from the LHC. For small rapidity intervals and transverse momentum jets in the case of the ALICE experiment (Figure 8.3) an excellent agreement was found. Going to a higher rapidity interval and higher  $p_T$ -jets, in the case of CMS, decreases the accuracy of JEWEL for the jet yield. The differential cross section (Figure 8.6) was replicated nicely with regard to the general shape, being slightly too small overall, mostly within margin of experimental error. There are, however, large scale uncertainties involved in the calculation. At the time of writing, the scale dependence is further investigated in next-to-leading order (NLO) calculations. The scale dependence in NLO should decrease and also one can deduce a more "natural" scale for the LO calculation from it. At the time of writing however this is still a work in progress. For the CMS analysis the scale  $p_T/2$  describes the data accurately. The jet yield (Figure 8.7) decreases too steeply, at least for small jet radii. The agreement becomes better when increasing the jet radius. Going to higher CMS energies in the case of ATLAS results in a better agreement for the jet yield in Pb+Pb collisions, while also, at least for the first bins, achieving a better result for the cross section in pp-collisions. A better result for smaller rapidity intervals was also found here. Both combined result in excellent agreement for  $R_{AA}$  (Figure 8.13); only the initial increase with  $p_T$  is underestimated slightly. This is also true for the  $R_{AA}$  obtained with regard to the CMS-analysis (Figure 8.8), there the errors on the experimental data is quite large in the first bins. All in all the results are in very good agreement with experimental data; considering that JEWEL works at leading order. It was also found that the uncertainties related to the scale and PDF's was of the same order of magnitude for the jet yield, while for the nuclear modification factor the

scale is the biggest factor of uncertainty despite the rather conservative estimate laid out in the previous chapter. Also it could be shown that the central PDF members of nCTEQ15 and EPPS16 give similar predictions for the jet yield in all three analyses. The effect of variations in the critical temperature turned out to be rather negligible, because they were very small compared to the other uncertainties involved. More interesting was the case of higher initial temperatures, where the suppression of the jet yield was greater than the PDF uncertainties, at least for jets with small  $p_T$ . The calculations showed that high- $p_T$  jets are very insensitive to medium effects, so no insights about e.g. the initial temperature can be gained from them with current PDF uncertainties. But, like previously mentioned, here sensible temperature values for the one-dimensional expansion in JEWEL would have to be obtained by other simulations first.

For future work there are many more jet observables available, which are sensitive to interactions with the medium, to test the capacity of JEWEL and the performance of newer PDF sets. See for example the long list in chapter 7, which by no means claims to be complete. Otherwise the investigation of the nuclear modification factor could be extended to the case of peripheral Pb+Pb scatterings, since in this thesis only the most central intervals were considered in each analysis. A variation of initial temperature should also be included then, since, as it was shown for the ALICE analysis, the initial temperature for peripheral collisions has to be lower than for central ones. The CMS and ATLAS paper report results over a large centrality range, giving opportunity to directly extend the analysis of this thesis.

# Acknowledgements

I would like to express my gratitude to the following people as a closing remark of this thesis:

- Prof. Dr. Michael Klasen, for providing the opportunity to research this topic.
- Dr. Jens Salomon, for the many long discussions and help along the way which is much appreciated.
- PD. Dr Karol Kovarik, for PDF related inputs and for always creating a nice atmosphere.
- Hendrik Poppenborg, for the initial introduction to the world of event generators.
- Simon May, for proofreading.
- My office colleagues, for many entertaining moments during my stay.
- The rest of the group, for the lively discussions during the afternoon break.
- My girlfriend, for putting up with me, especially over the last months of this thesis.

# A Calculation of invariant matrix elements in pQCD at tree level

Three matrix elements will be calculated here. The quarks will be taken as massless. The results can be checked with [23] or for the gluon scattering [40].

## A.1 $q\bar{q} \rightarrow q'\bar{q}'$

Starting with the easiest process, the annihilation of a quark-antiquark pair into a pair of another flavour. There is just one diagram contributing to this process, the s-channel diagram. Taking the Feynman rules from chapter 2 in the Feynman-t'Hooft gauge  $\xi = 1$  one obtains:

$$\begin{aligned}
 i\mathcal{M}_s = & \begin{array}{c} q \\ \swarrow p_1 \\ \text{---} p \\ \searrow p_2 \\ \bar{q} \end{array} \begin{array}{c} \text{---} p \\ \swarrow p_3 \\ q' \\ \searrow p_4 \\ \bar{q}' \end{array} \\
 & = \bar{v}(p_2)ig\gamma^\mu T_{ij}^a u(p_1) \frac{-ig^{\mu\nu}}{p^2} \delta^{ab} \bar{u}(p_3)ig\gamma^\nu T_{kl}^b v(p_4) \\
 & = iT_{ij}^a T_{kl}^a \frac{g^2}{s} \bar{v}(p_2)\gamma^\mu u(p_1)\bar{u}(p_3)\gamma_\mu v(p_4), \quad (\text{A.1})
 \end{aligned}$$

where  $s = p^2 = (p_1 + p_2)^2$  and some indices have been contracted. The colour indices of the spinors have been suppressed here, since it is easier in most cases to calculate the diagram and the colour factor separately. To calculate the squared matrix element, the complex conjugate of the above is needed. The relations  $\gamma_\mu^\dagger \gamma_0 = \gamma_0 \gamma_\mu$  and  $\gamma_0^\dagger = \gamma_0$  are needed to obtain:

$$\mathcal{M}_s^\dagger = \frac{g^2}{s} T_{ij}^a T_{kl}^a \bar{v}(p_4)\gamma_\mu u(p_3)\bar{u}(p_1)\gamma^\mu v(p_2). \quad (\text{A.2})$$

Taking both together yields:

$$|\mathcal{M}|^2 = \frac{g^4}{s^2} (T_{ij}^a T_{kl}^a)^2 [\bar{v}(p_2) \gamma^\mu u(p_1)] [\bar{u}(p_3) \gamma_\mu v(p_4)] [\bar{v}(p_4) \gamma_\nu u(p_3)] [\bar{u}(p_1) \gamma^\nu v(p_2)]. \quad (\text{A.3})$$

The quantities in the brackets are just numbers, so they can be freely rearranged. Taking a sum over the spins and averaging over initial spins with the identity, which like some trace relations used later can be found in the textbooks,  $\sum_s v_\alpha^s(p_4) \bar{v}_\beta^s(p_4) = \left( \not{p}_4 \right)_{\alpha\beta}$ , which in the case for massless quarks is the same for a sum over the  $u$ , this becomes

$$\frac{1}{4} \sum_{\text{spin}} |\mathcal{M}|^2 = \sum_{s,s'} \frac{g^4}{4s^2} (T_{ij}^a T_{kl}^a)^2 \bar{v}^s(p_2) \gamma^\mu \not{p}_1 \gamma_\nu v^s(p_2) \bar{u}^{s'}(p_3) \gamma_\mu \not{p}_4 \gamma^\nu u^{s'}(p_3). \quad (\text{A.4})$$

There are still two spin sums left to be done. To do this, one decomposes the expression in index notation; since there everything is just a number, one is again free to rearrange:

$$\begin{aligned} \sum_s \bar{v}^s(p_2) \gamma^\mu \not{p}_1 \gamma_\nu v^s(p_2) &= \sum_s \bar{v}_\beta^s(p_2) (\gamma^\mu)_{\beta\delta} \left( \not{p}_1 \right)_{\delta\zeta} (\gamma_\nu)_{\zeta\alpha} v_\alpha^s(p_2) \\ &= \left( \not{p}_1 \right)_{\delta\zeta} (\gamma_\nu)_{\zeta\alpha} \left( \not{p}_2 \right)_{\alpha\beta} (\gamma^\mu)_{\beta\delta} = \text{tr} \left( \not{p}_1 \gamma_\nu \not{p}_2 \gamma^\mu \right). \end{aligned} \quad (\text{A.5})$$

This trick will be used a lot in calculations, and so equation (A.4) becomes

$$\frac{1}{4} \sum_{\text{spin}} |\mathcal{M}|^2 = \frac{g^4}{4s^2} (T_{ij}^a T_{kl}^a)^2 \text{tr} \left( \not{p}_1 \gamma^\nu \not{p}_2 \gamma^\mu \right) \text{tr} \left( \not{p}_3 \gamma_\mu \not{p}_4 \gamma_\nu \right). \quad (\text{A.6})$$

At this point one can show a whole host of relations for traces over gamma matrices; needed here is the relation

$$\text{tr}(\gamma^\alpha \gamma^\mu \gamma^\beta \gamma^\nu) = 4(g^{\alpha\mu} g^{\beta\nu} - g^{\alpha\beta} g^{\mu\nu} + g^{\alpha\nu} g^{\mu\beta}), \quad (\text{A.7})$$

also for completeness the slash notation used above is  $\not{p} = p_\mu \gamma^\mu$ . Inserting this into the expression yields

$$\frac{1}{4} \sum_{\text{spin}} |\mathcal{M}|^2 = \frac{4g^4}{s^2} (T_{ij}^a T_{kl}^a)^2 p_1^\alpha p_2^\beta (g^{\alpha\nu} g^{\beta\mu} - g^{\alpha\beta} g^{\mu\nu} + g^{\alpha\mu} g^{\nu\beta}) p_3^\rho p_4^\sigma (g^{\rho\mu} g^{\sigma\nu} - g^{\rho\sigma} g^{\mu\nu} + g^{\rho\nu} g^{\sigma\mu})$$

Contracting all the momenta with the shorthand notation  $p_{ij} = p_i p_j$  leads to

$$\frac{1}{4} \sum_{\text{spin}} |\mathcal{M}|^2 = \frac{4g^4}{s^2} (T_{ij}^a T_{kl}^a)^2 (2p_{14} p_{23} + 2p_{13} p_{24}). \quad (\text{A.8})$$

Introducing the Mandelstam variables for massless particles

$$s = 2p_{12} = 2p_{34}, \quad (\text{A.9})$$

$$t = -2p_{13} = -2p_{24}, \quad (\text{A.10})$$

$$u = -2p_{14} = -2p_{23}, \quad (\text{A.11})$$

to simplify this further gives

$$\frac{1}{4} \sum_{\text{spin}} |\mathcal{M}|^2 = \frac{2g^4}{s^2} (T_{ij}^a T_{kl}^a)^2 (t^2 + u^2). \quad (\text{A.12})$$

All that is left now is to calculate the colour factor using a Fierz identity

$$\sum_a T_{ij}^a T_{kl}^a = \frac{1}{2} \left( \delta_{il} \delta_{kj} - \frac{1}{3} \delta_{ij} \delta_{kl} \right) \quad (\text{A.13})$$

and the properties of the Kronecker delta  $\delta_{il} \delta_{il} = \delta_{ii} = 3$  to obtain

$$\begin{aligned} (T_{ij}^a T_{kl}^a)^2 &= \frac{1}{4} \left( \delta_{il} \delta_{kj} - \frac{1}{3} \delta_{ij} \delta_{kl} \right) \left( \delta_{il} \delta_{kj} - \frac{1}{3} \delta_{ij} \delta_{kl} \right) \\ &= \frac{1}{4} \left( \delta_{ll} \delta_{kk} - \frac{1}{3} \delta_{lk} \delta_{lk} - \frac{1}{3} \delta_{lk} \delta_{lk} + \frac{1}{9} \delta_{jj} \delta_{lk} \delta_{lk} \right) \\ &= \frac{1}{4} \left( 3\delta_{ll} - \frac{1}{3} \delta_{ll} - \frac{1}{3} \delta_{ll} + \frac{1}{3} \delta_{ll} \right) \\ &= \frac{1}{4} (9 - 1) = 2. \end{aligned} \quad (\text{A.14})$$

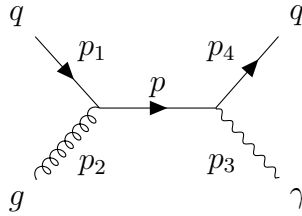
The quark can have one of three colours and so can the antiquark, giving in total nine combinations. Since there can be no way of knowing about the colour state one has to average over it, giving an additional factor of  $\frac{1}{9}$ . So the end result for the invariant matrix element squared for quark-antiquark-annihilation into a pair of a different flavour is

$$\frac{1}{36} \sum_{\substack{\text{spin} \\ \text{colour}}} |\mathcal{M}|^2 = \frac{4g^4}{9} \left( \frac{t^2 + u^2}{s^2} \right). \quad (\text{A.15})$$

## A.2 $qg \rightarrow q\gamma$

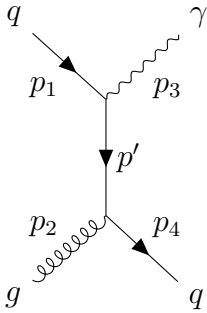
The next process is a quark and a gluon going into a quark and a photon. There are some QED Feynman rules needed now, which in general are not very different from

the QCD ones. Just leave out delta's signifying colour conservation from propagators, since QED does not interact with the colour charge. Also for QED there is just one vertex, which governs the interaction of photons with charged fermions. This vertex is identical to the quark-gluon vertex equation (2.26), albeit a bit simpler. Since QED is based on the Abelian group U(1) there are no generators in the expression. Also, obviously, the strong coupling has to be replaced by the electric charge of the fermion. Incoming and outgoing gluons and electrons are associated with polarization vectors  $\epsilon_\mu(p)$ ; summing over polarizations later will give  $\sum_{\text{pol}} \epsilon_\mu^* \epsilon_\nu \rightarrow g_{\mu\nu}$ . Two diagrams contribute to this process, an s-channel annihilation diagram and a t-channel scattering diagram. Starting with the s-channel, the diagram is



$$i\mathcal{M}_s = \bar{u}(p_4)(-i)e_f\gamma^\mu\epsilon_\mu^*(p_3)\frac{i\not{p}\delta_{ik}}{p^2}u(p_1)ig\gamma^\nu T_{ij}^a\epsilon_\nu(p_2) \quad (\text{A.16})$$

where again  $p = p_1 + p_2$  and  $e_f$  is the fractional charge of the quark. Next the t-channel diagram:



$$i\mathcal{M}_t = \bar{u}(p_4)ig\gamma^\nu T_{ki}^a\epsilon_\nu(p_2)\frac{i\not{p}'\delta_{ij}}{p'^2}u(p_1)(-i)e_f\gamma^\mu\epsilon_\mu^*(p_3) \quad (\text{A.17})$$

where  $p' = p_1 - p_3$ . For completeness, the incoming quark has the colour  $j$ , the outgoing the colour  $k$  and the virtual quark has the colour  $i$ . The colour is conserved in the propagator and in the QED vertex. Adding both together gives the matrix element  $\mathcal{M} = \mathcal{M}_s + \mathcal{M}_t$ . Now the complex conjugate for the calculation is needed, which can be given as

$$\mathcal{M}^\dagger = e_f g \epsilon_\alpha^*(p_2) \epsilon_\beta(p_3) \bar{u}(p_1) \left[ T_{ji}^a \gamma^\alpha \frac{\not{p} \delta_{ik}}{s} \gamma^\beta + T_{ik}^a \gamma^\beta \frac{\not{p}' \delta_{ij}}{t} \gamma^\alpha \right] u(p_4), \quad (\text{A.18})$$

where the Mandelstam variables from before were used again. Squaring the matrix element yields

$$|\mathcal{M}|^2 = |\mathcal{M}_s|^2 + |\mathcal{M}_t|^2 + |\mathcal{M}_s \mathcal{M}_t^\dagger| + |\mathcal{M}_t \mathcal{M}_s^\dagger|. \quad (\text{A.19})$$

Each term will be dealt with separately. Starting with the s-channel squared and summing over polarizations gives

$$\sum_{\text{pol.}} |\mathcal{M}_s|^2 = \frac{e_f^2 g^2}{s^2} g_{\alpha\nu} g_{\beta\mu} T_{ij}^a T_{ji}^a \bar{u}(p_4) \gamma^\mu \not{p} \gamma^\nu u(p_1) \bar{u}(p_1) \gamma^\alpha \not{p} \gamma^\beta u(p_4). \quad (\text{A.20})$$

Contracting the gamma matrices with the metrics, summing over spins in the final and averaging over initial spin and using equation (2.17) leads to

$$\frac{1}{4} \sum_{\substack{\text{pol.} \\ \text{spin}}} |\mathcal{M}_s|^2 = \frac{e_f^2 g^2}{4s^2} T_F \bar{u}(p_4) \gamma^\mu \not{p} \gamma^\nu \not{p}_1 \gamma^\nu \not{p} \gamma^\mu u(p_4). \quad (\text{A.21})$$

Some useful relations between gamma-matrices now are for the case of one intermediate matrix  $\gamma^\mu \gamma^\nu \gamma_\mu = -2\gamma^\nu$  and for three  $\gamma^\mu \gamma^\nu \gamma^\rho \gamma^\sigma \gamma_\mu = -2\gamma^\sigma \gamma^\rho \gamma^\nu$ . With these two relations and the calculation trick from the last section this expression reduces to

$$\frac{1}{4} \sum_{\substack{\text{pol.} \\ \text{spin}}} |\mathcal{M}_s|^2 = \frac{e_f^2 g^2}{s^2} T_F \text{tr}(\not{p}_4 \not{p} \not{p}_1 \not{p}). \quad (\text{A.22})$$

The calculation has been done in the last section; with  $T_F = \frac{1}{2}$  this becomes

$$\frac{1}{4} \sum_{\substack{\text{pol.} \\ \text{spin}}} |\mathcal{M}_s|^2 = 2 \frac{e_f^2 g^2}{s^2} (2p_{12} p_{34} - 2p_{12} p_{14}) = \frac{e_f^2 g^2}{s^2} (s^2 + su) = e_f^2 g^2 \left( -\frac{t}{s} \right), \quad (\text{A.23})$$

where  $s + t + u = 0$  for massless particles has been used in the last step. Averaging over the colours of the quark for the final expression gives:

$$\frac{1}{12} \sum_{\substack{\text{pol.} \\ \text{spin} \\ \text{colour}}} |\mathcal{M}_s|^2 = -\frac{1}{3} e_f^2 g^2 \left( \frac{t}{s} \right). \quad (\text{A.24})$$



Since  $t < 0$  and  $s > 0$  this result is indeed positive. There is nothing new to learn from calculating the squared t-channel. The steps are basically the same, one just swaps the  $s$  and  $t$  in the end, resulting in

$$\frac{1}{12} \sum_{\substack{\text{pol.} \\ \text{spin} \\ \text{colour}}} |\mathcal{M}_s|^2 = -\frac{1}{3} e_f^2 g^2 \left( \frac{s}{t} \right). \quad (\text{A.25})$$

All that is left now are the interference terms. Starting with

$$\sum_{\text{pol}} |\mathcal{M}_s \mathcal{M}_t^\dagger| = \frac{e_f^2 g^2}{st} g_{\alpha\nu} g_{\beta\mu} T_{ij}^a T_{ab}^a \bar{u}(p_4) \gamma^\mu \not{p} \gamma^\nu u(p_1) \bar{u}(p_1) \gamma^\beta \not{p}' \gamma^\alpha u(p_4). \quad (\text{A.26})$$

Performing the sum over spins leads to

$$\frac{1}{4} \sum_{\substack{\text{pol.} \\ \text{spin}}} |\mathcal{M}_s \mathcal{M}_t^\dagger| = \frac{e_f^2 g^2}{st} T_{ij}^a T_{ab}^a \bar{u}(p_4) \gamma^\mu \not{p} \gamma^\nu \not{p}_1 \gamma^\mu \not{p}' \gamma^\nu u(p_4). \quad (\text{A.27})$$

Focusing on the gamma-matrix part, we can use the relation from before to simplify

$$\gamma^\mu \not{p} \gamma^\nu \not{p}_1 \gamma^\mu \not{p}' \gamma^\nu = -2 \not{p}_1 \gamma^\nu \not{p} \not{p}' \gamma_\nu. \quad (\text{A.28})$$

Using a relation for two intermediate matrices  $\gamma^\mu \gamma^\nu \gamma^\rho \gamma_\mu = 4g^{\nu\rho}$  this becomes

$$-2 \not{p}_1 \gamma^\nu \not{p} \not{p}' \gamma_\nu = -8 \not{p}_1 p^\mu p'_\mu. \quad (\text{A.29})$$

Inserting  $p = p_1 + p_2$  and  $p' = p_1 - p_3$  and using the Mandelstam variables the contracted momenta yield

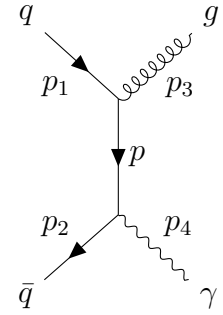
$$pp' = (p_1 + p_2)(p_1 - p_3) = p_1^2 - p_1 p_3 + p_1 p_2 - p_2 p_3 = 0 + t + s + u = 0 \quad (\text{A.30})$$

so this interference term vanishes for massless particles. As before the calculation for the second term is identical: the other interference term also vanishes. So in total the squared invariant matrix element for this process is

$$\frac{1}{12} \sum_{\substack{\text{pol.} \\ \text{spin} \\ \text{colour}}} |\mathcal{M}|^2 = -\frac{1}{3} e_f^2 g^2 \left( \frac{s}{t} + \frac{t}{s} \right). \quad (\text{A.31})$$

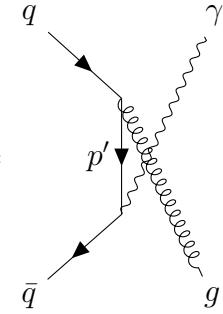
### A.3 $q\bar{q} \rightarrow g\gamma$

A process that is similar to the last one is the quark-antiquark annihilation into a gluon and a photon. Both these processes together are all contributions from QCD to the so-called prompt photon production at tree level. The process  $q\bar{q} \rightarrow g\gamma$  has two contributions again, a t-channel diagram and an u-channel diagram. The t-channel looks as follows



$$i\mathcal{M}_t = \bar{v}(p_2)(-i)e_f\gamma^\mu\epsilon_\mu^*(p_4)\frac{i\not{p}\delta_{jk}}{p^2}u(p_1)ig\gamma^\nu T_{ij}^a\epsilon_\nu^*(p_3), \quad (\text{A.32})$$

where  $p = p_1 - p_3$ . For the u-channel one obtains



$$i\mathcal{M}_u = \bar{v}(p_2)(-i)e_f\gamma^\mu\epsilon_\mu^*(p_3)\frac{\not{p}'\delta_{jk}}{p'^2}\epsilon_\nu^*(p_4)T_{ji}^aig\gamma^\nu u(p_1), \quad (\text{A.33})$$

where  $p' = p_1 - p_4$ . In both diagrams the index  $i$  is the colour of the ingoing quark and  $j$  the colour of the antiquark. The complex conjugated matrix elements are computed for this to calculate the total squared matrix element

$$|\mathcal{M}|^2 = |\mathcal{M}_t|^2 + |\mathcal{M}_u|^2 + |\mathcal{M}_t\mathcal{M}_u^\dagger| + |\mathcal{M}_u\mathcal{M}_t^\dagger|. \quad (\text{A.34})$$

Not only do these diagrams look very similar to the diagrams of the last process, the calculation of the diagrams follows all the same steps. The results for the squared s-

and u-channel have an identical form and all interference terms will come out as zero for massless particles again. Doing the explicit calculation for these diagrams leads to

$$\frac{1}{36} \sum_{\substack{\text{pol.} \\ \text{spin} \\ \text{colour}}} |\mathcal{M}|^2 = -\frac{8}{9} e_f^2 g^2 \left( \frac{u}{t} + \frac{t}{u} \right). \quad (\text{A.35})$$

There is a symmetry called crossing symmetry, which lets one reproduce results from calculations with a rotated diagram. Here it leads to a replacement of  $s$  with  $u$ , so the result does not have to be calculated explicitly again. Of course this is not a real physical symmetry, but it gives relations which can save some work. More on this can be found in textbooks. Of course another colour factor is associated with these diagrams, since the initial state and colour factor are different.

## A.4 $gg \rightarrow gg$

The last process is only possible in non-Abelian theories: the scattering of gauge-bosons, since they carry a charge and can therefore self-interact. There is no such process in QED, well at least there is no scattering at leading order. Higher-order terms can exist though. This self-interaction drastically increases the number of diagrams that have to be calculated. Also the naive calculation of gluon scattering is very cumbersome and involves a huge quantity of terms, which in the end will give zero. There is a more efficient way to do these calculations in the spinor-helicity formalism. First some basic points about this formalism, following Schwartz [40], will be gathered and afterwards comes the calculation. For this section all momenta are chosen as incoming.

### A.4.1 Spinor-Helicity Formalism

The spinor-helicity formalism is based on bispinors  $P_{\alpha\dot{\alpha}}$ , since momenta transform in the  $(\frac{1}{2}, \frac{1}{2})$  representation of the Lorentz group. Introducing left-handed Weyl spinors  $\psi_\alpha$  transforming in  $(\frac{1}{2}, 0)$  and right-handed  $\psi_{\dot{\alpha}}$  transforming in  $(0, \frac{1}{2})$  one can define

helicity spinors as doublets transforming in one of the two representations. With this one can give inner products as

$$\langle \lambda \chi \rangle = \varepsilon^{\alpha\beta} \lambda_\alpha \chi_\beta = \lambda_\alpha \chi^\alpha = -\lambda^\alpha \chi_\alpha, \quad [\lambda \chi] = \varepsilon^{\dot{\alpha}\dot{\beta}} \lambda_{\dot{\alpha}} \chi_{\dot{\beta}} = \lambda_{\dot{\alpha}} \chi^{\dot{\alpha}} = -\lambda^{\dot{\alpha}} \chi_{\dot{\alpha}}, \quad (\text{A.36})$$

where  $\varepsilon^{\alpha\beta}$  can lower or raise indices like  $g^{\mu\nu}$ , but is antisymmetric:

$$\varepsilon^{\alpha\beta} = -\varepsilon_{\alpha\beta} = \varepsilon^{\dot{\alpha}\dot{\beta}} = -\varepsilon_{\dot{\alpha}\dot{\beta}} = \begin{pmatrix} 0 & 1 \\ -1 & 0 \end{pmatrix}. \quad (\text{A.37})$$

Also the helicity spinors are anti-symmetric:

$$\langle \lambda \chi \rangle = -\langle \chi \lambda \rangle, \quad [\lambda \chi] = -[\chi \lambda], \quad (\text{A.38})$$

which ultimately leads to

$$\langle \lambda \lambda \rangle = [\lambda \lambda] = 0. \quad (\text{A.39})$$

With help of the  $\sigma$ -matrices one can give momenta as bispinors from four-vectors and the other way around:

$$p^{\alpha\dot{\alpha}} \equiv \sigma_\mu^{\alpha\dot{\alpha}} p^\mu, \quad p_{\dot{\alpha}\alpha} \equiv \bar{\sigma}_\mu^{\dot{\alpha}\alpha} p_\mu, \quad p^\mu \equiv \frac{1}{2} \sigma^{\mu\alpha\dot{\alpha}} p_{\dot{\alpha}\alpha}, \quad p_\mu \equiv \frac{1}{2} \bar{\sigma}_\mu^{\dot{\alpha}\alpha} p^{\alpha\dot{\alpha}}. \quad (\text{A.40})$$

A very useful property for the case of massless particles like gluons is  $\det(p^{\alpha\dot{\alpha}}) = 0$ , so that matrices can be given as an outer product

$$p^{\alpha\dot{\alpha}} = \lambda^\alpha \tilde{\lambda}^{\dot{\alpha}} = p \rangle [p], \quad (\text{A.41})$$

where the last equality is a convenient notation for this. The product of two massless vectors then becomes

$$p \cdot q = \frac{1}{2} \langle \lambda \chi \rangle [\chi \lambda]. \quad (\text{A.42})$$

For some useful relations, writing  $i]$  for  $p_i]$  one can write with momentum conservation

$$\sum_j \langle ij \rangle [jk] = 0 \quad (\text{A.43})$$

and a given spinor can be given in terms of two others

$$1\rangle = \frac{\langle 13\rangle}{\langle 23\rangle}2\rangle - \frac{\langle 12\rangle}{\langle 23\rangle}3\rangle \quad (\text{A.44})$$

which leads to the Schouten identity

$$\langle 12\rangle\langle 34\rangle + \langle 13\rangle\langle 42\rangle + \langle 14\rangle\langle 23\rangle = 0. \quad (\text{A.45})$$

For gluons one also needs to construct polarisation vectors, which satisfy the relations  $\epsilon_\mu^* \epsilon^\mu = -1$  and  $p_\mu \epsilon^\mu = 0$ . Additionally another four-momentum, the reference momentum,  $r^\mu$  is introduced. This reference momentum must not be aligned with the momentum  $p^\mu$  of the gluon ( $r \cdot p \neq 0$ ). This is the only constraint on choosing the reference momentum. The aforementioned relations can be fulfilled by

$$[\epsilon_p^-(r)]^{\alpha\dot{\alpha}} = \sqrt{2} \frac{p\rangle[r}{[pr]}, \quad [\epsilon_p^+(r)]^{\alpha\dot{\alpha}} = \sqrt{2} \frac{r\rangle[p}{\langle rp)}. \quad (\text{A.46})$$

With these definitions  $\epsilon^+ \cdot \epsilon^+ = \epsilon^- \cdot \epsilon^- = \epsilon^\pm \cdot p = 0$  also follows. In calculations it is convenient to take the reference momentum as the momentum of another gluon in the problem. As a shorthand  $\epsilon_i(j)$  is the polarisation vector of a gluon  $i$  with momentum  $p_i^\mu$  and reference momentum  $r^\mu = p_j^\mu$ . With this all possible contractions can be worked out:

$$\epsilon_1^-(i) \cdot \epsilon_2^-(j) = \frac{\langle 12\rangle[ji]}{[1i][2j]}, \quad p_1 \cdot p_2 = \frac{1}{2}\langle 21\rangle[12], \quad (\text{A.47})$$

$$\epsilon_1^-(i) \cdot \epsilon_2^+(j) = \frac{\langle 1j\rangle[2i]}{[1i]\langle j2\rangle}, \quad \epsilon_1^+(i) \cdot \epsilon_2^+(j) = \frac{\langle ij\rangle[21]}{\langle i1\rangle\langle j2\rangle}, \quad (\text{A.48})$$

$$\epsilon_1^-(i) \cdot p_3 = \frac{1}{\sqrt{2}} \frac{\langle 13\rangle[3i]}{[1i]}, \quad \epsilon_1^+(i) \cdot p_3 = \frac{1}{\sqrt{2}} \frac{[13]\langle 3i\rangle}{\langle i1\rangle} \quad (\text{A.49})$$

By choosing one reference momentum for all gluons one obtains

$$\epsilon_i^+(r) \cdot \epsilon_j^+(r) = \frac{\langle rr\rangle[ji]}{\langle ri\rangle\langle ri\rangle} = 0, \quad (\text{A.50})$$

leading to a quite general result. Namely, all amplitudes with all positive or negative helicities vanish at tree level in QCD. It can be further shown that only amplitudes with two negative and two positive helicities contribute, these are called maximum helicity-violating (MHV).

### A.4.2 Diagrams

For the calculation the diagram will be calculated first and the colour factor will be treated afterwards. Also it is enough to calculate one MHV amplitude and get the other results by crossing. The MHV amplitude calculated will be  $\mathcal{M}(1^-, 2^-, 3^+, 4^+)$ . For the following matrix elements this will be left implicit. Also the Mandelstam variables in this section will be  $t = (p_1 + p_4)^2$ ,  $u = (p_1 + p_3)^2$  and finally  $s = (p_1 + p_2)^2$ , while still fulfilling  $s + t + u = 0$ . Choosing the reference momentum for  $\epsilon_1$  and  $\epsilon_2$  as  $r = p_4$  and for  $\epsilon_3$  and  $\epsilon_4$  as  $r = p_1$  leads to  $\epsilon_2 \cdot \epsilon_3$  being the only non-vanishing contraction. For the process there are now four diagrams to consider. Starting with the four-gluon vertex and the conventions laid out above this becomes

$$\begin{aligned}
 i\mathcal{M}_4 = & \begin{array}{c} \mu; a \\ \text{~~~~~} \\ \text{~~~~~} \\ \rho; c \end{array} \begin{array}{c} \nu; b \\ \text{~~~~~} \\ \text{~~~~~} \\ \sigma; d \end{array} = -ig^2 \times [f^{abc} f^{cde} (g^{\mu\rho} g^{\nu\sigma} - g^{\mu\sigma} g^{\nu\rho}) \\
 & + f^{ace} f^{bde} (g^{\mu\nu} g^{\rho\sigma} - g^{\mu\sigma} g^{\nu\rho}) \\
 & + f^{ade} f^{bce} (g^{\mu\nu} g^{\rho\sigma} - g^{\mu\rho} g^{\nu\sigma})] \\
 & \epsilon_{1,\mu}^-(4) \epsilon_{2,\rho}^-(4) \epsilon_{3,\nu}^+(1) \epsilon_{4,\sigma}^+(1) \\
 = & ig^2 \{ f^{abc} f^{cde} [(\epsilon_1^-(4) \cdot \epsilon_2^-(4)) (\epsilon_3^+(1) \cdot \epsilon_4^+(1)) - (\epsilon_1^-(4) \cdot \epsilon_4^+(1)) (\epsilon_3^+(1) \cdot \epsilon_2^-(4))] \\
 & + f^{ace} f^{bde} [(\epsilon_1^-(4) \cdot \epsilon_3^+(1)) (\epsilon_2^-(4) \cdot \epsilon_4^+(1)) - (\epsilon_1^-(4) \cdot \epsilon_4^+(1)) (\epsilon_3^+(1) \cdot \epsilon_2^-(4))] \\
 & + f^{ade} f^{bce} [(\epsilon_1^-(4) \cdot \epsilon_3^+(1)) (\epsilon_2^-(4) \cdot \epsilon_4^+(1)) - (\epsilon_1^-(4) \cdot \epsilon_2^-(4)) (\epsilon_3^+(1) \cdot \epsilon_4^+(1))] \} \\
 = & 0. \tag{A.51}
 \end{aligned}$$

So the four-gluon vertex does not contribute to this process. In the following the reference momentum will still be chosen as above, but will not be written down explicitly. Next is the s-channel diagram:

$$\begin{aligned}
 i\mathcal{M}_s = & \begin{array}{c} \mu; a \\ \text{~~~~~} \\ p_1 \\ \text{~~~~~} \\ \nu; b \end{array} \begin{array}{c} p_2 \\ \text{~~~~~} \\ \text{~~~~~} \\ p_4 \end{array} \begin{array}{c} p_3 \\ \text{~~~~~} \\ \text{~~~~~} \\ \chi; f \end{array} \begin{array}{c} \varphi; e \\ \text{~~~~~} \\ \text{~~~~~} \\ \text{~~~~~} \end{array} = ig^2 \epsilon_{1,\mu}^- \epsilon_{2,\nu}^- f^{abc} f^{def} [g^{\mu\nu} (p_1 - p_2)^\rho + g^{\nu\rho} (p_2 + q)^\mu \\
 & + g^{\rho\mu} (-q - p_1)^\nu] \frac{-g^{\rho\sigma} \delta_{cd}}{q^2} [g^{\sigma\varphi} (q - p_3)^\chi \\
 & + g^{\varphi\chi} (p_3 - p_4)^\sigma + g^{\chi\sigma} (p_4 - q)^\varphi] \epsilon_{3,\varphi}^* \epsilon_{4,\chi}^* \\
 = & -i \frac{g^2}{s} f^{abc} f^{efc} [(\epsilon_1^- \epsilon_2^-) (p_1 - p_2)^\rho + 2\epsilon_2^{-,\rho} (\epsilon_1^- p_2) - 2\epsilon_1^{-,\rho} (\epsilon_2^- p_1)] \\
 & \times [(\epsilon_3^+ \epsilon_4^+) (p_3 - p_4)^\rho + 2\epsilon_4^{+,\rho} (\epsilon_3^+ p_4) - 2\epsilon_3^{+,\rho} (\epsilon_4^+ p_3)] \tag{A.52}
 \end{aligned}$$

Now it is time to use the spinor products from above. The Mandelstam variables also have to be expressed in terms of these products:

$$s = \langle 21 \rangle [12] = \langle 34 \rangle [43] \quad (\text{A.53})$$

$$t = [14] \langle 41 \rangle = [23] \langle 32 \rangle \quad (\text{A.54})$$

$$u = \langle 31 \rangle [13] = \langle 42 \rangle [24]. \quad (\text{A.55})$$

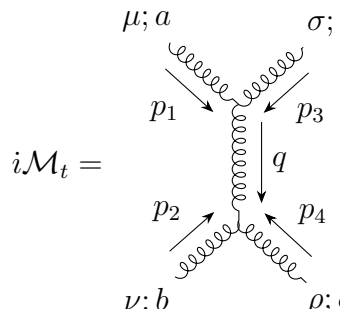
The s-matrix element then becomes

$$\begin{aligned} \mathcal{M}_s &= 4 \frac{g^2}{s} f^{abc} f^{efc} (\epsilon_2^- \epsilon_3^+) (\epsilon_1^- p_2) (\epsilon_4^+ p_3) = 2g^2 f^{abc} f^{efc} \frac{1}{\langle 21 \rangle [12] [24] \langle 13 \rangle} \frac{\langle 21 \rangle [34] \langle 12 \rangle [24] [43] \langle 31 \rangle}{[14] \langle 14 \rangle} \\ &= 2g^2 f^{abc} f^{efc} \frac{\langle 12 \rangle [34]^2}{[12] [14] \langle 41 \rangle}. \end{aligned} \quad (\text{A.56})$$

This can be simplified by writing the 1 more complicated e.g.  $s/s$ ; also using equation (A.43) one can write  $\langle 12 \rangle [23] = -\langle 14 \rangle [43]$ . With this:

$$\begin{aligned} \mathcal{M}_s &= 2g^2 f^{abc} f^{efc} \frac{\langle 12 \rangle [34]^2}{[12] [14] \langle 41 \rangle} \left( \frac{[14] \langle 41 \rangle}{[23] \langle 32 \rangle} \right) \left( \frac{[12] \langle 21 \rangle}{\langle 34 \rangle [43]} \right) \left( \frac{\langle 12 \rangle [23]}{\langle 14 \rangle [34]} \right) \\ &= -2g^2 f^{abc} f^{efc} \frac{\langle 12 \rangle^3}{\langle 23 \rangle \langle 34 \rangle \langle 41 \rangle}. \end{aligned} \quad (\text{A.57})$$

In many in-between steps the order in bispinors was swapped, which introduces additional minus signs. Turning to the t-channel diagram now:



$$\begin{aligned} i\mathcal{M}_t &= -i \frac{g^2}{t} f^{ade} f^{cbe} \epsilon_{1,\mu}^- \epsilon_{2,\nu}^- \epsilon_{3,\rho}^+ \epsilon_{4,\sigma}^+ [g^{\mu\theta} (p_1 + q)^\sigma + g^{\theta\sigma} (-q - p_4)^\mu \\ &\quad + g^{\sigma\mu} (p_4 - p_1)^\theta] [g^{\nu\rho} (p_2 - p_3)^\theta + g^{\sigma\theta} (p_3 - q)^\nu + g^{\theta\nu} (q - p_2)^\rho] \\ &= -i \frac{g^2}{t} f^{ade} f^{cbe} \left[ (\epsilon_1^- \epsilon_4^+) (p_4 - p_1)^\theta + 2\epsilon_1^\theta (\epsilon_4^+ p_1)^\theta - 2\epsilon_4^\theta (\epsilon_1^- p_4) \right] \times \\ &\quad \left[ (\epsilon_2^- \epsilon_3^+) (p_2 - p_3)^\theta + 2\epsilon_3^\theta (\epsilon_2^- p_3)^\theta - 2\epsilon_2^\theta (\epsilon_3^+ p_2) \right]. \end{aligned} \quad (\text{A.58})$$

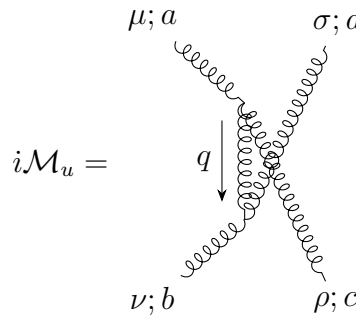
Using the bispinors

$$p_1 \epsilon_4^+ = \frac{1}{2} \frac{[41]\langle 44 \rangle}{\langle 41 \rangle} = 0, \quad \epsilon_1^- p_4 = \frac{1}{2} \frac{\langle 14 \rangle [44]}{\langle 14 \rangle} = 0, \quad \epsilon_1^- \epsilon_4^+ = \frac{\langle 11 \rangle [44]}{[14]\langle 14 \rangle} = 0 \quad (\text{A.59})$$

it follows that

$$\mathcal{M}_t = 0. \quad (\text{A.60})$$

The last remaining diagram is the u-channel



$$\begin{aligned}
 i\mathcal{M}_u &= -ig^2 f^{aec} f^{bdf} \epsilon_{1,\mu} \epsilon_{2,\nu} \epsilon_{3,\rho} \epsilon_{4,\sigma} \left[ g^{\mu\theta} (p_1 + q)^\rho + g^{\theta\rho} (-q - p_3)^\mu \right. \\
 &\quad \left. + g^{\rho\mu} (p_3 - p_1)^\theta \right] \frac{g^{\theta\varphi} \delta_{ef}}{u} \left[ g^{\nu\sigma} (p_2 - p_4)^\varphi + g^{\sigma\varphi} (p_4 - q)^\nu \right. \\
 &\quad \left. + g^{\varphi\nu} (q - p_2)^\rho \right] \\
 &= -i \frac{g^2}{u} f^{ace} f^{bde} \left[ (\epsilon_1^- \epsilon_3^+) (p_1 - p_3)^\theta + 2\epsilon_3^\theta (\epsilon_1^- p_3) - 2\epsilon_1^\theta (\epsilon_3^+ p_1) \right] \times \\
 &\quad \left[ (\epsilon_2^- \epsilon_4^+) (p_2 - p_4)^\theta + 2\epsilon_4^\theta (\epsilon_2^- p_4) - 2\epsilon_2^\theta (\epsilon_4^+ p_2) \right] \quad (\text{A.61})
 \end{aligned}$$

Now using the relation between polarisations and expressing everything as bispinors

$$\begin{aligned}
 \mathcal{M}_u &= \frac{4g^2}{u} (\epsilon_3^+ \epsilon_2^-) (\epsilon_1^- p_3) (\epsilon_4^+ p_2) = 2g^2 f^{ace} f^{bde} \frac{1}{\langle 31 \rangle [13] [24] \langle 13 \rangle} \frac{\langle 21 \rangle [34] \langle 13 \rangle [34] [42] \langle 21 \rangle}{[14] \langle 14 \rangle} \\
 &= 2g^2 f^{ace} f^{bde} \frac{\langle 21 \rangle^2 [34]^2}{\langle 13 \rangle [13] [14] \langle 14 \rangle} \left( \frac{[14] \langle 41 \rangle}{[23] \langle 32 \rangle} \right) \left( -\frac{\langle 21 \rangle [13]}{\langle 42 \rangle [34]} \right) \left( -\frac{\langle 12 \rangle [23]}{\langle 41 \rangle [34]} \right) \\
 &= -2g^2 f^{ace} f^{bde} \frac{\langle 21 \rangle^4}{\langle 14 \rangle \langle 42 \rangle \langle 23 \rangle \langle 31 \rangle}. \quad (\text{A.62})
 \end{aligned}$$

Summing the two non-vanishing contributions gives the matrix element:

$$\mathcal{M}(1^-, 2^-, 3^+, 4^+) = -2g^2 \left[ f^{abc} f^{efc} \frac{\langle 12 \rangle^3}{\langle 23 \rangle \langle 34 \rangle \langle 41 \rangle} + f^{ace} f^{bde} \frac{\langle 21 \rangle^4}{\langle 14 \rangle \langle 42 \rangle \langle 23 \rangle \langle 31 \rangle} \right]. \quad (\text{A.63})$$



For the calculation of the squared matrix element the bispinor part will come first and afterwards comes the colour part. Bispinors under complex conjugation behave as  $(\langle 14 \rangle)^\dagger = [41]$  so that

$$\left| \frac{\langle 12 \rangle^3}{\langle 23 \rangle \langle 34 \rangle \langle 41 \rangle} \right|^2 = \frac{\langle 12 \rangle^3 [21]^3}{\langle 23 \rangle [32] \langle 34 \rangle [43] \langle 41 \rangle [41]} = \frac{s^2}{t^2}, \quad (\text{A.64})$$

$$\left| \frac{\langle 21 \rangle^4}{\langle 14 \rangle \langle 42 \rangle \langle 23 \rangle \langle 31 \rangle} \right|^2 = \frac{\langle 21 \rangle^4 [12]^4}{\langle 14 \rangle [41] \langle 42 \rangle [24] \langle 23 \rangle [32] \langle 31 \rangle [13]} = \frac{s^4}{t^2 u^2}, \quad (\text{A.65})$$

$$\frac{[12]^4 \langle 21 \rangle^4}{[12][23][34][41] \langle 14 \rangle \langle 42 \rangle \langle 23 \rangle \langle 31 \rangle} = \frac{s^4}{st^2 u}, \quad (\text{A.66})$$

for the squared matrix elements, where the Mandelstam variables from above were used. Turning to the colour factor now, there are two different calculations to be done, namely  $(f^{abe} f^{cde})^2$  and  $(f^{abe} f^{cde})(f^{acg} f^{bdg})$ . For this the structure constants can be expressed in terms of generators:

$$f^{abc} = -2i \operatorname{tr}([T^a, T^b] T^c). \quad (\text{A.67})$$

One can give some relations that are useful for calculating several traces involving generators:

$$\operatorname{tr}(T^a A) \operatorname{tr}(T^a B) = \frac{1}{2} \left( \operatorname{tr}(AB) - \frac{1}{N} \operatorname{tr}(A) \operatorname{tr}(B) \right), \quad (\text{A.68})$$

$$\operatorname{tr}(AT^a BT^a) = \frac{1}{2} \left( \operatorname{tr}(A) \operatorname{tr}(B) - \frac{1}{N} \operatorname{tr}(AB) \right). \quad (\text{A.69})$$

Starting with  $(f^{abe} f^{cde})^2$  and the trace relations above:

$$(f^{abe} f^{cde})^2 = (-2 \operatorname{tr}([T^a, T^b][T^c, T^d]))^2 \quad (\text{A.70})$$

$$= (-2 \operatorname{tr}(T^a T^b T^c T^d - T^a T^b T^d T^c - T^b T^a T^c T^d + T^b T^a T^d T^c))^2. \quad (\text{A.71})$$

Using trace properties  $\text{tr}(A + B) = \text{tr}(A) + \text{tr}(B)$  and introducing  $\mathbb{1}$  as shorthand for the colour factor  $T^a$  coming from gluon 1 etc. this then becomes

$$\begin{aligned} (f^{abe} f^{cde})^2 = & 4(\text{tr}(1234) \text{tr}(1234) - 2 \text{tr}(1234) \text{tr}(1243) - 2 \text{tr}(1234) \text{tr}(2134) \\ & + 2 \text{tr}(1234) \text{tr}(2143) + \text{tr}(1243) \text{tr}(1243) + 2 \text{tr}(1243) \text{tr}(2134) \\ & - 2 \text{tr}(1243) \text{tr}(2143) + \text{tr}(2134) \text{tr}(2134) - 2 \text{tr}(2134) \text{tr}(2143) \\ & + \text{tr}(2143) \text{tr}(2143)) \end{aligned} \quad (\text{A.72})$$

The calculation will now be demonstrated for some examples: the full calculation is in principle not difficult, but very lengthy and prone to error, so is better left to some computer algebra system like Form. Starting with  $\text{tr}(1234) \text{tr}(1234)$  it is easiest to start with the trace over two generators and going up in complexity, while noting that  $\text{tr}(T^a) = \text{tr}(\mathbb{1}) = 0$  and using the relation from above. Also using the unit matrix  $\mathbb{1}$  and  $\text{tr}(\mathbb{1}) = N$ :

$$\bullet \text{tr}(\mathbb{1}\mathbb{1}) = \text{tr}(\mathbb{1}\mathbb{1}\mathbb{1}\mathbb{1}) = \frac{1}{2} \left( \text{Tr}(\mathbb{1}) \text{tr}(\mathbb{1}) - \frac{1}{N} \text{tr}(\mathbb{1}) \right) = \frac{N^2 - 1}{2}, \quad (\text{A.73})$$

$$\bullet \text{tr}(12) \text{tr}(12) = \frac{1}{2} \left( \text{tr}(22) - \frac{1}{N} \text{tr}(2) \text{tr}(2) \right) = \frac{N^2 - 1}{4}, \quad (\text{A.74})$$

$$\bullet \text{tr}(1212) = \frac{1}{2} \left( \text{tr}(1) \text{tr}(1) - \frac{1}{N} \text{tr}(11) \right) = \frac{1 - N^2}{4N}, \quad (\text{A.75})$$

$$\begin{aligned} \bullet \text{tr}(123) \text{tr}(123) &= \frac{1}{2} \left( \text{tr}(2323) - \frac{1}{N} \text{tr}(23) \text{tr}(23) \right) = \frac{1}{2} \left( \frac{1 - N^2}{4N} - \frac{N^2 - 1}{4N} \right) \quad (\text{A.76}) \\ &= \frac{1 - N^2}{4N}, \end{aligned}$$

$$\bullet \text{tr}(123123) = \frac{1}{2} \left( \text{tr}(12) \text{tr}(12) - \frac{1}{N} \text{tr}(1212) \right) = \frac{N^4 - 1}{8N^2}, \quad (\text{A.77})$$

$$\bullet \text{tr}(1234) \text{tr}(1234) = \frac{1}{2} \left( \text{tr}(234234) - \frac{1}{N} \text{tr}(234) \text{tr}(234) \right) = \frac{N^4 + 2N^2 - 3}{16N^2}. \quad (\text{A.78})$$

As another example look at  $\text{tr}(1234) \text{tr}(2143)$ :

$$\begin{aligned} \text{tr}(1234) \text{tr}(2143) &= \text{tr}(1234) \text{tr}(1432) = \frac{1}{2} \left( \text{tr}(234432) - \frac{1}{N} \text{tr}(234) \text{tr}(432) \right) \\ &= \frac{1}{2} \left[ \frac{1}{2} \left( \text{tr}(\mathbb{1}) \text{tr}(3443) - \frac{1}{N} \text{tr}(3443) \right) - \frac{1}{2N} \left( \text{tr}(3443) - \frac{1}{N} \text{tr}(34) \text{tr}(43) \right) \right] \\ &= \frac{N^6 - 4N^4 + 6N^2 - 3}{16N^2}. \end{aligned} \quad (\text{A.79})$$

Working everything out leads to

$$(f^{abe} f^{cde})^2 = N^2(N^2 - 1) \quad (\text{A.80})$$

$$(f^{abe} f^{cde})(f^{acg} f^{bdg}) = \frac{1}{2}N^2(N^2 - 1). \quad (\text{A.81})$$

Putting all the parts together gives the squared matrix element

$$\sum_{\text{colour}} |\mathcal{M}(1^-, 2^-, 3^+, 4^+)|^2 = 4g^4 N^2(N^2 - 1) \left( \frac{s^4}{t^2 u^2} - \frac{s^2}{tu} \right). \quad (\text{A.82})$$

There are in principle five more MHV amplitudes that contribute, which are related to the one above by crossing symmetry. The other amplitudes correspond to the possible permutations of the s, t and u. Averaging the initial state gives a factor  $\frac{1}{4}$  for the spin and there are  $N^2 - 1$  colours. Taking  $N = 3$  now for QCD gives

$$\frac{1}{256} \sum_{\substack{\text{pols.} \\ \text{colours}}} |\mathcal{M}|^2 = \frac{9}{2}g^4 \left( 3 - \frac{su}{t^2} - \frac{ut}{s^2} - \frac{st}{u^2} \right). \quad (\text{A.83})$$

The relation  $s + t + u = 0$  is used a lot here. These calculations are best left to be done by CAS, since they are, again, very lengthy.

## List of Figures

2.1	Running coupling $\alpha_s$ . . . . .	13
3.1	nCTEQ15 nPDFs for lead . . . . .	21
3.2	Glauber model beam pipe view . . . . .	32
3.3	Centrality . . . . .	34
4.1	Comparison of different jet algorithms . . . . .	38
5.1	Sketch of producing a QGP through increasing the nucleon density . . . . .	41
6.1	Four-Momentum-Subtraction . . . . .	53
8.1	ALICE differential jet cross section in pp . . . . .	64
8.2	ALICE differential jet yield in PbPb . . . . .	65
8.3	ALICE nuclear modification factor $R_{AA}$ . . . . .	66
8.4	ALICE differential jet yield in PbPb for different $T_C$ . . . . .	67
8.5	ALICE differential jet yield in PbPb for different $T_I$ . . . . .	68
8.6	CMS differential jet cross section in pp . . . . .	69
8.7	CMS differential jet yield in PbPb . . . . .	70
8.8	CMS nuclear modification factor $R_{AA}$ . . . . .	71
8.9	CMS differential jet yield in PbPb for different $T_C$ . . . . .	72
8.10	CMS differential jet yield in PbPb for different $T_I$ . . . . .	72
8.11	ATLAS differential jet cross section in pp . . . . .	73
8.12	ATLAS differential jet yield in PbPb . . . . .	74
8.13	ATLAS nuclear modification factor $R_{AA}$ . . . . .	75
8.14	ATLAS differential jet yield in PbPb for different $T_C$ . . . . .	76
8.15	ATLAS differential jet yield in PbPb for different $T_I$ . . . . .	76

## Bibliography

- [1] **M. Aaboud et al.** *Measurement of jet  $p_T$  correlations in Pb+Pb and pp collisions at  $\sqrt{s_{NN}} = 2.76$  TeV with the ATLAS detector.* Phys. Lett., B774:379–402 (2017). 57
- [2] **M. Aaboud et al.** *Measurement of jet fragmentation in Pb+Pb and pp collisions at  $\sqrt{s_{NN}} = 5.02$  TeV with the ATLAS detector.* Phys. Rev., C98(2):024908 (2018). 56
- [3] **M. Aaboud et al.** *Measurement of photon–jet transverse momentum correlations in 5.02 TeV Pb + Pb and pp collisions with ATLAS.* Phys. Lett., B789:167–190 (2019). 56
- [4] **M. Aaboud et al.** *Measurement of the nuclear modification factor for inclusive jets in Pb+Pb collisions at  $\sqrt{s_{NN}} = 5.02$  TeV with the ATLAS detector.* Phys. Lett., B790:108–128 (2019). 56, 59, 73, 74, 75
- [5] **B. Abelev et al.** *Measurement of the inclusive differential jet cross section in pp collisions at  $\sqrt{s} = 2.76$  TeV.* Phys. Lett., B722:262–272 (2013). 64
- [6] **S. Acharya et al.** *First measurement of jet mass in Pb–Pb and p–Pb collisions at the LHC.* Phys. Lett., B776:249–264 (2018). 57
- [7] **S. Acharya et al.** *Medium modification of the shape of small-radius jets in central Pb–Pb collisions at  $\sqrt{s_{NN}} = 2.76$  TeV.* JHEP, 10:139 (2018). 56
- [8] **J. Adam et al.** *Measurement of jet suppression in central Pb–Pb collisions at  $\sqrt{s_{NN}} = 2.76$  TeV.* Phys. Lett., B746:1–14 (2015). 53, 58, 59, 63, 64, 65, 66
- [9] **J. Adam et al.** *Direct photon production in Pb–Pb collisions at  $\sqrt{s_{NN}} = 2.76$  TeV.* Phys. Lett., B754:235–248 (2016). 66

- [10] **J. Adam et al.** *Anomalous evolution of the near-side jet peak shape in Pb-Pb collisions at  $\sqrt{s_{NN}} = 2.76$  TeV.* Phys. Rev. Lett., 119(10):102301 (2017). 57
- [11] **J. Adam et al.** *Evolution of the longitudinal and azimuthal structure of the near-side jet peak in Pb-Pb collisions at  $\sqrt{s_{NN}} = 2.76$  TeV.* Phys. Rev., C96(3):034904 (2017). 57
- [12] **A. Bazavov et al.** *Chiral crossover in QCD at zero and non-zero chemical potentials* (2018). 66
- [13] **J. Beringer et al.** *Review of Particle Physics (RPP).* Phys. Rev., D86:010001 (2012). 13
- [14] **J. D. Bjorken.** *Highly Relativistic Nucleus-Nucleus Collisions: The Central Rapidity Region.* Phys. Rev., D27:140–151 (1983). 42
- [15] **A. Buckley, J. Butterworth, L. Lonnblad, D. Grellscheid, H. Hoeth, J. Monk, H. Schulz and F. Siegert.** *Rivet user manual.* Comput. Phys. Commun., 184:2803–2819 (2013). 63
- [16] **A. Buckley, J. Ferrando, S. Lloyd, K. Nordström, B. Page, M. Rüfenacht, M. Schönherr and G. Watt.** *LHAPDF6: parton density access in the LHC precision era.* Eur. Phys. J., C75:132 (2015). 61
- [17] **M. Cacciari, G. P. Salam and G. Soyez.** *FastJet User Manual.* Eur. Phys. J., C72:1896 (2012). 39
- [18] **S. Chatrchyan et al.** *Observation and studies of jet quenching in PbPb collisions at nucleon-nucleon center-of-mass energy = 2.76 TeV.* Phys. Rev., C84:024906 (2011). 58
- [19] **S. Chatrchyan et al.** *Jet momentum dependence of jet quenching in PbPb collisions at  $\sqrt{s_{NN}} = 2.76$  TeV.* Phys. Lett., B712:176–197 (2012). 58
- [20] **S. Chatrchyan et al.** *Measurement of jet fragmentation into charged particles in pp and PbPb collisions at  $\sqrt{s_{NN}} = 2.76$  TeV.* JHEP, 10:087 (2012). 58
- [21] **K. G. Chetyrkin, J. H. Kuhn and M. Steinhauser.** *RunDec: A Mathematica package for running and decoupling of the strong coupling and quark masses.* Comput. Phys. Commun., 133:43–65 (2000). 62

- [22] **M. Droettboom, T. A. Caswell, J. Hunter, E. Firing, J. H. Nielsen, N. Varoquaux, A. Lee, E. S. de Andrade, B. Root, D. Stansby and et al.** *matplotlib/matplotlib v2.1.2* (2018). 63
- [23] **R. K. Ellis, W. J. Stirling and B. R. Webber.** *QCD and collider physics.* Camb. Monogr. Part. Phys. Nucl. Phys. Cosmol., 8:1–435 (1996). 80
- [24] **K. J. Eskola, P. Paakkinen, H. Paukkunen and C. A. Salgado.** *EPPS16: Nuclear parton distributions with LHC data.* Eur. Phys. J., C77(3):163 (2017). 62
- [25] **K. J. Eskola, H. Paukkunen and C. A. Salgado.** *EPS09: A New Generation of NLO and LO Nuclear Parton Distribution Functions.* JHEP, 04:065 (2009). 61
- [26] **S. Ferreres-Solé and T. Sjöstrand.** *The space–time structure of hadronization in the Lund model.* Eur. Phys. J., C78(11):983 (2018). 29
- [27] **V. Khachatryan et al.** *Correlations between jets and charged particles in PbPb and pp collisions at  $\sqrt{s_{NN}} = 2.76$  TeV.* JHEP, 02:156 (2016). 58
- [28] **V. Khachatryan et al.** *Decomposing transverse momentum balance contributions for quenched jets in PbPb collisions at  $\sqrt{s_{NN}} = 2.76$  TeV.* JHEP, 11:055 (2016). 57
- [29] **V. Khachatryan et al.** *Measurement of transverse momentum relative to dijet systems in PbPb and pp collisions at  $\sqrt{s_{NN}} = 2.76$  TeV.* JHEP, 01:006 (2016). 58
- [30] **V. Khachatryan et al.** *Charged-particle nuclear modification factors in PbPb and pPb collisions at  $\sqrt{s_{NN}} = 5.02$  TeV.* JHEP, 04:039 (2017). 57
- [31] **V. Khachatryan et al.** *Measurement of inclusive jet cross sections in pp and PbPb collisions at  $\sqrt{s_{NN}} = 2.76$  TeV.* Phys. Rev., C96(1):015202 (2017). 57, 59, 68, 69, 70, 71
- [32] **K. Kovarik et al.** *nCTEQ15 - Global analysis of nuclear parton distributions with uncertainties in the CTEQ framework.* Phys. Rev., D93(8):085037 (2016). 21, 22, 62
- [33] **R. Kunnawalkam Elayavalli and K. C. Zapp.** *Medium response in JEWEL and its impact on jet shape observables in heavy ion collisions.* JHEP, 07:141 (2017). 52

- [34] **E. Maguire, L. Heinrich and G. Watt.** *HEPData: a repository for high energy physics data.* J. Phys. Conf. Ser., 898(10):102006 (2017). 63
- [35] **M. L. Miller, K. Reygers, S. J. Sanders and P. Steinberg.** *Glauber modeling in high energy nuclear collisions.* Ann. Rev. Nucl. Part. Sci., 57:205–243 (2007). 31, 32, 34
- [36] **P. Nason.** *A New method for combining NLO QCD with shower Monte Carlo algorithms.* JHEP, 11:040 (2004). 28
- [37] **M. E. Peskin and D. V. Schroeder.** *An Introduction to quantum field theory.* Addison-Wesley, Reading, USA (1995). 3, 16, 25
- [38] **G. P. Salam.** *Towards Jetography.* Eur. Phys. J., C67:637–686 (2010). 36, 38
- [39] **H. Satz.** *Extreme states of matter in strong interaction physics. An introduction.* Lect. Notes Phys., 841:1–239 (2012). 41, 44
- [40] **M. D. Schwartz.** *Quantum Field Theory and the Standard Model.* Cambridge University Press (2014). 3, 16, 80, 87
- [41] **A. M. Sirunyan et al.** *Study of Jet Quenching with Z + jet Correlations in Pb-Pb and pp Collisions at  $\sqrt{s_{NN}} = 5.02$  TeV.* Phys. Rev. Lett., 119(8):082301 (2017). 57
- [42] **A. M. Sirunyan et al.** *Comparing transverse momentum balance of b jet pairs in pp and PbPb collisions at  $\sqrt{s_{NN}} = 5.02$  TeV.* JHEP, 03:181 (2018). 56
- [43] **A. M. Sirunyan et al.** *Jet properties in PbPb and pp collisions at  $\sqrt{s_{NN}} = 5.02$  TeV.* JHEP, 05:006 (2018). 56
- [44] **A. M. Sirunyan et al.** *Measurement of the groomed jet mass in PbPb and pp collisions at  $\sqrt{s_{NN}} = 5.02$  TeV.* JHEP, 10:161 (2018). 56
- [45] **A. M. Sirunyan et al.** *Study of jet quenching with isolated-photon+jet correlations in PbPb and pp collisions at  $\sqrt{s_{NN}} = 5.02$  TeV.* Phys. Lett., B785:14–39 (2018). 57
- [46] **T. Sjostrand, S. Mrenna and P. Z. Skands.** *PYTHIA 6.4 Physics and Manual.* JHEP, 05:026 (2006). 28, 29, 60, 62



- [47] **T. Sjöstrand and P. Z. Skands.** *Transverse-momentum-ordered showers and interleaved multiple interactions.* Eur. Phys. J., C39:129–154 (2005). 27
- [48] **T. Sjöstrand, S. Ask, J. R. Christiansen, R. Corke, N. Desai, P. Ilten, S. Mrenna, S. Prestel, C. O. Rasmussen and P. Z. Skands.** *An Introduction to PYTHIA 8.2.* Comput. Phys. Commun., 191:159–177 (2015). 61
- [49] **M. R. Whalley, D. Bourilkov and R. C. Group.** *The Les Houches accord PDFs (LHAPDF) and LHAGLUE.* In *HERA and the LHC: A Workshop on the implications of HERA for LHC physics. Proceedings, Part B*, pp. 575–581 (2005). 61
- [50] **K. Zapp, G. Ingelman, J. Rathsman and J. Stachel.** *Jet quenching from soft QCD scattering in the quark-gluon plasma.* Phys. Lett., B637:179–184 (2006). 48
- [51] **K. Zapp, G. Ingelman, J. Rathsman, J. Stachel and U. A. Wiedemann.** *A Monte Carlo Model for 'Jet Quenching'.* Eur. Phys. J., C60:617–632 (2009). 48
- [52] **K. Zapp, J. Stachel and U. A. Wiedemann.** *A Local Monte Carlo implementation of the non-abelian Landau-Pomeranchuk-Migdal effect.* Phys. Rev. Lett., 103:152302 (2009). 48
- [53] **K. C. Zapp.** *JEWEL 2.0.0: directions for use.* Eur. Phys. J., C74(2):2762 (2014). 48
- [54] **K. C. Zapp, F. Krauss and U. A. Wiedemann.** *A perturbative framework for jet quenching.* JHEP, 03:080 (2013). 27, 48
- [55] **K. C. Zapp, J. Stachel and U. A. Wiedemann.** *A local Monte Carlo framework for coherent QCD parton energy loss.* JHEP, 07:118 (2011). 48